Advanced Materials Technologies

ADVANCED MATERIALS TECHNOLOGIES
www.advmattechnol.com

REVIEW OPEN ACCESS

Transducers Across Scales and Frequencies: A System-Level Framework for Multiphysics Integration and Co-Design

Aolei Xu[1,2,3] | Mengyao Xiao[1,2] | Zhouli Sui[1,2,3] | Yinpeng Wang[1,2] | Daoye Zheng[1,2,4] | Yuxin Liu[1,2,4] | Luwei Wang[1,2] | Huajun Liu[5] | Chengkuo Lee[1,2,3,4,6]

[1]Department of Electrical and Computer Engineering, National University of Singapore, Singapore, Singapore | [2]Centre for Intelligent Sensors and MEMS (CISM), National University of Singapore, Singapore, Singapore | [3]National University of Singapore Suzhou Research Institute (NUSRI), Suzhou Industrial Park, Suzhou, China | [4]National Centre for Advanced Integrated Photonics (NCAIP), Singapore, Singapore | [5]Institute of Materials Research and Engineering (IMRE), Agency for Science, Technology and Research (A*STAR), Singapore, Singapore | [6]NUS Graduate School–Integrative Sciences and Engineering Programme (ISEP), National University of Singapore, Singapore, Singapore

Correspondence: Huajun Liu (liu_huajun@imre.a-star.edu.sg) | Chengkuo Lee (elelc@nus.edu.sg)

Received: 30 September 2025 | **Revised:** 20 January 2026 | **Accepted:** 3 February 2026

Keywords: heterogeneous integration | in-sensor computing | metasurfaces | photonics | quantum photonics | scaling | transducers

ABSTRACT

Transducers underpin modern sensing, actuation, and modulation by converting physical signals into electrical or optical representations. Despite rapid advances across materials, fabrication, and device architectures, individual transduction mechanisms remain constrained by intrinsic trade-offs among bandwidth, sensitivity, speed, energy consumption, and integrability. This review examines transducer technologies across mechanical, acoustic, electromagnetic, and optical domains, and shows that performance evolution is not only increasingly governed by the discovery of new mechanisms, but also by the system-level coordination of established ones. By organizing representative platforms according to physical scale, operating frequency, and accessible degrees of freedom, we reveal how distinct mechanisms occupy complementary performance envelopes across Hertz-to-THz regimes. We highlight how heterogeneous integration and multiphysics co-design enable these envelopes to be traversed through coordinated architectures that combine flexible interfaces, electromechanical systems, metasurfaces, and photonic circuits. This perspective reframes transducers from isolated interfaces into programmable system nodes that jointly support sensing, modulation, and information processing. The resulting framework provides a foundation for designing reconfigurable and scalable transducer systems for sustainable applications, precision imaging, adaptive communication, edge intelligence, and emerging quantum technologies.

1 | Introduction

Transducers define the boundary at which physical phenomena become accessible to engineered systems. By converting mechanical, thermal, electromagnetic, chemical, or quantum signals into electrical or optical representations, they enable sensing, actuation, modulation, and control across a wide range of technologies [1–6]. As such, transducers do not merely connect the physical and digital domains; they determine how information is encoded, transmitted, and processed across scales and platforms.

Over the past decades, advances in micro- and nanofabrication [7–9], photonic engineering [10–14], and heterogeneous integration [15–20] have substantially expanded the space of realizable transduction mechanisms. Transducer platforms now span operating frequencies from sub-hertz mechanical deformation to GHz

and THz electromagnetic carriers, supporting applications in wearable health monitoring, environmental sensing, communication systems, and emerging edge devices [21]. They serve as the interface for sensing [22–24], modulation [25], actuation [26, 27], and even primitive forms of computing in various systems [28]. They allow wearable monitors to perceive physiological cues [29], Internet of Things (IoT) nodes to gather environmental data [21, 30], communication systems to modulate and transmit information [31, 32], and emerging edge devices to perform local signal processing [33, 34] and enable energy-autonomous operation [35–37]. Despite this diversity, a fundamental constraint persists: each established transduction mechanism is governed by intrinsic trade-offs among sensitivity, bandwidth, response time, noise, energy consumption, linearity, and integrability. These trade-offs arise from carrier dynamics [38], inertia [39], dissipation [40], thermodynamic [41], and field confinement, and they confine every mechanism to a bounded performance envelope.

As system-level requirements evolve, this constraint becomes increasingly consequential. Contemporary platforms demand combinations of attributes that no single mechanism can deliver in isolation, including high sensitivity together with wide bandwidth, fast response with low power consumption, and compact footprint with long-term stability [21, 28, 42, 43]. Under such multi-objective constraints, incremental optimization or straightforward miniaturization of individual transducers proves insufficient [44, 45]. Performance gains can no longer be achieved solely within a single physical domain.

A key insight emerging from recent progress is that transducer evolution does not follow a linear trajectory of replacement or scaling, but instead reflects a reorganization of physical degrees of freedom across frequency and scale. Mechanical deformation, acoustic waves, electromagnetic fields, thermal gradients, and quantum-coherent states each provide distinct carriers of information, whose accessibility is strongly correlated with characteristic device dimensions and operating frequencies. Recent progress in micro- and nanofabrication, heterogeneous integration, and photonic engineering is already redefining what transducers can do with different physical degrees. These advances have unlocked new mechanisms and materials [46–51] that operate efficiently at scales from millimeters down to nanometers [52–54]. Mapping transducers across scale, frequency, and function serves not as a final design prescription, but as an analytical lens that reveals where and why single mechanisms become insufficient for complex system demands. Figure 1 frames transduction mechanisms as interoperable system components, organized across frequency, scale, and physical degrees of freedom, and provides a conceptual anchor for the structure of this review.

Within this landscape, heterogeneous integration and multiphysics co-design emerge as structural necessities rather than optional enhancements. Recent advances allow nanoscale photonic and plasmonic elements to be combined with microelectromechanical systems, flexible substrates, and electronic circuits within unified platforms [15–20, 55–57]. Flexible and compliant transducers operating at low frequencies enable robustness, conformability, and energy-autonomous operation in physiological and environmental interfaces [27, 35–37]. Microscale electromechanical devices operating in the kHz to MHz regime provide controllable coupling, array-level programmability, and compatibility with on-chip signal conditioning and inference [26]. At higher carrier frequencies, photonic and optoelectronic structures operating at GHz and THz regimes bypass mechanical inertia, enabling ultrafast modulation [58–60], high spectral resolution [61, 62], and field-mediated information encoding [28, 63]. When these complementary capabilities are deliberately coordinated, transducers evolve from isolated interfaces into programmable system nodes that organize information flow across physical domains.

This shift fundamentally redefines the role of the transducer. Rather than serving solely as a bridge between a stimulus and a readout circuit, the transducer becomes an active participant in system-level functionality. Its value lies not only in converting signals but in enabling coordinated sensing, actuation, modulation, and computation through reconfigurable interactions among verified physical mechanisms. The unit of innovation thus moves beyond materials or individual devices toward the designable relationships among multiple degrees of freedom enabled by heterogeneous integration.

In this review, we examine transducer technologies from this system-oriented perspective. By surveying representative platforms across mechanical, acoustic, electromagnetic, and optical domains, and organizing them according to characteristic scales, operating frequencies, and functional roles, we show how heterogeneous integration transforms established mechanisms into composable and evolvable system capabilities. This framework provides a coherent foundation for understanding current transducer technologies and for guiding the development of next-generation systems that demand simultaneous performance across bandwidth, sensitivity, speed, energy efficiency, and scalability [28].

2 | Flexible Transducers Across Audio–RF Scales

Flexible transducers and related wearable or implantable devices operate over mechanical excitation frequencies spanning subhertz human motion, audio-band vibrotactile stimulation at 10^2 Hz, and MHz-range ultrasonic waves, with characteristic device dimensions ranging from centimeter-scale textile platforms to millimeter-scale discrete units and micrometer-thick active layers [12, 34, 35, 57, 64–73]. These quantifiable transducer scale and frequency regimes of target signals help to determine the dominant transduction mechanisms, hence to affect achievable bandwidth, sensitivity, response time, and integration density, thereby defining functional roles in health monitoring, human–machine interaction, and energy harvesting. The representative works below illustrate how device size, operating frequency, and coupling physics are co-optimized to balance spatial coverage, signal fidelity, actuation strength, and system-level integration, rather than relying on qualitative scale distinctions.

One representative example is a haptic-feedback smart glove that integrates triboelectric finger-bending and palm-sliding sensors with piezoelectric PZT stimulators for immersive VR/AR human–machine interaction, as shown in Figure 2a [74]. The finger sensors employ Eco-flex hemispheres with a defined diameter

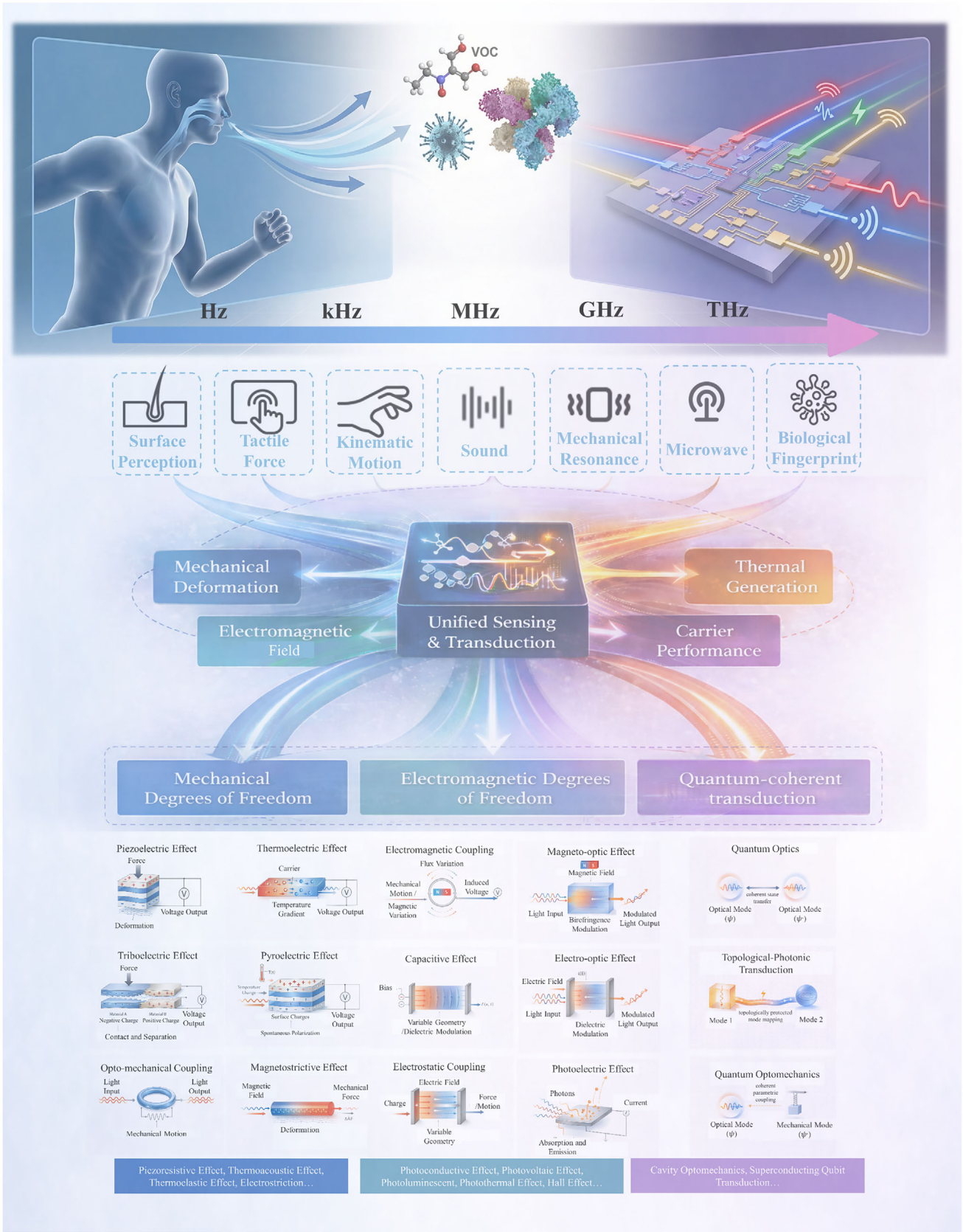

FIGURE 1 | System-level coordination of transduction mechanisms across frequency, scale, and physical degrees of freedom.

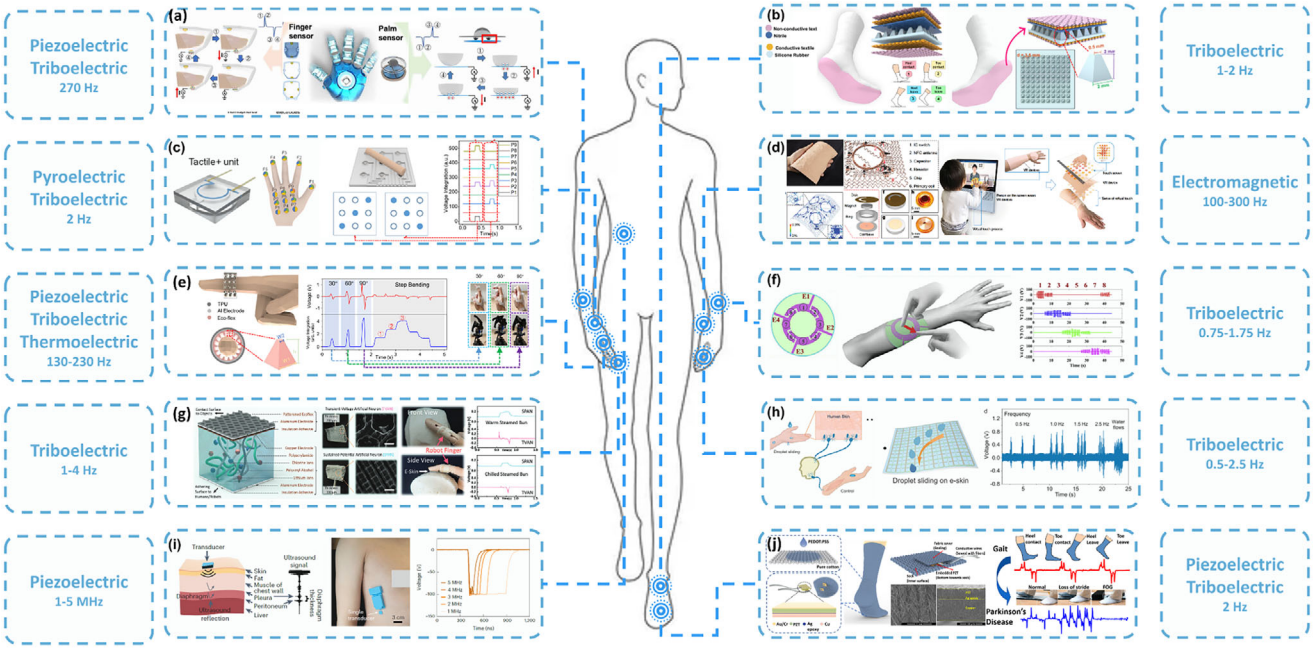

FIGURE 2 | Flexible transducer across Audio and RF Domains. (a) Haptic-feedback smart glove combining triboelectric sensors and piezoelectric actuators for real-time VR/AR interaction. Reproduced with permission [74]. Copyright 2020, The Authors. (b) Triboelectric smart socks for gait analysis and VR interaction. Reproduced with permission [75]. Copyright 2020, The Authors. (c) Soft modular glove integrating triboelectric-based tactile/strain sensing with pneumatic and thermal haptic feedback, for immersive human–machine interaction. Reproduced with permission [76]. Copyright 2022, American Chemical Society. (d) Flexible electromagnetic transducer for multimodal sensing and energy harvesting. Reproduced with permission [77]. Copyright 2019, The Author(s), under exclusive licence to Springer Nature Limited. (e) Ring-shaped wearable system integrating self-powered tactile and temperature sensors with vibro- and thermo-haptic feedback. Reproduced with permission [78]. Copyright 2022, The Author(s). (f) A flexible skin-mounted triboelectric patch enabling minimalist, self-powered human–machine interaction through direct gesture and motion control. Reproduced with permission [79]. Copyright 2019, Elsevier Ltd. (g) Zero-biased fingertip e-skin integrating triboelectric sensors with ionic-hydrogel interfaces for multimodal tactile perception without external bias. Reproduced with permission [80]. Copyright 2024, Wiley-VCH GmbH. (h) Bionic e-skin with anisotropic microstructures and iontronic sensing layers for multi-directional droplet sliding detection, enhancing robotic liquid-handling perception. Reproduced with permission [81]. Copyright 2024, The Author(s). (i) Single-piezoelectric EchoMG patch for dual ultrasound–EMG neuromuscular monitoring. Reproduced with permission [82]. Copyright 2024, The Author(s), under exclusive licence to Springer Nature Limited. (j) Hybrid piezo–triboelectric smart sock for energy harvesting and multimodal health sensing. Reproduced with permission [83]. Copyright 2019, American Chemical Society.

of approximately 3.5 mm, enabling bending-angle detection down to 30° with response times of 30–40 ms. The palm sensor, on the other hand, uses a 15 mm PDMS dome populated with 3 mm Eco-flex hemispheres to resolve shear forces in eight directions. Integrated PZT chips with lateral dimensions of ~8 × 5 mm and thickness reduced to 20 μm operate near a mechanical resonance of ~270 Hz, delivering tunable vibrotactile output under 6–12 V actuation. This design shows that system performance depends not on a single device parameter but on the precise matching of mechanisms to their optimal scales and frequency regimes. Triboelectric sensing ensures a high signal-to-noise ratio under low-frequency, large-displacement conditions, while piezoelectric actuation delivers low-power, high-efficiency output under mid-to-high-frequency, small-displacement conditions. Together, they provide broad bandwidth, high sensitivity sensing, and stable, controllable actuation. Demonstrations include multi-DOF gesture recognition, sliding detection, and real-time tactile feedback when combined with machine learning. As a result, the 96% recognition accuracy of the smart glove was partially enabled by this scale–mechanism–frequency co-design, offering a clear paradigm that links device physics, functional partitioning, and system integration for high-performance human–machine interaction.

The above synergistic paradigm provides a blueprint for further integration of richer interaction modalities. A soft modular glove that integrates multifunctional tactile units for simultaneous sensing and feedback, as shown in Figure 2c, extends this logic from dual-mechanism to multi-mechanism systems [76]. Each unit combines triboelectric tactile and strain sensors with pneumatic actuators and resistive thermal elements, allowing the glove to detect bending angles (0°–90°), pressures in the range of 1–5 N, and sliding-induced texture cues, while also providing localized vibro- and thermal-haptic stimulation. Typical tests were performed at 2 Hz contact frequency, and pneumatic actuation under ~120 kPa delivered displacements of 1–5 mm with corresponding tactile forces. Within a unified spatiotemporal 2 Hz contact frequency and millimeter-scale units, triboelectric sensing, pneumatic actuation, and thermal-resistive feedback are synchronized. This design shows that performance improvement no longer relies on extreme optimization of a single device, but instead on system-level fusion that achieves spatiotemporal

alignment of heterogeneous transduction mechanisms according to the target frequency band and human-scale dimensions. As a result, pressure and texture sensing are tightly coupled with tactile feedback, yielding a recognition accuracy of ∼96%.

When application scenarios impose extreme demands on integration density, thickness, and power consumption, the dominant transduction mechanism must undergo a fundamental shift. To achieve high-density and programmable arrayed tactile feedback while maintaining ultrathin flexibility (overall thickness of 2.5 mm), the epidermal VR system shown in Figure 2d abandons the previously used piezoelectric or pneumatic approaches and instead adopts an electromagnetic resonance mechanism [77]. As illustrated in Figure 2d, each millimeter-scale actuator consists of a Cu coil embedded in a PDMS ring and a nickel-plated neodymium magnet mounted on a polyimide cantilever, forming a compact vibration unit with an overall diameter of ∼18 mm and a thickness of 2.5 mm. Wireless near-field communication enables battery-free operation, with harvested RF power distributed across arrays of up to 32 actuators. By tuning the cantilever geometry, the system achieves resonant actuation in the 100–300 Hz band, which aligns with the most sensitive range of human mechanoreceptors, generating micrometer-scale displacements at power levels as low as 1.75 mW. The conformal soft platform adheres seamlessly to curved body surfaces, enabling programmable spatiotemporal vibration patterns for VR/AR immersion, prosthetic feedback, and gaming applications.

However, integrating multimodal feedback within the extremely limited space of the fingers constitutes another dimension of design challenge. A ring-shaped wearable system ("ATH-Rings") was devised that delivers vibro- and thermo-haptic cues while sensing finger motions, enabling coordinated bidirectional communication in augmented/virtual environments (Figure 2e) [78]. Within the ring-shaped space at the finger scale, triboelectric sensing, vibration (ERM), and thermal (NiCr) feedback are integrated. The key lies in the ERM actuator, which, by adjusting the driving voltage, can simultaneously tune frequency and amplitude within the 130–230 Hz range. This enables high-quality and tunable multimodal tactile feedback in an extremely constrained volume without increasing device size, thereby demonstrating the feasibility of mechanism integration and frequency control under strict spatial limitations.

Beyond conventional pressure and vibration sensing, high-precision discrimination of physical properties such as texture and hardness requires the introduction of entirely new sensing mechanisms. The zero-biased bionic fingertip e-skin couples a triboelectric vibration artificial neuron (TVAN) with an iontronic SPAN in a finger-mounted format (see Figure 2g) [80]. Its structure and scale are fingertip-appropriate: a patterned Ecoflex TVAN (∼200 μm, 100-μm pattern + 100-μm substrate) laminated over a PVA/PAAm/LiCl/Gly ionic hydrogel (∼300 μm), with active layers pre-formed to ∼20 × 30 mm and copper/aluminum electrodes cut to ∼25 × 35 mm; the honeycomb surface features a unit-cell size of 1 × 0.4 mm that boosts isotropic signal density. The device integrates triboelectric and ionotronic mechanisms. By operating strictly within the low-Hz band (1–4 Hz), it exploits the differential responses of these mechanisms to sliding and contact dynamics, thereby achieving multimodal perception of texture, hardness, and material properties. This reveals how ionotronic mechanisms, which are correlated with carrier performance, synergize with micro–mesoscopic structures to endow wearable devices with high-dimensional sensing capabilities approaching those of biological skin.

Bionic electronic skin is engineered to detect multi-directional droplet sliding, enhancing robotic perception for applications in complex liquid-handling environments [81]. The design combines anisotropic microstructures and high-sensitivity iontronic sensing layers, enabling the discrimination of droplet motion direction, speed, and contact dynamics. Such capability extends the sensory repertoire of robots, facilitating precise liquid manipulation and environment–object interaction awareness. A bionic electronic skin capable of precise multi-directional droplet sliding detection has been developed to enhance robotic perception and environmental adaptability. Built on co-layer interlaced branched electrode networks patterned on PTFE non-woven fabric and covered by a FEP negative triboelectric layer, the device forms a flexible, waterproof sheet that conforms to curved robotic limbs—demonstrated in 13 × 13 cm modules (with 10 × 10 cm and 7 × 7 cm variants) and an FEP thickness of ∼0.02 mm (see Figure 2h). In frequency terms, characterization explicitly probes droplet sliding frequencies of 0.5–2.5 Hz (with 1 Hz used for standard electrical measurements), from which average velocities ∼0.38–0.56 $m{\cdot}s^{-1}$ and accelerations ∼2.08–4.68 $m{\cdot}s^{-2}$ are derived under 45°–75° surface tilts. These scale–frequency choices enable robust dual-/multi-channel readouts that encode droplet position, direction, and speed, supporting real-time trajectory mapping, directional warning, and closed-loop leakage control in robotic demonstrations.

The above case illustrates a design philosophy where performance is enhanced through the superposition and fusion of mechanisms. However, in scenarios with extreme constraints on size, power consumption, or cost, deeply optimizing a single mechanism and maximizing its signal dimensionality is equally critical. In Figure 2f, a minimalist yet versatile human–machine interface is presented, employing a flexible, skin-mountable triboelectric patch to enable direct gesture and motion control without bulky electronics [79]. Within a palm-sized area, robust gesture recognition is achieved solely through a single-layer patterned electrode and low-frequency operation at 0.75–1.75 Hz, using spatial voltage ratio decoding. This demonstrates that, under clearly defined target frequency bands and scales, a minimalist physical architecture combined with intelligent signal processing is sufficient to support core interactive functions, offering a paradigm for resource-constrained ubiquitous applications. Furthermore, coupling such an efficient energy-conversion mechanism with system-level sustainability requirements points toward the ultimate form of "energy autonomy".

As shown in Figure 2b, a pair of deep learning-enabled smart socks is shown, where triboelectric textile sensors with millimeter-scale frustum structures are embedded into cotton fabric to detect foot pressure during gait cycles [75]. The device operates under low-frequency mechanical input from walking and running, typically at 1–2 Hz, converting these motions into electrical signals without external power. Each sock-sized sensor covers the full plantar area and sustains pressures, enabling accurate capture of heel–toe contact events and force distributions. By covering the full plantar area and sustaining pressures up to

200–300 kPa, they achieve >93% gait recognition accuracy across multiple activities, while harvested energy (0.32 mW at 1 Hz, 3.18 mW at 2 Hz) supports wireless data transmission.

Extending this concept, a self-powered and self-functional cotton sock (S^2-sock) demonstrates how hybridized energy harvesting can be integrated into everyday textiles by combining a PEDOT:PSS-coated triboelectric textile with embedded piezoelectric PZT thin-film chips (see Figure 2j) [83]. The triboelectric layer operates in a contact–separation mode to generate signals from foot motion, while the 20 μm-thick PZT chips (5 × 5 mm) provide complementary piezoelectric outputs under localized pressure. During dynamic activities such as jumping, the sock produced 1.71 mW (11 μW cm^{-2}) at 2 Hz, whereas individual PZT units generated up to 32 μW (128 μW cm^{-2}) under 12 N applied force at 1 Hz. In addition to harvesting energy, the hybrid device enabled gait recognition, pressure mapping, and sweat sensing, offering a multifunctional wearable platform for healthcare and sports monitoring. This integrated design of sensing and energy supply enables the system to perform sensing functions; the measured physical information serves simultaneously as both the excitation for sensing signals and the source for energy harvesting. Consequently, the sensing and energy modules are not simply stacked; rather, they share the same low-frequency mechanical stimuli and achieve deep coordination at the levels of system architecture and circuit design, thereby establishing the physical foundation for long-term and autonomous monitoring.

Formal discussed cases mainly focus on addressing Hz–kHz mechanical signals arising from human motion and tactile interaction, with device scales correspondingly adapted from centimeters to micrometers. However, when the sensing target extends from the body surface to the dynamics of deep tissues, the physical constraints of signal frequency and penetration depth drive the design parameters into a fundamentally different regime. Figure 2i illustrates the exploration of this direction through an ultrasonic, fully integrated single-transducer echomyography (EcMG) patch [82]. To achieve dynamic monitoring of tissues at depths up to ~6.6 cm, its operating frequency must be elevated to the MHz ultrasound range (1–5 MHz) with a ~4 MHz central frequency with ~1.6–1.8 MHz (−6 dB) bandwidth. For application-specific sound fields, the single transducer is sized 4 × 4 × 1 mm^3 for diaphragm monitoring and 4 × 0.5 × 1 mm^3 for forearm muscles. The physical nature of the target information—such as depth and resolution—determines the required signal frequency band. The generation and detection of such high-frequency signals almost inevitably demand piezoelectric transducer units with shorter wavelengths and smaller dimensions. This case demonstrates that the same design framework can be applied to explain technical pathway choices in high-frequency and microscale domains, highlighting its universality and coherence across different application spectra.

From tactile interaction to deep-tissue monitoring, the discussed cases collectively validate a core design methodology: the type and frequency of information required by applications (e.g., force, texture, depth imaging) together with system constraints (e.g., wearable location, power consumption) first determine the target signal frequency and the physical scale of the transducer. For instance, tactile feedback demands efficient actuation in the hundred-Hz range, where piezoelectric or electromagnetic mechanisms can be employed; whereas deep-tissue imaging requires ultrasound in the MHz range, enabling the use of micrometer-scale piezoelectric transducers. The decision chain from target frequency to scale and mechanism constitutes a deterministic decision pathway for designing high-performance flexible transducers.

3 | Acoustic Transducers Platform for Cross-Frequency

As flexible and wearable transducers progress from single-mode tactile sensing toward continuous interaction and deep information acquisition, application demands for signal types and penetration depth increasingly exceed the quasistatic and low-frequency mechanical regimes. Tactile feedback and surface sensing primarily depend on mechanical responses in the tens to hundreds of hertz; when applications shift to internal-structure imaging, tissue characterization, or cross-medium information transfer, acoustic waves—capable of long-range propagation in media while preserving spatial resolution—become the indispensable carrier. This application-level shift reorients transducer priorities from bendability and conformability toward the efficient generation, reception, and control of acoustic signals, thereby establishing acoustic transducers as a distinct and critical technical direction.

The evolution of acoustic transduction technology is rooted in the classical and physically intuitive mechanism of capacitive coupling. Its macroscopic implementation, exemplified by the electret microphone shown in Figure 3a, uses 1 mm-diameter air gaps with polyester films or polymer spacer layers to anchor performance in the audio band, with a resonance near 8.5 kHz and a sensitivity of about 3 mV/Pa at 1 kHz [84]. Capacitive mechanisms offer potential far beyond broadband sound-pressure sensing. When coupled with precise optical excitation and acoustic resonant structures, they can be substantially extended into highly specific analytical applications. One acoustic spectroscopy system, illustrated in Figure 3b, utilizes a cylindrical resonator with a 5 mm radius and a 100 mm length to stabilize the system on a single high-Q resonant mode near 1.58 kHz. This design converts the capacitive sensor into an extremely sensitive narrowband detection front end, achieving detection limits as low as 8.7 ppm for water vapor and 875 ppb for ammonia. This indicates that when pursuing extreme chemical detection sensitivity, design strategies shift away from broadband approaches and toward exploiting structural resonances to amplify signals. Nevertheless, there also exists a pathway to enhance quasi-static capacitive detection performance through direct optimization of electrode structures and readout circuits [85, 86].

The exceptional sensitivity of formal resonant systems comes at the cost of large volume and fixed bandwidth. To achieve broader bandwidth and on-chip integration within smaller dimensions, the capacitive transduction mechanism has undergone a paradigm shift to the MEMS. The perforated-backplate structure depicted in Figure 3c mitigates air-gap damping, producing a flat frequency response over 0.1–10 kHz and −42 dB V/Pa sensitivity at 1 kHz, while maintaining low power consumption and metal-oxide-semiconductor (CMOS) compatibility—features that have made this design dominant in consumer electronics

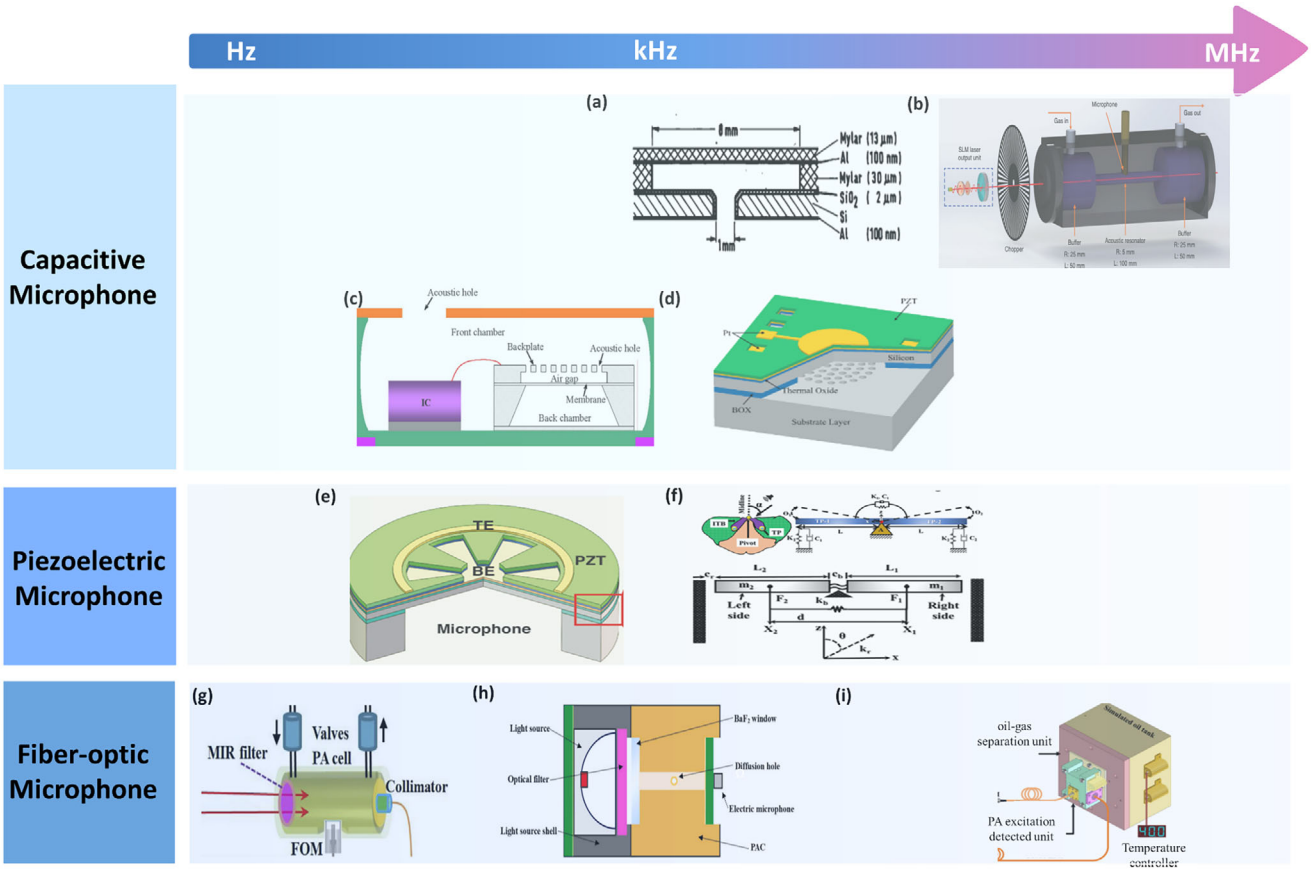

FIGURE 3 | Acoustic transducer platform for cross-frequency sensing. (a) Schematic of a silicon-dioxide backplate-electret microphone. Reproduced with permission [84]. Copyright 1984, AIP. (b) Schematic of a photoacoustic gas sensing system using a MEMS microphone. Reproduced with permission [87]. Copyright 2024, Elsevier. (c) Schematic of a MEMS capacitive microphone with a perforated backplate. Reproduced with permission [88]. Copyright 2008, IEEE. (d) Schematic of a hybrid MEMS microphone combining piezoelectric and capacitive transduction. Reproduced with permission [89]. Copyright 2024, IEEE. (e) Schematic of a piezoelectric MEMS microphone with electrode layers. Reproduced with permission [90]. Copyright 2025, Elsevier. (f) Mechanical model of an Ormia ochracea-inspired piezoelectric MEMS directional microphone. Reproduced with permission [91]. Copyright 2020, Springer Nature. (g) All-optical photoacoustic spectrometer for trace C_2H_4 detection in high-concentration CH_4 background. Reproduced with permission [92]. Copyright 2020, Elsevier. (h) Miniature mid-infrared photoacoustic gas sensor for detecting dissolved CO_2 in seawater. Reproduced with permission [93]. Copyright 2024, Elsevier. (i) Frequency-division-multiplexed fiber-optic photoacoustic sensor for in-situ C_2H_2/CH_4 detection in transformer oil. Reproduced with permission [94]. Copyright 2025, Elsevier.

[88]. However, at the microscale, the performance of a single capacitive mechanism encounters inherent physical bottlenecks. To simultaneously enhance sensitivity and linearity within the bandwidth while suppressing harmonic distortion, cutting-edge designs have begun to explore the synergy of different physical mechanisms within the same device. As shown in Figure 3d, the piezoelectric–capacitive hybrid MEMS microphone integrates two transduction principles: within the 100 Hz–10 kHz range, its capacitive and piezoelectric outputs exhibit sensitivities of −51 dB and −58 dB, respectively [89]. Through electrical signal fusion, the overall sensitivity is optimized to −47 dB, while the linear dynamic range is effectively broadened. This demonstrates how multi-physics coupling at the microscale can overcome the limitations of single mechanisms, achieving both bandwidth stability and sensitivity improvement.

This multiphysical design highlights the immense potential of piezoelectric materials at the microscale. In fact, when the piezoelectric effect is directly employed as the core transduction mechanism, devices can achieve superior performance owing to their high electromechanical coupling coefficients and the intrinsic property of force-to-charge conversion. A piezoelectric MEMS microphone, as shown in Figure 3e, incorporates single-crystal PZT thin films and enables resonance tuning between 76 and 106 kHz [90]. It employs a single-crystal PZT thin film reinforced by rib structures, successfully tuning its fundamental resonance frequency into the ultrasonic range. This clearly demonstrates that the piezoelectric pathway can more efficiently combine mechanical miniaturization with elevated operating frequencies, thereby achieving high-frequency and high-sensitivity responses that are difficult for capacitive mechanisms to attain at comparable scales. Moreover, the exceptional designability of piezoelectric microstructures can further enable bioinspired functionalities beyond conventional sound-pressure sensing. The MEMS design in Figure 3f, modeled after the fly Ormia ochracea, uses mechanically coupled diaphragms to enhance interaural phase and amplitude differences [91]. It achieves directional sensitivity in both rocking (≈7 kHz) and bending modes (≈12 kHz), maintaining accurate sound localization across 1–13 kHz with an equivalent input noise of ~25 dB SPL, close to the human

hearing threshold. Together, these designs show that microscale devices not only push operation toward higher frequencies but also enable new functionalities, such as directional selectivity.

Both capacitive and piezoelectric approaches are essentially electrical transduction mechanisms, ultimately converting acoustic signals into electrical outputs for readout. This shared nature imposes fundamental challenges to signal integrity, safety, and reliability in extreme environments such as strong electromagnetic interference, flammable or explosive atmospheres, corrosive conditions, or immersion in complex media like seawater. To overcome these inherent limitations, opticalreadout acoustic sensing offers a disruptive alternative based on a fundamentally different principle. In photoacoustic technology, optical excitation and acoustic detection are decoupled: laser modulation generates the acoustic signal, while purely optical methods perform the detection, thereby ensuring complete electrical isolation between the sensing and readout units.

In Figure 3g, a fiber Fabry–Perot microphone coupled to a nonresonant photoacoustic cell provides a flat response from 30 to 300 Hz, maintaining 200 ppb detection limits for ethylene even under 100% methane background [92]. The compact mid-infrared photoacoustic sensor in Figure 3h, with a cavity volume of only 73 μL, operates optimally at ∼11 Hz and achieves a detection limit of 0.72 ppm for dissolved CO_2 in seawater, while consuming only 350 mW and offering a response time of 3.5 min due to efficient water–gas separation [93]. For scenarios such as fault warning in power transformers, where simultaneous monitoring of multiple gases is required, Figure 3i employs frequency-division multiplexing. Two distributedfeedback (DFB) lasers are modulated at closely spaced frequencies of 1486 Hz and 1490 Hz to simultaneously excite the photoacoustic signals of C_2H_2 and CH_4, thereby achieving high-precision detection at the 0.1 $\mu L \cdot L^{-1}$ level [94]. These cases collectively demonstrate the irreplaceable value of optical acoustic sensing. Rather than representing an incremental refinement of electrical mechanisms, it offers a fundamentally distinct innovation by shifting the signal carrier at the very boundary where electrical approaches encounter physical failure. In doing so, it provides a definitive solution to challenges of specificity and robustness in advanced industrial and scientific applications.

Figure 3 thus encapsulates a fundamental design dialectic in acoustic transducers. While structural scaling physically dictates the accessible frequency boundary, the ultimate functional demands drive the selection and optimization of specific transduction mechanisms across these bands. Taken together, the examples illustrate this interplay not merely as a linear scaling law, but as a path-dependent technological evolution. Capacitive mechanisms, from original design to CMOS-integrated MEMS, have established the benchmark for audio-band sensing by prioritizing sensitivity, robustness, and cost-effective integration. Piezoelectric designs, leveraging their high-frequency electromechanical coupling, break through these frequency limits at the microscale to enable ultrasonic operation and novel functionalities like directional selectivity. When applications exceed the environmental limits of electrical transduction, fiber-optic photoacoustic systems shift to an entirely different physical principle, trading bandwidth for unmatched specificity and robustness in hostile or complex media. Underpinning this mechanistic diversification is the critical engineering of material systems—such as thin-film lithium niobate, aluminum nitride [50, 95–99], which modulate the efficiency and practicality of each mechanism at a given scale and frequency [57]. Consequently, the progression from capacitive to piezoelectric to optical platforms demonstrates that performance frontiers are expanded not by a single optimal design, but by strategically matching a mechanism's inherent physical advantages to the specific constraints and signals of the target application.

4 | Transduction-Enabled Metamaterials for High-Frequency Sensing

Metamaterial molecular sensors signify a fundamental leap in sensing technology—from acquiring low-frequency mechanical information to perceiving high-frequency molecular and electromagnetic signals. Unlike acoustic or tactile transducers that rely on mechanical deformation and structural scaling to capture signals in the Hz–MHz range, molecular fingerprint recognition directly corresponds to intrinsic vibrations and electronic transitions in the THz regime. This dramatic frequency expansion not only alters the nature of the signal carrier but also compels the transduction process to shift from mechanical degrees of freedom toward electromagnetic modes and even quantumcoherent states as the foundation of high-frequency sensing. The vibrational absorption wavelengths of many molecules fall in the mid-infrared (MIR) band and feature exclusive fingerprints, which enable infrared spectroscopy to be a reliable and powerful technique for chemical analysis and biomolecular characterization [100].

Against this backdrop, device scale is no longer merely an engineering parameter but a decisive variable linking information frequency with transduction mechanisms. When the target information lies in high-frequency electromagnetic bands, devices must achieve subwavelength localization and reconstruction of electromagnetic fields to effectively map molecular vibrations, carrier responses, or thermal radiation into readable signals via surface enhancement [101]. Optical metamaterials, exemplified by localized surface plasmon resonances (LSPR) and dielectric scattering, precisely manipulate field distributions to embed weak molecular absorption and scattering into a unified transduction framework, thereby enabling cross-degree-of-freedom coupling from mechanical, thermal, and carrier signals to optical outputs.

Thus, for molecular sensing transducers at the optical range, metamaterials function not merely as field-enhancing structures but as enabling transduction platforms. By reconstructing electromagnetic degrees of freedom across nano to microscale dimensions, they unify diverse physical processes into a single framework for perception and conversion, laying the foundation for highly sensitive and integrated sensing in the THz and higher regimes. LSPR-based metamaterial sensors were therefore the earliest practical realization, which can be seen as transducers that convert photon energy into molecule vibrational energy, e.g., surface-enhanced infrared absorption (SEIRA) and surface-enhanced Raman scattering (SERS). Within this trajectory, localized surface plasmon resonances were among the first mechanisms systematically introduced, initially enabling

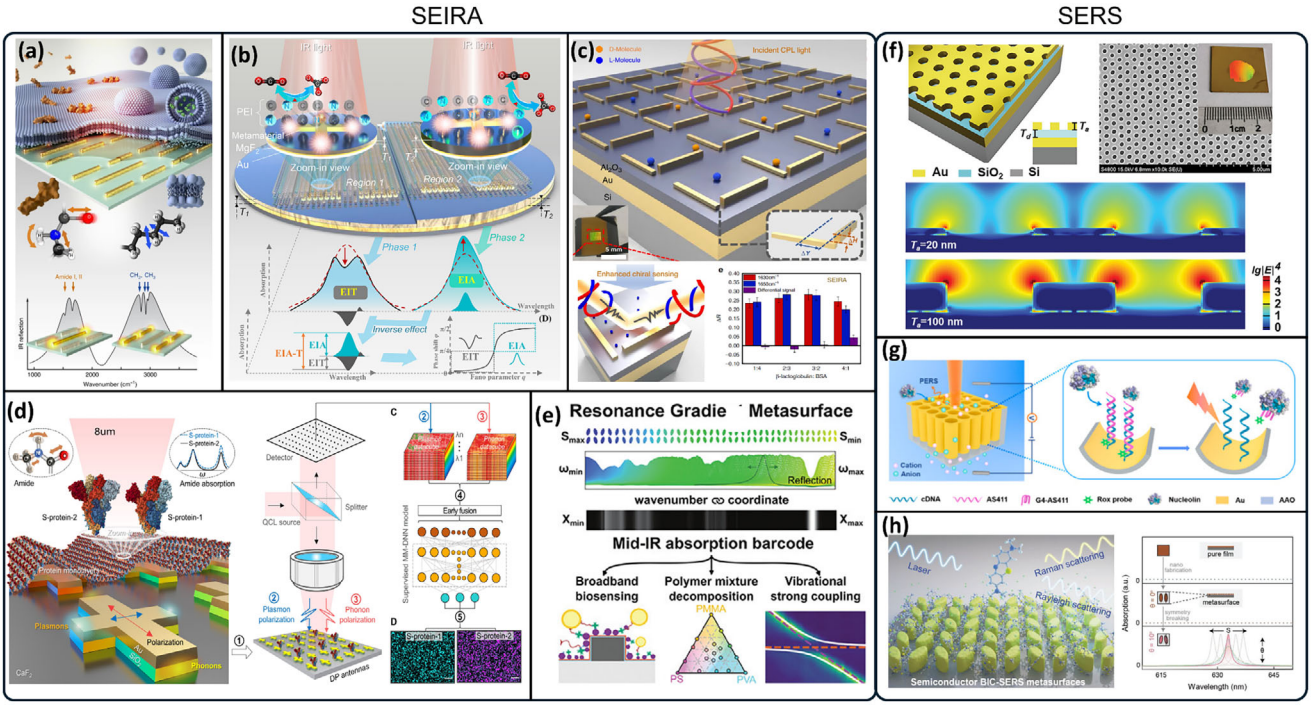

FIGURE 4 | Transduction-enabled metamaterials for SEIRA. (a) Multi-resonance metamaterial-based multi-molecule detection. Reproduced with permission [103]. Copyright 2018, Springer. (b) Fano resonance-based dual-phase detection. Reproduced with permission [104]. Copyright 2022, Wiley. (c) Metamaterial-enhanced chiral SEIRA sensing. Reproduced with permission [105]. Copyright 2023, Springer. (d) Machine learning assisted plasmon-phonon coupling metamaterial for protein detection. Reproduced with permission [106]. Copyright 2024, AAAS. (e) Gradient BIC metasurface for broadband SEIRA molecule fingerprint sensing. Reproduced with permission [107]. Copyright 2024, Wiley. Transducer-enabled metamaterials for SERS. (f) LSP-based SERS. Reproduced with permission [108]. Copyright 2021, Wiley. (g) Metallic nanotube-based SERS for molecule recognition. Reproduced with permission [109]. Copyright 2021, Elsevier. (h) Dielectric-based BIC resonance for SERS. Reproduced with permission [110]. Copyright 2024, Wiley.

surface-enhanced infrared absorption and opening the gateway to subsequent metamaterial strategies featuring higher quality factors, lower losses, and multi-degree-of-freedom coupling.

Among various kinds of novel physical mechanisms, LSPR is initially applied to realize SEIRA [102]. As shown in Figure 4a, a multi-resonant metamaterial composed of interlaced metal bars on calcium fluoride (CaF2) substrate, providing two plasmonic electric dipole modes at 1600 cm^{-1} and 2900 cm^{-1} with strong field enhancement ($|E/E0|^2 \approx 1000$), which can overlap the absorption peaks of amide I, amide II, CH_2 and CH_3 bonds [103]. By combining with spectral monitoring techniques, they realized real-time detection of the interaction process in the single-layer lipid membrane. However, the sensing performance of conventional LSPR mode still suffers from weak signal intensity, fabrication errors, and design constraints, which indicate that a breakthrough in the basic physical mechanism is still demanded. To this end, research has shifted toward the precise control of plasmonic modes. In 2022, inverse phases of electromagnetically induced transparency (EIT) and electromagnetically induced absorption (EIA) modes (Figure 4b), which are realized by tuning the thickness of the insulator layer in a metal-insulator-metal (MIM) configuration, were obtained to obtain constructive and destructive signals, thus effectively breaking the limitation of noise suppression [104]. In their research, two configurations with insulator thicknesses of 200 and 500 nm are respectively proposed to decrease and increase absorptivity, and an excellent limit of detection (LoD) performance of 13 ppm to CO_2 molecules was demonstrated with noise suppression of 30%. Furthermore, to achieve specific recognition of chiral molecules or species with overlapping absorption peaks, the design of metamaterials has expanded beyond intensity detection toward the dimensions of optical chirality and multi-parameter synchronous sensing. Luckily, the high design freedom enables metamaterials to support more modes. For example, in Figure 4c, a three-dimensional chiral metamaterial consisting of two vertically placed metallic bars with different thicknesses to support chiral LSPR resonance, which boosted the vibrational circular dichroism signal by 6 orders of magnitude [105]. In Figure 4d, an asymmetrical cross-shaped dual plasmon-phonon (DP) metamaterial that supports plasmon mode and phonon mode under linear polarized incident light along shorter and longer arms [106]. By simultaneously supporting plasmonic and phononic modes, the system can separately capture variations in the real and imaginary parts of the refractive index of the analyte. When combined with machine learning, this enables precise imaging of molecules with overlapping absorption peaks.

The above cases demonstrate the ability of metamaterials to deliver outstanding sensing performance at specific, discrete resonance wavelengths. However, the fingerprint characteristics of molecular spectra require sensing platforms with broadband coverage, as a single narrowband resonator cannot meet the demand for simultaneous multicomponent analysis in practical samples. To overcome this limitation, design strategies have shifted from unit-level optimization to system-level integration. Researchers

have proposed the concept of pixelated metamaterials, in which arrays of resonant units with varying scales are integrated on the same chip, stitching together discrete resonance peaks to achieve broadband coverage [111]. By splicing these discrete resonances to overlap a wide wavelength range, this design can provide a wideband fingerprint to recognize molecules. Subsequently, the incident angular dispersion was applied to equivalently construct spectra pixels [112]. Building on this foundation, gradient metasurfaces advance further by adopting unit structures with a one-dimensional continuous gradient (scaling factor from 1.0 to 3.5). This enables continuously tunable resonances across a broad infrared band from 3.12 μm to 10 μm, transforming molecular interactions into spectral barcodes readily recognizable by machine learning (Figure 4e) [107]. This evolution from a single resonance point to a continuous spectral surface marks the transition of metamaterial sensors from precise probes tailored to specific targets toward universal analytical platforms endowed with broadband fingerprint recognition capabilities.

Nevertheless, whether in discrete units or integrated systems, the performance of metallic metamaterials is ultimately constrained by their physical nature: thermal effects induced by Ohmic losses, intrinsic noise, and limited chemical stability. To break through these ceilings, fundamental innovation in both material systems and physical mechanisms is required. At this juncture, the theory of bound states in the continuum (BIC) provides a critical solution. BICs are special states that can be reached through scaling confinement, in which optical fields can be infinitely confined within dielectric structures without radiative loss. Their theoretical characteristics perfectly circumvent the Ohmic losses of metals, pointing the way toward optical field enhancement with extremely high quality factors (Q) and minimal thermal effects [113]. In 2024, one report applied BIC-driven TiO2 metamaterials as semiconductor SERS platforms (Figure 4h) [110]. The quasi-BIC mode provides a strong field enhancement of 103, and its resonant wavelength can be tuned by scaling the geometry size to match various wavelengths of stimulating lasers. The LoD of BIC metamaterial is improved to 10–8 M, two magnitudes higher than conventional TiO_2 substrates. Thus, the introduction of BICs is not merely a substitution from metals to dielectrics, but rather an elevation of the design paradigm as a transition from metallic resonances compromised by loss to the physical realization of theoretically lossless ideal resonances.

The core paradigm of metamaterials lies in manipulating optical fields through artificial structures, and their application potential is not confined to the infrared regime. In the field of Raman scattering, this paradigm likewise demonstrates the ability to disrupt conventional technological pathways. Raman signals originate from the inelastic scattering of photons, and their inherently small cross-section results in weak signal intensity [114]. Chemically synthesized noblemetal nanoparticles have served as the mainstream substrates for surface-enhanced Raman scattering (SERS). Although such substrates can provide enhancement through localized surface plasmon resonances, their performance is constrained by nanoscale fabrication precision: the randomness in particle size, morphology, and spacing leads to uncontrollable hotspot distributions, large fluctuations in enhancement factors, and poor reproducibility. This reflects the inherent bottleneck of the bottom-up synthesis approach when striving for macroscopic uniformity [14].

In contrast, metamaterial platforms based on nanofabrication fundamentally resolve the issue of uniformity at this scale by virtue of their top-down manufacturing precision. For example, in Figure 4f, a MIM metamaterial platform that supports the SPR mode, and a high enhancement factor of 106 was realized with a low relative standard deviation of 12.6% [108]. More importantly, the structural designability of metamaterials opens an entirely new dimension for functional integration. Studies have demonstrated that specific aptamer probes can be modified onto three-dimensional nanotube metamaterial structures, while the introduction of an external electric field enriches target molecules (such as nucleolar proteins), thereby constructing an intelligent biosensing interface capable of active recognition and signal switching [109]. As shown in Figure 4g, when the molecule nucleolin meets the aptamer AS411 with a carboxy-X-rhodamine (Rox) probe, they form a G-quadruplex (G4)-AS411 complex and detach from the nanotube wall, thus impairing the Raman signal of the Rox probe. This work highlights its potential in supporting cross-disciplinary applications. Moreover, semiconductor substrates are also widely used in Raman scattering applications due to their biocompatibility and stability. Similarly, dielectric metamaterials can also be used as SERS platforms.

In conclusion, this section clarifies a unifying causal framework underlying metamaterial-enhanced spectroscopic sensing, in which target molecular vibrational frequencies define the operational spectral window. This window constrains the viable resonance mechanisms, and the realizability of these mechanisms is ultimately governed by accessible device scales and integration limits. Within this framework, the historical transition from plasmonic to dielectric-based resonances reflects not a linear pursuit of stronger enhancement, but a sequence of constraint-driven choices responding to increasing demands on frequency selectivity, loss suppression, stability, and system compatibility. As a result, performance gains emerge primarily from reallocating frequency control from material-intrinsic responses to structure-defined resonances that are scalable and manufacturable.

Looking forward, further advances will depend on system-level co-design anchored to predetermined frequency and scale targets for the expansion of application scenarios, rather than rigid optimization of isolated physical effects. Inverse design enables direct matching between desired features and structural resonances [115], machine learning addresses quantitative interpretation of high-dimensional spectral data in complex environments, and integration with microfluidics and flexible platforms allows these frequency- and scale-specific mechanisms to be deployed in programmable and wearable systems [116]. The convergence of these tools within a unified design logic will determine whether metamaterial-based spectroscopy can progress from high-performance components to a robust technological foundation for information and health-related applications.

5 | Transducer-Driven Tunable Metamaterials for High-Frequency Modulation

The integration of MEMS with metamaterial transducers has opened a versatile route toward dynamically tunable platforms for high-frequency electromagnetic modulation [117, 118]. Unlike

static structures, MEMS-driven metamaterials can provide precise, reversible, and broadband reconfiguration across different frequency regimes, ranging from microwave to visible light. The actuation mechanisms—including mechanical, electrostatic, electrothermal, piezoelectric, and electrochemical schemes—offer varying advantages in terms of scalability, speed, and energy efficiency. In the following, we review representative demonstrations of MEMS transducer-enabled tunable metamaterials, organized according to their operating frequency domain.

At microwave frequencies, the relatively large unit-cell dimensions allow mechanical actuation by traditional motors. A notable example is the kirigami-inspired reconfigurable metasurface proposed in 2025, which achieves beam deflection and distribution in the 12–17 GHz range [119]. As illustrated in Figure 5a, the metasurface consists of rigid metallic panels joined at the corners, a dielectric spacer, and A-shaped resonant elements on the top surface. By mechanically rotating the metasurface (Figure 5b), the intersection angle can be tuned from 0° to 90°, resulting in a continuous modulation of anomalous reflection efficiency from 97.5% to 36.5%. Complementing this work, other researchers demonstrated a mechanically deformable metasurface resonant near 2.4 GHz [120]. Their design employed flexible acetate substrates patterned with MXene resonators. External stretching by motorized actuation shifted the resonance by more than 200 MHz. Furthermore, by employing a multiresonant design, the authors realized strain-induced tunability across the broader 4–10 GHz range. Together, these studies highlight that in the microwave domain, mechanically driven reconfiguration remains viable owing to the large feature sizes and robustness of the resonant units.

As the operating frequency increases into the millimeter-wave band, device miniaturization becomes essential, rendering bulky mechanical actuation impractical. Instead, MEMS actuation mechanisms such as electrostatic [58, 126–139] and electrothermal deformation [140, 141] dominate. A reported stacked MEMS metasurface absorber operating at 94 GHz for sensing and imaging applications [121]. As shown in Figure 5c, the device comprises a resonant metasurface layer, a dielectric spacer, an air gap, and a ground plane. The resonant layer efficiently absorbs. Millimeter waves heat MEMS cantilevers in the process. The thermally induced deformation modulates the air-gap thickness (Figure 5d), thereby tuning the working frequency. This platform enables millimeter-wave detection with an optical readout and a modulation rate up to 144 Hz. This transition from macroscopic mechanical actuation to MEMS-based electrothermal strategies underscores the importance of compact, integrated control mechanisms at millimeter-wave frequencies.

In the THz band, MEMS actuation continues to play a central role, with electrostatic, electrothermal, and electromagnetic mechanisms being the most widely employed. For example, an electrostatically reconfigurable metasurface operating from 0.4 to 0.8 THz for logic control of THz beams [122]. Their resonant unit, composed of symmetric split-ring resonators (SRRs) fabricated on an alumina-coated silicon substrate (Figure 5e), could be independently deflected by two electrode pairs, enabling XOR, XNOR, NOT, NAND, and OR logical functionalities (Figure 5f). Alternatively, an electrothermally actuated omega-ring metasurface with continuous tunability between 0.37 and 0.73 THz was introduced [142]. Joule heating induced by differential thermal expansion of Al and Al_2O_3 layers bends the suspended omega-ring structures downward, resulting in a maximum resonance tuning range of ~0.30 THz under 500 mW input power. These examples illustrate the versatility of MEMS actuation in the THz domain, enabling both logic-level functionality and broadband frequency modulation.

Moving into the MIR spectrum, nanometer-scale precision in actuation becomes indispensable. MEMS devices employing electrostatic control are particularly effective in this range. An electrostatically driven MEMS metasurface that reconfigures symmetry-protected bound states in the continuum (quasi-BIC) is proposed [123]. Their device, displayed in Figure 5g, comprising suspended metallic beams with etched elliptical nanoantennas, a tunable air gap, and a reflective metal substrate, achieved a 400 nm redshift in the resonance peak as the applied bias increased from 0 to 6 V. Figure 5h demonstrates the unbiased/biased state of the electrostatic MEMS metasurface. Similarly, A reconfigurable MIR emitter based on an electrostatically driven metasurface with an Al_2O_3 dielectric spacer was reported [143]. By varying the bias from 0 to 15 V, the absorption peak blue-shifted from 10.2 μm to 8.9 μm, while peak absorptivity increased from 0.5 to 0.95. Remarkably, this device achieved a modulation speed exceeding 110 kHz with a modulation depth of 23.7%.

At near-infrared (NIR) wavelengths, piezoelectric and electrostatic actuations are increasingly applied. Researchers have developed a piezoelectrically actuated MEMS metasurface for beam steering around 800 nm [124]. The structure employed a MIM configuration with a gold reflector, tunable air gap, nanobrick array, and silica substrate. By adjusting the air-gap width through piezoelectric actuation, efficient modulation of amplitude and phase was achieved, enabling polarization-independent beam deflection and two-dimensional focusing with modulation efficiency exceeding 50% (Figure 5i,j). Another seminal work employed electrostatic actuation to realize a dynamically tunable metasurface lens operating near 915 nm [144]. The device consisted of a fixed diverging metasurface and a movable focusing metasurface separated by a voltage-controlled air gap. With applied bias varying from 0 to 80 V, the focal length was tuned from 635 μm to 781 μm, achieving a corrected field of view up to 40°. These studies emphasize that NIR metasurfaces benefit from both piezoelectric and electrostatic actuation, offering multifunctional optical control within compact platforms.

At visible wavelengths, electrochemical actuation offers a powerful approach to achieve large, reversible geometric modulations. For instance, an electrochemically driven active metasurface composed of gold nanoantenna arrays separated from a gold mirror by a conductive polymer spacer of PEDOT:PSS is proposed [125]. As illustrated in Figure 5k,l, the polymer thickness expanded from 100 nm to 400 nm under bias voltages ranging from +1 to −1 V, with the reverse contraction achieved through opposite polarity. This swelling/shrinking process modulated both amplitude and phase of the reflected light, enabling high-contrast and dynamically reconfigurable beam shaping. This work highlights the potential of electrochemical mechanisms to provide efficient tunability in regimes where nanometer-level precision is mandatory.

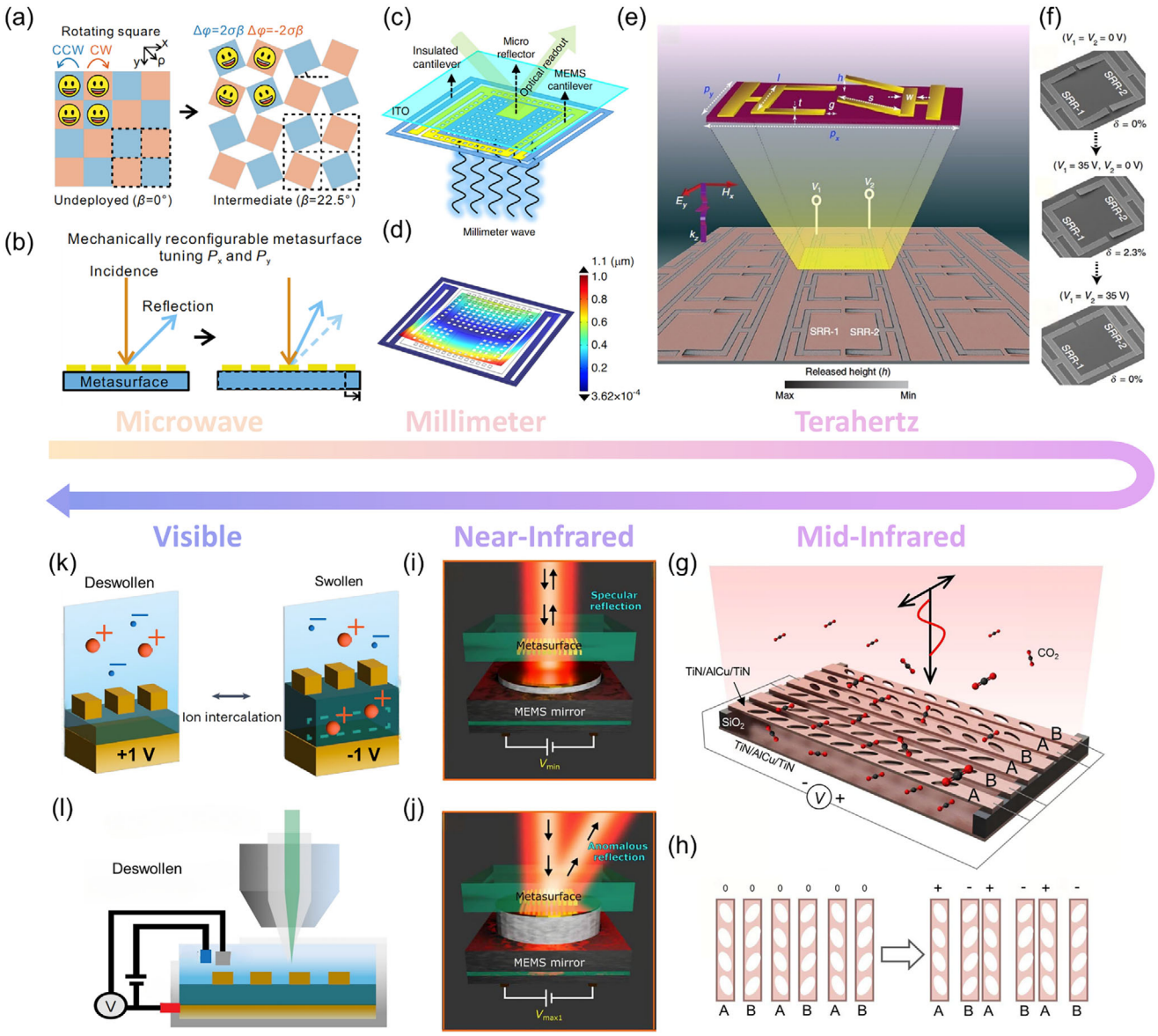

FIGURE 5 | MEMS/NEMS transducer-driven tunable metasurface with different working frequencies. (a) Tuning mechanism of mechanically deformable metasurface working in the microwave frequency band, (b) Schematic diagram of altering the beam deflection angle by adjusting the period. Reproduced with permission [119]. Copyright 2025, The Author(s). (c) Tuning mechanism of thermal-induced MEMS metasurface working in the millimeter wave band. (d) Schematic diagram of the pixel deflection of the metasurface. Reproduced with permission [121]. Copyright 2025, The Author(s). (e) Electrostatic MEMS metasurface operating in the THz band. (f) Three different working states of electrostatic MEMS. Reproduced with permission [122]. Copyright 2018, The Author(s). (g)Electrostatic MEMS metasurface operating in the Mid-infrared band, (h) Unbiased/biased state of the electrostatic MEMS metasurface. Reproduced with permission [123]. Copyright 2025, IEEE. (i,j) Schematic diagram of near-infrared metasurface based on piezoelectric MEMS under unbiased and biased conditions. Reproduced with permission [124]. Copyright 2021, The American Association for the Advancement of Science. (k) A schematic diagram of a mechanically tunable metasurface in the visible light band, based on swelling/deswelling induced by ion insertion, (l) Schematic diagram of driven electrodes for the metasurface. Reproduced with permission [125]. Copyright 2024, The Author(s).

Across the electromagnetic spectrum, MEMS-driven tunable metamaterial transducers have demonstrated remarkable adaptability in frequency modulation, beam steering, logic operations, and spectral control. At lower frequencies (microwave and millimeter-wave), mechanical and electrothermal actuations dominate due to larger unit-cell dimensions, while in the THz range, MEMS-enabled electrostatic and electrothermal mechanisms enable both broadband tunability and functional logic operations. As the frequency advances toward the infrared and visible regimes, nanometer-scale precision requires electrostatic, piezoelectric, and electrochemical strategies, enabling fast modulation and compact multifunctional integration. Looking forward, challenges remain in achieving higher modulation speeds, minimizing power consumption, and ensuring large-scale integration with complementary CMOS processes. The convergence of MEMS actuation with emerging material platforms and AI-assisted design frameworks is expected to expand the functional landscape of tunable metamaterials further, ultimately paving the way for transformative applications in communication, imaging, sensing, and quantum photonics.

6 | Optical Transducers for Advanced Chip-Level Sensing

The evolution of optical sensing reflects a shift from single-nanostructure functionality toward chip-level multifunctional cooperative systems. Nanophotonic structures such as metasurfaces, through subwavelength control of electromagnetic degrees of freedom, have demonstrated advantages in high-frequency field shaping for molecular fingerprint [145] and chirality detection [14]. Yet, as the focus moves from field enhancement to stable information acquisition, parallel readout, and efficient processing, the interface between discrete structures and macroscopic systems has become a bottleneck. Consequently, research has turned to on-chip sensors, emphasizing not further local enhancement of individual structures but the integration of field generation, modulation, sensing, and signal transduction into scalable, low-power, and fabrication-compatible architectures [33, 146, 147].

When transducers for optical sensing are designed in device feature sizes that range from one to several hundred micrometers, a common paradigm dominates. Researchers employ the inertia or elastic deformation of micromechanical structures as an intermediate transduction medium, mechanically amplifying external perturbations and then reading signals through changes in optical path length, phase, or intensity. This approach offers extremely high displacement sensitivity, yet its fundamental limitation arises from classical mechanics. The effective mechanical mass and elastic coefficient jointly determine the intrinsic frequency, confining the optimal operating bandwidth to the kHz range—typically below 20 kHz—and thereby imposing an inherent tradeoff between sensitivity and response speed [22, 148].

This paradigm of mechanical coupling with optical readout is most prominently embodied in the classical inertial sensors. For example, the core of a microfiber knot resonator accelerometer is an optical cavity formed by coupling a fiber ring of only about one micrometer in diameter with a microelectromechanical cantilever beam roughly 200 μm long. Acceleration induces deformation of the cantilever, thereby modulating the optical path length within the cavity, yielding a spectral sensitivity of 29 pm/g and an intensity sensitivity of 654.7 mV/g. Its high quality factor of 8200 ensures low-noise detection, but the system's dynamic response is confined to the mechanical resonance frequency range [149]. Similarly, an accelerometer featuring a one-dimensional photonic crystal with a micrometer-scale air-gap defect layer exploits the deformation of its asymmetric lattice and air-gap beam. This design achieves a resonance wavelength shift of 10.6 nm/g, a measurement bandwidth from 0 to 4 kHz, and a linear range up to ±25 g [150]. In another example, the microring resonator accelerometer further miniaturizes the optical sensing unit to a micrometerscale silicon ring. By detecting variations in coupling distance, it achieves a sensitivity of 1.56 nm per g of acceleration, with a dynamic resonance frequency of about 13 kHz [151]. These designs demonstrate that, at the microscale, carefully designed massspring systems can reliably convert inertial forces into measurable optical displacements, enabling high linearity and low-noise sensing. However, the device response speed, together with its bandwidth, is inevitably constrained by the intrinsic mechanical resonance frequency.

The principle of optical sensing based on mechanical deformation naturally extends to detecting weaker vibrations such as sound waves. A representative example is the vertically integrated optical MEMS acoustic sensor, which monolithically integrates a Vertical-Cavity Surface-Emitting Laser (VCSEL), photodetector, and diffraction grating to sense minute displacements induced by sound pressure, thereby achieving highSNR detection across the entire audio band [152]. Even magnetic fields can be indirectly measured by driving microstructures into rotation via magneto torque. The microdisk cantilever torsional magnetooptical sensor follows this principle, with a torque sensitivity corresponding to an equivalent frequency of 7.2 MHz [153]. These cases illustrate that any physical quantity convertible into a force or torque acting on a micromechanical structure can be incorporated into the mechanical-mediated sensing framework.

Chemical sensing can likewise be incorporated into this framework, with the key lying in converting molecular recognition events into measurable mechanical deformations. A micro optoacoustic CO_2 sensor exemplifies such indirect transduction. When the target gas absorbs modulated light, it undergoes periodic thermal expansion, exciting acoustic pressure waves within a miniature sealed cavity of 73 μL. These waves are ultimately detected by a microphone, achieving a detection limit of 0.72 ppm [93]. An even more direct transduction is embodied in the nanomembrane-film (NMF) sensor in Figure 6a in a piezoresistive approach. Molecular adsorption-induced deformation redistributes stress, modulating the resistance of a high-gauge-factor ITO layer. A Pd surface coating enhances the response to hydrogen in the 0.01–0.1% range, significantly boosting electromechanical conversion efficiency [154]. Both chemical sensing pathways, whether relying on volumetric changes in photoacoustic cavities or stress variations in sensitive membranes, depend on relatively slow physicochemical processes such as adsorption–desorption or thermal diffusion to drive mechanical responses. As a result, their operating frequencies are confined to the range of hertz to hundreds of hertz. This highlights that within the mechanical coupling paradigm, the pursuit of very high chemical sensitivity often requires sacrificing response speed.

When the sensing target shifts from a single physical or chemical quantity to complex spectral information, the mechanical-mediated paradigm evolves into its most refined form. Researchers begin to employ movable micromechanical actuators to replace the macroscopic moving parts of traditional spectrometers. The MEMS mid-infrared spectrometer in Figure 6b employs an electrostatically tunable waveguide coupler to modulate the optical path difference in a Fourier transform infrared (FTIR) spectrometer, attaining a resolution of 3 nm across the 3.7–4.05 μm band and identifying N_2O absorption [155]. Pushing the limits of sensitivity, a silicon photonic computational spectrometer (Figure 6c) utilizes a 0.35 μm-wide waveguide and a 33 μm-long cantilever. A deep denoising autoencoder enhances its resolution from 1.2 nm to 0.4 nm at a 30 dB SNR, outperforming traditional FTIR in resolution–noise trade-off [61]. Compared to traditional FTIR designs, this miniaturized platform delivers superior resolution at lower noise levels, demonstrating the benefits of algorithm co-optimization. Meanwhile, a high-performance planar Fourier transform spectrometer achieves a resolution of 0.2 nm using a 22 nm coupling-gap comb actuator [162]. The common feature

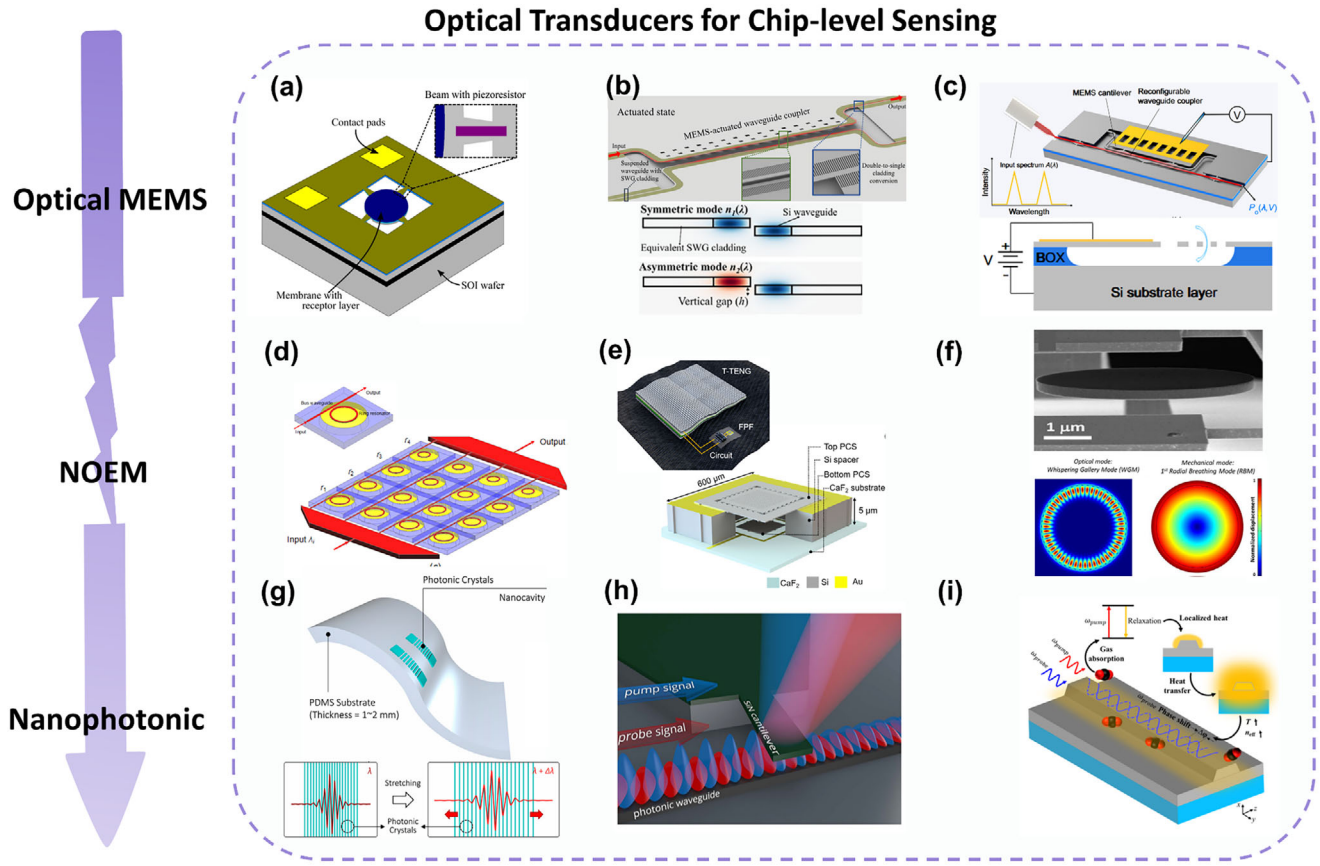

FIGURE 6 | Optical Transducers for Advanced Chip-level Sensing. (a) Microscale Si nanomechanical membrane–flexure gas sensor with indium tin oxide (ITO) piezoresistive readout. Reproduced with permission [154]. Copyright 2024, IEEE. (b) MEMS computational spectrometer using electrostatic cantilevers for tunable waveguide coupling and broadband reconstruction. Reproduced with permission [155]. Copyright 2022, American Chemical Society. (c) Microscale triboelectric-actuated Fabry–Pérot photonic-crystal-slab filter with tunable air gap for mid-IR spectroscopy. Reproduced with permission [61]. Copyright 2024, The Author(s). (d) Hybrid optomechanical pressure sensor combining a Si diaphragm and a nanoscale ring resonator for wavelength-shift readout. Reproduced with permission [156]. Copyright 2012, Optical Society of America. (e) Nanoscale GaAs/AlGaAs optomechanical disk resonator with GHz mechanics and high-Q optics for temperature and humidity sensing. Reproduced with permission [157]. Copyright 2021, Elsevier Ltd. (f) 1D photonic-crystal cavity embedded in flexible PDMS for optical modulation and strain sensing. Reproduced with permission [158]. Copyright 2023, The Authors. (g) All-photonic NEMS biosensor using optical-gradient-force actuation of a suspended nanobeam with MHz resonance readout. Reproduced with permission [159]. Copyright 2023, by the authors. (h) Pd/Au nanophotonic mechanical cavity for hydrogen-induced deformation and interference-based spectral modulation. Reproduced with permission [160]. Copyright 2015, The Author(s). (i) Nanophotonic photothermal transducer based on a lithium-niobate waveguide, converting gas absorption into phase modulation via the thermo-optic effect. Reproduced with permission [161]. Copyright 2024 Elsevier B.V.

of these miniature spectrometers is that they transform spectral encoding, the process of information extraction, into a problem of mechanically controlling the position of micrometer-scale optical elements. Their outstanding resolution and stability stem from precise mechanical motion enabled by micro/nanofabrication, yet their spectral acquisition speed, typically in the millisecond-to-second range, is fundamentally limited by the response and stabilization time of mechanical actuators. To break through the frequency limitation imposed by mass and elasticity, it is essential to fundamentally reduce or eliminate dependence on macroscopic mechanical degrees of freedom. This necessity has directly driven the technological paradigm toward evolution at the nanoscale.

This physical principle is directly manifested in optical sensing with movable nanostructures. The tunable photonic crystal membrane Fabry–Pérot spectrometer in Figure 6d demonstrates this shift. Electrostatic actuation combined with a nanoscale triboelectric generator induces membrane deformation, enabling mid-infrared spectral detection within the 4.13–5.61 μm range and resolving the acetone absorption peak at 5.75 μm [156]. The key to this design lies in replacing the bulky movingmirror system of traditional spectrometers with a nanomembrane. Its minute mass enables faster response to actuation, thereby laying the foundation for dynamic spectral detection. Similarly, the ring resonator pressure sensor follows the path of mass reduction. It replaces the bulk material diaphragm with a silicon film only 20 μm thick, coupled to a ringshaped optical cavity with a cross-section of 450 nm by 220 nm. Owing to the significant reduction in mechanical mass, the sensor maintains a high sensitivity of 1.47 pm per kPa while successfully pushing its mechanical resonance frequency into the MHz range [157]. This confirms the feasibility of optimizing sensitivity and bandwidth through nanoscale constraints.

Further studies show that when structural features shrink below 100 nm, devices achieve very high mechanical quality factors and strong energy localization. A slot-type nanooptoelectromechanical system (NOEMS) with a 50 nm air slot demonstrates strong subwavelength optomechanical coupling, reaching an optical quality factor of 9 000 000 and a sensitivity of 4.2 nm/μN, with optimal operation in the kHz range [163]. Such devices indicate that nanoscale mass reduction not only enhances operating frequency but, through strong field localization, also opens new avenues for ultra-sensitive sensing. However, once mechanical inertia is overcome, these approaches face new bottlenecks arising from the thermal noise limit of displacement detection and the rate of electromechanical transduction.

In the paradigm of direct optical field control, the logic of functional integration in nanophotonic devices undergoes a fundamental shift. The focus moves from assembling multiple mechanical sensing units to programming and multiplexing the optical modes supported by a single nanophotonic structure. By designing subwavelength geometries, typically smaller than one-tenth of the operating wavelength, distinct modes with varied spatial distributions, polarization states, or frequency responses can be excited within the same device. These modes respond selectively to external perturbations such as temperature, stress, refractive index, or molecular adsorption. For example, a flexible 1D photonic-crystal cavity embedded in PDMS further adds strain-tunable optical modulation while preserving compactness with a sensitivity of 2×10^{-4} strain, thereby extending the readout frequency toward THz-band optical modes [164]. This paradigm thereby integrates multiple sensing channels into one shared optical field and platform. This mode-based integration not only increases functional density but also provides inherent advantages of high speed and immunity to electromagnetic interference, since all signals originate in the optical domain.

The most direct manifestation of this mode-multiplexing strategy is the realization of high-precision, simultaneous, and decoupled sensing of multiple physical parameters within a single miniature device. A representative example is the GaAs/AlGaAs nanodisk structure shown in Figure 6f, which, at the micrometer scale, supports both optical whispering-gallery modes and mechanical radial breathing modes [158]. This case illustrates the core mechanism of functional integration in nanophotonics, where the couplingcoefficient matrix between different modes and external parameters enables the effective decomposition of complex physical perturbations into independent optical signal channels, thereby achieving parallel high-precision sensing.

Further functional integration requires devices to possess not only passive sensing capabilities but also the ability to actively modulate the optical field, thereby establishing a closed-loop system between sensing and actuation. This demand has driven the deep incorporation of electro-optic (EO) and thermo-optic (TO) effects into nanophotonic structures. A liquid-crystal fiber-tip device with a 5 μm deformed helix ferroelectric (DHF) layer and a nanograting offers hysteresis-free phase modulation at 1.55 μm under a low 3 V drive [165]. Similarly, a graphene/Au nano-opto-mechanical resonator exhibits a current sensitivity of 18.04 Hz/mA^2 with a response time of ∼2 ms [166]. The ability to miniaturize EO modulation units and monolithically integrate them with photonic devices forms the foundation for future on-chip programmable sensing systems and optical computing units.

Extending the capability of optical field manipulation from static sensing to dynamic actuation has led to the emergence of nano-actuators based on optical gradient forces and photothermal effects. An all-photonic NEMS biosensor in Figure 6g uses optical-gradient-force actuation of a suspended nanobeam for MHz-resonance readout, reaching a minute pressure detection limit of a pressure detection limit of 1.6‰ [159]. A PDMS-embedded nanorod-array cavity reduces mode volume and attains high strain sensitivity, extending coverage toward THz-band optical modes [167]. Alternatively, a high-Q nanobeam cavity (0.055 μm^3 volume) senses refractive-index perturbations and nanoparticles through Bloch-mode engineering [168]. Building upon this approach, a nanobeam cantilever, shown in Figure 6h, demonstrates dynamic operation. It generates MHz-level vibrations under excitation by 1.31 μm pump light, which are read out by 1.55 μm probe light, enabling single-molecule mass sensitivity detection in a vacuum environment [160]. These designs eliminate external electronic driving and rely solely on incident light to simultaneously achieve actuation and readout. As a result, the device attains extremely low energy consumption, reduced system complexity, and minimal electromagnetic noise, thereby highlighting the potential ultimate capability of alloptical integration.

Ultimately, this highly integrated design philosophy has been successfully applied to the particularly challenging field of chemical sensing, with the central approach bypassing any mechanical intermediary and directly exploiting the interaction between optical fields and molecules. The scheme shown in Figure 6i represents a milestone: a lithium niobate nanophotonic waveguide with a subwavelength cross-section achieves an effective interaction length of 91.2 mm through a meandering geometry. When the modulated pump laser is absorbed by adjacent CO_2 molecules, the resulting minute heat induces an immediate refractiveindex change in the waveguide via the strong thermooptic effect, which is precisely captured by another probe laser using interferometric detection. Operating at kHz modulation frequencies and optimized with an integration time of 190 s, the system ultimately achieves a CO_2 detection limit of 870 ppm [161]. This work delineates a clear pathway: by deeply integrating high-Q optical nanocavities, efficient functional materials, and low-noise heterodyne detection techniques on a chip, nanophotonics can enable high-performance on-chip spectroscopic analysis systems that operate without mechanical motion and chemical features.

The data in Table 1 provide clear scalinglaw evidence for the paradigm shift from mechanical coupling to optical field manipulation. The results reveal that when device feature sizes shrink from the micrometer to the nanometer scale, the dominant operating frequency undergoes an order-of-magnitude leap, transitioning from the kHz–MHz mechanical domain to the THz optical domain. Micrometerscale devices, including those based on capacitive, electrostatic, or optomechanical coupling, are constrained by mechanical inertia, with operating frequencies limited to the range of 734 Hz to about 7 MHz [153, 169]. In contrast, nanometer-scale devices, such as nanoantennas and waveguide biosensors, operate predominantly between 2 THz and beyond 100 THz [145, 170–173]. This pronounced frequency

TABLE 1 | Characteristics of diverse optical sensing transducers.

Transducer		Sensing frequency	Device CD	Refs.
Mechanism	**Device**			
Capacitive	MEMS Accelerometer	734 Hz	Millimeter-scale	[169]
Electrostatic	Integrated Cavity Optomechanical Accelerometer	20 kHz	Micrometer-scale	[175]
Electrostatic	Reconfigurable diffraction grating array	0.97 – 2.28 THz	Micrometer-scale	[176]
EO	Fluidic Resonator	24.26 MHz	Micrometer-scale	[177]
Magnetomechanical	Whispering-Gallery Mode Disk Torque Sensor	∼7 MHz	Micrometer-scale	[153]
Magnetomechanical	Optomechanical Oam Detector	∼5 MHz	Micrometer-scale	[178]
Optical Transduction	Mid-Infrared Waveguide-Based Photonic Biosensor	THz	Nanoscale	[171]
Optical Transduction	AI-Enhanced MIR Lab-On-A-Chip Biosensor	78.8–81 THz	Nanoscale	[145]
Optical Transduction	MIM Nano-Antenna Array Biosensor	30–100 THz	Nanoscale	[170]
Optical Transduction	Metal–Organic Framework Polymers Multi-Hotspot Nanoantenna Biosensor	∼37– 50 THz	Nanoscale	[172]
Optical Transduction	Wavelength-Multiplexed Hook Nanoantennas Biosensor	∼33– 50 THz	Nanoscale	[173]
Optical Transduction	Quasi-Bics Metasurface Biosensor	∼2 THz	Micrometer-scale	[179]
Optical Transduction	Dual-modal encoded SERS	THz	Nanoscale	[180]
Optical Transduction	flexible PMDS SERS	THz	Nanoscale	[181]
Optomechanical	Slot-Type Photonic Crystal Cavity Inertial Sensor	71.3 kHz	Micrometer-scale	[41]
Optomechanical	Microdisk Cavity Optomechanical Ultrasound Sensor	98 kHz – 315 kHz	Micrometer-scale	[182]
Optomechanical	Fiber Cantilever Accelerometer	23.3 Hz	Millimeter-scale	[183]
Optomechanical	Mass Spectrometry	44.9 MHz	Micrometer-scale	[184]
Optomechanical	Dual Nano-Ring Resonator	THz	Nanoscale	[185]
Optomechanical	Zipper Cavity Optomechanical Accelerometer	27.5 kHz	Micrometer-scale	[186]
Optomechanical	double-membrane photonic crystal cavity	95 kHz	Micrometer-scale	[187]
Photonic	Resonant Fiber Optic Gyroscope	10 MHz	Millimeter-scale	[188]
Piezoelectric	Fiber Bragg Grating Acousto-Optic Sensors	2.25 MHz	Millimeter-scale	[189]
Pyroelectric	pyroelectric SERS	∼50 THz	Nanoscale	[190]
Thermal	Microring Resonator Thermal Detector	THz	Micrometer-scale	[191]
Thermal	Optomechanical Cavities Thermal Sensor	MHz	Micrometer-scale	[192]
Thermal	Fiber Current Sensor	221.4 kHz	Micrometer-scale	[166]

discontinuity signifies a fundamental shift in the underlying physical mechanism, from detecting low-frequency mass vibrations (phonon modes) to directly probing molecular bond vibrations or electronic transitions (photon modes) [61, 167]. The reduction to deep-subwavelength scales is specifically intended to excite and localize these high-frequency photon modes that encode rich information. Design frameworks such as coupled-mode theory [106, 170, 174] play a pivotal role in this context. They provide methodological guidance for researchers to employ structures to precisely program optical fields at the nanoscale, thereby enabling mode multiplexing, conversion, and recognition.

Therefore, the core logic of functional integration in nanophotonic sensors lies not in the simple aggregation of multiple device functions, but in the programmable control and efficient reuse of optical fields within the optical frequency domain as an established information platform. To meet the extreme demands on information dimensionality and resolution in applications such as biochemical fingerprinting, single-molecule detection, and quantum-state sensing, sensing systems must transition from mechanically limited, low-frequency dynamical regimes to the optical frequency domain, where high-frequency intrinsic information can be directly accessed. Only when system scales permit direct manipulation of photonic behavior can sensing escape the spectral bottlenecks imposed by mechanical inertia and enable direct acquisition and processing of the most fundamental, highest-frequency material information. This transition represents not merely device miniaturization, but a fundamental upgrade in the information hierarchy of sensing systems, from the mechanical domain to the optical domain, thereby establishing the physical basis for high integration density and multidimensional sensing.

7 | Transducers for Optical Modulation

Within a unified transduction framework, optical sensing and optical modulation play fundamentally distinct roles in the frequency domain. Optical sensors passively map the intrinsic frequencies of external signals, with their operating bands determined by the target phenomena, ranging from low-frequency mechanical perturbations and acoustic vibrations to THz molecular fingerprints. In this process, transducers sequentially invoke mechanical, electromagnetic, or quantum degrees of freedom to encode external frequencies into readable optical signals. In contrast, optical modulators are designed to actively generate and precisely control the temporal scales and spectral structures of optical carriers, embedding electrical or mechanical drive signals directly into the optical field. This capability defines the attainable data rates [193], energy confinement [60, 194], and functional complexity of the system [195].

Because of this disparity in frequency authority, optical modulation places substantially more stringent demands on transduction mechanisms. For optical MEMS transducers, external control signals can be converted into mechanical deformation and subsequently mapped onto changes in optical path length or phase [116]. As a result, the achievable modulation bandwidth is inherently constrained by mechanical degrees of freedom and is typically limited to the kHz regime. As application requirements progress toward GHz and even THz carrier control, such mechanically mediated pathways become difficult and insufficient. Modulation must instead bypass mechanical inertia and directly access electromagnetic degrees of freedom, or exploit their coupling with acoustic modes, charge carriers, and quantum states. This transition reflects a fundamental shift from mechanically dominated transduction toward electromagnetic and quantum-coherent degrees of freedom, thereby repositioning optical modulators as central nodes of multiphysics cooperation rather than passive amplifiers of isolated effects.

In this context, transducers for optical modulation are not merely extensions of sensing devices but rather essential units within a unified transduction framework that perform the function of programming. By reconstructing the coupling between optical and driving fields at deeply subwavelength scales, they transform optical systems from passive interfaces that perceive external frequencies into active engines capable of defining frequency, bandwidth, and information flow, while continually striving for higher speed, lower energy consumption, and richer functionality. This distinction establishes the physical boundary between optical sensing and optical modulation and provides the foundation for systematic comparisons of different modulation mechanisms in terms of frequency, power consumption, and functional complexity [196–198].

7.1 | Transducers for Advanced Optical Modulation

In the domain of microscale optical modulation, device dimensions typically range from several hundred micrometers to a few millimeters. The prevailing design paradigm relies on mechanical intermediaries, whereby external energy drives microstructures to produce displacement or deformation, indirectly modulating the optical path length or reflection angle. This paradigm faces a fundamental constraint: the maximum operating frequency of the device is determined by its mechanical resonance, which scales with the square root of the effective mass and elastic coefficient of the structure. Moreover, the practical modulation bandwidth is not only limited by this resonance but is also strongly influenced by mechanical damping and thermal dissipation. Consequently, all technological approaches must inevitably balance tradeoffs within a multidimensional parameter space defined by resonance frequency, displacement amplitude, driving voltage, and fabrication compatibility.

Thermal actuation provides large displacement and versatile functionality, suitable for programmable imaging. Its principle relies on Joule heating-induced thermal expansion to drive microstructural deformation. For instance, an electrothermalactuated photonic crystal lens can achieve a significant strain of 1.4% [199]. However, this case also demonstrates that the thermooptic mechanism, by sacrificing response speed, achieves enhanced integration convenience and substantial optical modulation depth.

To enhance modulation speed, electrostatic actuation offers a pathway into the tens of kHz regime, albeit at the cost of requiring high driving voltages. The underlying mechanism relies on Coulomb forces between conductors to induce mechanical motion for optical modulation. This approach enables devices

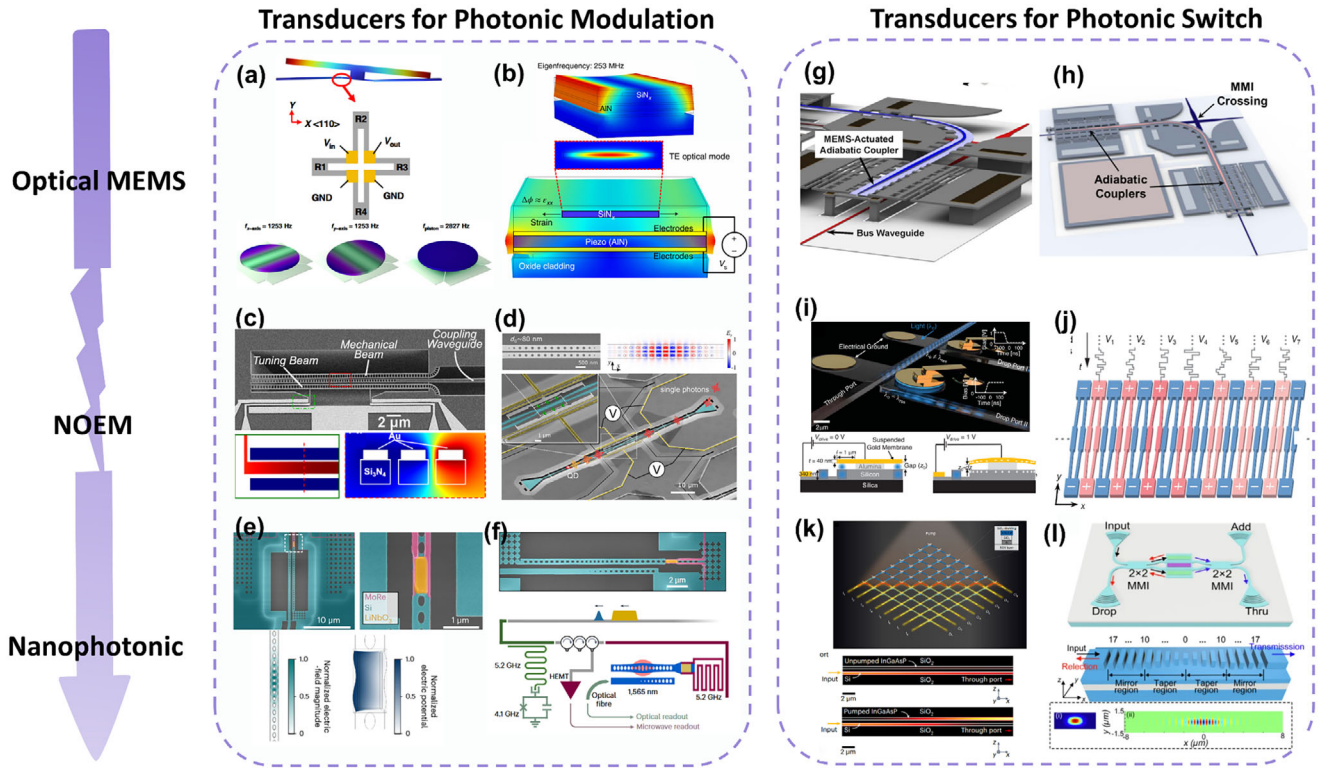

FIGURE 7 | Transducers for Optical Modulation. (a) MEMS fast steering mirror, 10 mm aperture, piezo drive with piezoresistive feedback, >2 kHz beam control. Reproduced with permission [200]. Copyright 2025, The Author(s). (b) AlN-on-SiN microscale phase modulator on CMOS, up to 253 MHz in visible–NIR. Reproduced with permission [147]. Copyright 2021, The Author(s). (c) Nanoscale electrostatic plasmonic nanogap modulator for mid-IR reflection control across 14–18 μm. Reproduced with permission [202]. Copyright 2018, Author(s). (d) Nanomechanical photonic-crystal cavity filter, electrostatic drive, tens-of-MHz resonance for quantum-dot single-photon selection. Reproduced with permission [63]. Copyright 2020 WILEY-VCH Verlag GmbH & Co. KGaA. (e) $LiNbO_3$-silicon piezo-optomechanical interface coupling a 5.07 GHz mechanical mode for microwave–optical transduction. Reproduced with permission [203]. Copyright 2023, The Author(s). (f) Nanoscale piezo-optomechanical transducer with $LiNbO_3$ nanobeam cavities, GHz-band for superconducting-qubit optical readout. Reproduced with permission [204]. Copyright 2025, The Author(s). (g) Digital 64 × 64 silicon photonic switch with vertical adiabatic couplers for broadband operation. Reproduced with permission [205]. Copyright 2016, The Optical Society. (h) Wafer-scale stitched 240 × 240 silicon photonic MEMS switch beyond the reticle size limit. Reproduced with permission [193]. Copyright 2019, The Optical Society. (i) CMOS-voltage-driven NOEM switch. Reproduced with permission [206]. Copyright 2019, AAAS. (j) Pixelated NOEMS switching grating for on-demand spectral filtering. Reproduced with permission [207]. Copyright 2025, AAAS. (k) Non-Hermitian hybrid III-V/Si photonic switch. Reproduced with permission [208]. Copyright 2025, Nature Portfolio. (l) Photonic crystal nanobeam cavity electro-optic switch. Reproduced with permission [209]. Copyright 2024, Nature Portfolio.

such as fast steering mirrors and large-area micromirror arrays for spatial light modulation. A representative AlScN-based MEMS mirror (Figure 7a) achieves a control bandwidth exceeding 2 kHz with high angular precision [200], while stress-actuated MEMS arrays can form reconfigurable diffraction gratings operating with THz carrier waves up to 2.28 THz [176]. A dual-axis electrostatic MEMS micromirror, with a 500 μm aperture on a 5 × 3 mm chip, scans at 4.87 kHz and 31.15 kHz along its two axes, with optical deflections ranging from 4.57° to 13.08°, offering mid-frequency modulation suitable for LiDAR and displays at low power [201]. Despite its speed advantage, electrostatic actuation often requires high voltages for substantial mechanical deflection. Achieving sufficient force and displacement at the microscale to effectively modulate optical beams typically requires driving voltages ranging from tens to over one hundred volts. Such demands increase system complexity and pose challenges to long-term reliability.

To achieve higher mechanical resonance frequencies under relatively low driving voltages, piezoelectric modulation has emerged as a key technological pathway. Its principle relies on the inverse piezoelectric effect, whereby an applied electric field is directly converted into mechanical stress to drive structural modulation. A state-of-the-art example shown in Figure 7b is an AlN piezo-optomechanical phase modulator fabricated in a CMOS-compatible process, operating at 253 MHz [147]. However, the performance benefits of piezoelectric materials often come at the cost of material compatibility and integration complexity. Challenges such as film stress, high process temperature, and potential CMOS incompatibility can complicate monolithic integration, restricting their scope in highly scalable photonic integrated circuits. Collectively, these microscale transducers illustrate a clear evolutionary trajectory toward higher speed and integration, a pursuit that continuously exposes the inherent limitations of mechanically mediated actuation. The inertia of mass, the slow dynamics of heat, and the voltage-displacement compromise create a performance ceiling fundamentally tied to the microscale domain. This recognition catalyzed the pivotal transition toward a paradigm where modulation is achieved by

the direct manipulation of the refractive index, circumventing mechanical inertia altogether.

The inherent inertia and energy inefficiency of mechanical transducers fundamentally limit their operational bandwidth. This bottleneck was decisively overcome by harnessing the EO effect, particularly the Pockels effect [210], which enables direct modulation of a material's refractive index via an electric field. The essential advantage of this paradigm shift lies in the decoupling of modulation speed from mechanical mass and resonance constraints, thereby enabling direct access to the GHz and even hundreds of GHz frequency regimes. This advance establishes a solid foundation for high-speed optical communications and precision spectroscopy. The breakthrough has been driven by the emergence of thinfilm lithium niobate (TFLN) platforms, which integrate the outstanding EO properties of lithium niobate crystals with the scalability of semiconductor micro and nanofabrication technologies.

A prominent hallmark of this performance leap is the order-of-magnitude enhancement in modulation bandwidth, rooted in the phasematching design between microwave and optical signals. In conventional devices, the parasitic capacitance of the electrodes severely limits response speed. Advanced traveling-wave electrode designs overcome this constraint by synchronizing the propagation of the modulation field with the optical wave. Through precise microwave transmission line engineering, including optimization of electrode impedance and microwave–optical velocity matching, state-of-the-art thin-film lithium niobate modulators have extended their 3dB optical bandwidth beyond 110 GHz and demonstrated support for single-wavelength data transmission rates exceeding 200 Gbps [211, 212]. This implies that the effective operating frequency range now fully spans the radiofrequency and microwave domains.

Alongside the achievement of ultra-high bandwidth, the concurrent optimization of driving efficiency reflects the energydimension design logic of EO modulation, with its essence lying in the enhancement of the spatial overlap integral between the optical and modulation fields. Driving efficiency is commonly characterized by the product of the half-wave voltage and the interaction length. By employing structures such as inverted ridge waveguides or thin-layer silicon bonding, researchers have effectively confined the optical field within the region of the applied electric field, thereby reducing the half-wave voltage-length product to approximately 1.0 V·cm. For instance, the adoption of transparent conductive oxide electrodes has enabled a modulation bandwidth of 108 GHz while maintaining a high driving efficiency of approximately 1.02 V·cm, underscoring the effectiveness of structural design in simultaneously optimizing speed and energy efficiency [212].

Nevertheless, although electro-optic direct modulation has delivered major advances in bandwidth and efficiency, it also exposes inherent limits in functional scope that point toward the next stage of evolution. Integrated EO modulators, such as thin-film lithium niobate, are largely restricted to linear, high-speed control of optical phase or intensity. While their performance is exceptional, they remain fundamentally constrained in enabling functions that rely on nonlinear or multiphysics interactions, including dynamic nonreciprocity, optical frequency-comb generation, and coherent microwave–optical state conversion. Moreover, monolithic integration of lithium niobate with on-chip sources and detectors remains challenging due to material incompatibilities. As a result, by resolving the primary challenges of speed and efficiency, electro-optic modulation has simultaneously elevated the demands for functional diversity and system-level integration, motivating a shift toward nanoscale platforms and deeper exploitation of multiphysics coupling.

As EO modulation approaches maturity at ultrahigh bandwidths, the research focus in optical modulation shifts toward a more demanding direction: maintaining high-speed response while introducing new physical degrees of freedom to expand device functionality. This demand naturally drives the technology into the nanoscale regime. At characteristic dimensions of several hundred nanometers, which is well below the optical wavelength, optical, acoustic, electrical, and mechanical strain fields can be strongly colocalized, giving rise to intense coupling and a new paradigm of multiphysics-assisted modulation. The essence of this paradigm is no longer the linear superposition of a single effect, but rather the deliberate design of nanostructures to actively shape the interactions among different physical mechanisms, thereby opening new pathways toward functionalities such as quantumstate control, frequency conversion, and nonreciprocal transmission.

This paradigm is first manifested in the extreme reinforcement of classical physical effects, with its design principle relying on nanoscale mode compression to overcome the inherent trade-off between efficiency and frequency in macroscopic devices. In the domain of AO modulation, conventional bulkmaterial devices struggle to simultaneously achieve high frequency and strong coupling. An innovative design addresses this challenge by coconfining optical and acoustic modes within a suspended aluminum nitride film only 330 nm thick, thereby enabling strong interaction at high frequencies [213]. Such a localized design leads to an order-of-magnitude enhancement in AO interaction strength, enabling efficient excitation of Lamb waves for optical modulation across the high-frequency range of 1.35 to 19.2 GHz. The conversion efficiency significantly surpasses that of conventional bulk devices based on surface acoustic waves. An alternative approach employs AlN thin films to excite surface acoustic waves at 12.1 GHz, which are then sideband-resolved and coupled to a high-quality-factor photonic crystal nanocavity. This configuration enables electrically controlled modulation and optical gain with low power consumption [214]. This demonstrates that nanostructures, by confining both optical and acoustic fields within an extremely small volume, fundamentally redefine the boundary of interaction strength, thereby making efficient modulation feasible at tens of GHz frequencies and overcoming the physical limitations of traditional AO devices.

Furthermore, the nanoscale regime creates favorable conditions for exploiting intrinsic nonlinear effects and pursuing novel hybrid integration pathways, thereby opening new frontiers of ultrabroad bandwidth and high efficiency within classical systems. For instance, lithium niobate nanowire modulators based on $\chi^{(2)}$ nonlinearity have demonstrated lossless amplification of squeezed states across an exceptionally wide bandwidth exceeding 25.1 THz, with a modulation depth of 4.9 dB and an energy consumption below 1 pJ per bit [215]. In the domain

of hybrid integration, siliconon lithium niobate Rayleigh surface acoustic wave modulators, enabled by heterogeneous bonding, have achieved an outstanding halfwave voltage–length product of 0.496 V·cm across frequency ranges from hundreds of MHz to the GHz regime [15]. These advances highlight that the nanoscale not only strengthens individual physical effects but also provides a versatile platform for the efficient hybrid integration of disparate material systems and physical mechanisms, thus enabling simultaneous optimization of bandwidth, efficiency, and power consumption.

Beyond performance enhancement, the central advantage of nanoscale multiphysics integration lies in its capacity to create entirely new dimensions of optical functionality, such as dynamic reconfigurability and multidimensional signal processing. This capability arises from the simultaneous programming of optical, electrical, and mechanical degrees of freedom. For instance, reconfigurable nanoscale devices, such as a conductive polymer nanograting tunable from kHz to MHz rates [216], highlight the potential for flexible photonic systems. Another two-dimensional photonic crystal cavity array, exploiting carrierdispersion effects, enables optical programming on subnanosecond timescales and at GHz rates, thereby achieving spatiotemporal joint modulation [217]. Another type of electrostatically reconfigurable nanogap device (Figure 7c) achieves substantial spectral tuning in the midinfrared range of 14–18 μm by dynamically varying the gap between metallic plates from 1 nm to 60 nm, thereby exploiting localized surface plasmon resonances [202]. Such devices exemplify the reconfigurability afforded by the nanoscale: their optical response is no longer static but can be dynamically reprogrammed in real time through electrical signals. This capability paves the way for advances in adaptive optics and intelligent sensing.

The aforementioned enhancement and functional expansion of classical systems ultimately provide an indispensable interface for precision control in quantum information science, with the central objective of directly manipulating the quantum states of photons. A key example is the pixelated nanooptomechanical grating employed for quantum light sources (Figure 7d) [63]. This device utilizes voltage-tunable nanobeam photonic crystal cavities, with mechanical frequencies of 10 MHz and 52 MHz, to filter single photons emitted from quantum dots. It achieves an exceptionally high tuning rate of 97 GHz per nanometer together with a narrow linewidth of 0.54 nm. The breakthrough of this work lies in the deep integration of nanomechanical tunability with the filtering properties of optical resonances, thereby enabling precise and dynamic control of photons as carriers of quantum states.

The ultimate form of a quantum transducer is the realization of coherent conversion between quantum states at entirely different frequencies. This requirement calls for strong, low-noise coupling among optical, electrical, and acoustic fields at the nanoscale. At the state of the art, integrated quantum transducers have demonstrated monolithic integration of superconducting qubits operating in the microwave regime around 5 GHz, piezoelectric acoustic resonators, and optical microcavities in the near-infrared band around 200 THz, as illustrated in Figure 7e. Such platforms provide a critical foundation for coherent quantum-state transduction and manipulation across widely separated frequency domains [218]. The operating principle is as follows: the state of the qubit is first converted into mechanical vibrations of nanoscale structures via the piezoelectric effect, and subsequently transferred to optical photons through the photoelastic effect. Under millikelvin cryogenic conditions, such systems have achieved single-phonon excitation efficiencies as high as 75%, with added noise suppressed to as low as 0.57 equivalent photons, thereby demonstrating outstanding quantum transduction performance. Similarly, integrated qubit–cavity systems have demonstrated single-phonon-to-single-photon conversion, as illustrated in Figure 7f, establishing a physical mechanism for quantum state transfer [203]. Additionally, a nanophotonic piezo-optomechanical transducer achieves 4% conversion efficiency from 4.07 GHz qubit states to optical telecom signals using only 31 μW [204]. This series of cases signifies the progressive maturation of the nanoscale multiphysics modulation paradigm. The trajectory has moved beyond the reinforcement of classical effects toward the establishment of a bidirectional and coherent quantum bridge between the microwave and optical domains, which constitute two central branches of quantum information processing. The key performance metrics, namely conversion efficiency and added noise, are determined directly by the strength of multiphysics coupling at the nanoscale and by the mechanisms governing quantum decoherence.

The data summarized in Table 2 quantitatively reveal a clear three-stage evolution of optical modulation technologies, governed by the dominant physical mechanism. Devices relying on mechanical inertia, such as thermo-optic and electrostatic modulators, are fundamentally confined to the hertz to kHz regime, whereas modulators based on intrinsic electro-optic effects bypass mechanical mass and extend operation into the GHz and even hundreds-of-GHz range. This comparison confirms that replacing mechanical displacement with direct refractive-index control is the decisive step for overcoming frequency bottlenecks. More critically, nanoscale integration introduces a further qualitative shift. This progression defines the central message of this chapter: the attainable modulation bandwidth and functionality are fundamentally set by the physical degree of freedom being controlled, evolving from mechanically limited systems to electro-optic materials and ultimately to nanoscale platforms where tightly coupled optical, electrical, and mechanical fields enable capabilities unattainable at larger scales.

7.2 | Transducers for Advanced Optical Switch

In the transduction process between optical signals and mechanical deformation, MEMS serve as a pivotal mediating platform that enables direct reconfiguration of optical paths, such as waveguide structures, offering distinct advantages in photonic switching and modulation.

The design philosophy of optical switches is founded on the need for precise mechanical control of light paths. At its core, the approach employs microelectromechanical actuators to generate micrometerscale displacements, thereby directly altering the relative position or coupling state between waveguides to achieve physical routing of optical signals. The primary advantage of this scheme lies in the mechanically separated light paths, which inherently enable extremely low optical insertion loss and

TABLE 2 | Characteristics of optical modulation transducers.

Transducer		Modulation frequency	Device CD	Refs.
Mechanism	**Device**			
AO	Microwave-Optical Transducers	~3.5 GHz	Micrometer-scale	[5]
AO	Piezo-Optomechanical Quantum Transducer	~5 GHz	Micrometer-scale	[219]
AO	SAW–Photonic Modulator	0.9–10.6 GHz	Micrometer-scale	[220]
AO	AlN-SOI AO Modulator	2.25 GHz	Micrometer-scale	[221]
AO	Brillouin Photonic Modulator	4 GHz	Micrometer-scale	[222]
AO	Piezo-optomechanical quantum transducer	5.1–5.7 GHz	Micrometer-scale	[218]
AO	Optomechanical Crystal Nanobeam	200 MHz – 2.25 GHz	Nanoscale	[223]
AO	silicon photonic wires	~10 GHz	Nanoscale	[224]
AO	SAW–Photonic crystal Modulator	1.35–19.20 GHz	Nanoscale	[213]
AO	SAW–multiple photonic nanocavities	12.1 GHz	Nanoscale	[214]
Capacitive	MEMS tunable nanograting	250 kHz	Millimeter-scale	[225]
Carrier Dynamic	Quantum tunneling excitonic modulator	8 MHz	Nanophotonic	[226]
Electrochemical	Electrochemically switchable metagrating	30 Hz	Nanoscale	[216]
Electrostatic	Grating Phase Shifters	~50 kHz	Microscale	[227]
Electrostatic	Pixelated NOEM Grating	12 MHz	Nanoscale	[207]
EO	Microcavity EO Modulator	>110 GHz	Micrometer-scale	[211]
EO	Random Multimode Waveguide Grating	100 kHz	Micrometer-scale	[62]
EO	Mach–Zehnder EO Modulator	108 GHz	Micrometer-scale	[212]
EO	Optoelectronic Oscillator	30 GHz	Micrometer-scale	[228]
EO	Plasmonic Monolithic Directional Coupler Switch	9 GHz	Micrometer-scale	[60]
EO	Chiral EO Modulator Based on Asymmetric Mie Scatterers	~1 GHz	Nanoscale	[229]
EO	PhC-spatial light modulators	140 GHz	Nanoscale	[217]
EO & Thermal	Hybrid Photonic-Electronic Near-Sensor Edge Computing Chip	MHz	Micrometer-scale	[33]
optical force	Mach–Zehnder waveguide	5.773 MHz	Nanophotonic	[194]
Optomechanical	tapered nanofiber	N.A.	Nanophotonic	[230]
Piezoelectric	Piezo-optomechanical Cantilever Modulator	23.3 MHz	Micrometer-scale	[231]
Thermal	Tip-Tilt-Piston Electrothermal Micromirror Array	Hz	Millimeter-scale	[232]
Thermal	Dual-axis MEMS mirror	1 kHz	Micrometer-scale	[233]
Thermal	Grating Phased Array	100 kHz	Micrometer-scale	[234]
Thermal	Waveguide phased array	14.3 kHz	Micrometer-scale	[235]
Thermal	Microdisk Phased Array	330 kHz	Micrometer-scale	[236]
Thermal	microdisk resonator filter	THz	Micrometer-scale	[237]

exceptionally high extinction ratios, as they circumvent the additional losses associated with phase-change-based mechanisms.

In 2024, a MEMS-based lateral waveguide coupling transducer is proposed, exemplified by the split-waveguide crossing (SWX) design in Figure 7g, which dynamically tunes light propagation by electrostatically driving adjacent waveguide halves to move laterally [238]. This switch relies on a lateral transducer, which employs opposing electrostatic forces to mechanically separate or combine the waveguides, achieving broadband operation (1400–1700 nm) with ultra-low excess loss (0.1–0.47 dB) and an ultracompact footprint of $23 \times 23\ \mu m^2$ per cell, demonstrating high potential for dense photonic integration. However, the lateral mechanical actuation mechanism suffers from millimeter-scale actuators that restrict scalability and require large inertial masses to generate micrometer-scale displacements, creating an inherent trade-off between limited microsecond-range switching speed and precision.

To overcome these limitations, vertical transducer designs were introduced for optical switching. For example, the suspended silicon waveguide directional coupler posed by Zhou's group, shown in Figure 7h, employs electrodes to drive vertical movement of the waveguide, thereby modulating coupling efficiency [239]. This configuration achieves 14.25 dB attenuation at 90 V bias within the mid-infrared wavelength range of 6.4–7 μm. Unlike lateral actuation, vertical movement confines displacement along a single axis, which not only helps reduce crosstalk but also simplifies the force transmission path. Nevertheless, vertical transducers inherit core limitations of macroscopic mechanical motion. High actuation voltages of 90 V are required to overcome the larger force needed for vertical displacement, resulting in slower response times of 177 μs, unsuitable for high-speed applications.

Building on this trend, Wu's group introduced large-scale MEMS-based photonic switch arrays that pushed the scalability frontier. In 2015, they reported a 50×50 optical circuit switch, integrating 50×50 MEMS-actuated movable directional coupler transducers on a $9 \times 9\ mm^2$ chip [240]. Each switching element relied on mechanically adjustable directional couplers, achieving a 2.5 μs response time at just 14 V and an extinction ratio of 26 dB. This work demonstrated that MEMS motion, though slower than carrier-based modulation, could scale to unprecedented port counts with relatively low optical loss (0.04 dB per crossing), offering a strictly nonblocking architecture. In 2016, as shown in Figure 7g, the same group advanced to vertical actuation by introducing MEMS-driven vertical adiabatic coupler switches in a 64×64 array [205]. This design provided broadband operation across 1400–1700 nm, digital ON/OFF switching without bias drift, and ultra-low insertion loss of 3.7 dB (0.058 dB/port). The vertical actuation minimized cumulative loss and achieved sub-microsecond switching (0.91 μs), three orders faster than earlier vertical tuning MEMS, while ensuring reliability over 10^{10} cycles. Further scaling by this group was realized in 2019 in Figure 7h, when wafer-scale stitching enabled a record 240×240 optical switch fabricated across a $4 \times 4\ cm^2$ chip [193]. Each 80×80 block was lithographically stitched with negligible loss (0.004 dB per boundary), yielding a large integrated switch, with ON/OFF ratios of 70 dB, insertion loss of 9.8 dB, and switching speeds below 400 ns. These milestones highlighted how MEMS transducers could evolve from chip-scale to wafer-scale switching architectures, overcoming reticle size limits.

Nevertheless, the performance of this paradigm is severely constrained by the inertia of moving masses, which imposes a fundamental limitation on response speed. To generate sufficient optical phase shifts, optical switch transducers typically require micrometerscale mechanical displacements. Such displacements demand driving voltages ranging from tens to hundreds of volts in order to overcome mechanical resistance. This dependence creates a critical tradeoff between speed and energy consumption, representing a major bottleneck for further performance enhancement.

Both lateral and vertical mechanical transducers are constrained by their reliance on large inertial masses and displacement-dependent trade-offs. However, reducing both the displacement magnitude and the overall structural scale offers a pathway to improved performance. This insight motivates the exploration of nanoscale actuation that enables faster response times, smaller footprints, and enhanced reliability for photonic switching applications. Building on this motivation, as shown in Figure 7i, Leuthold's team demonstrated a hybrid photonic–plasmonic opto-electro-mechanical transducer, where a 35-nm air gap and a sub-100-nm gold membrane form the core of the device [206]. Electrostatic actuation of the membrane introduced only a 4-nm displacement—two orders of magnitude smaller than in traditional MEMS—yet was sufficient to induce a full optical resonance shift due to strong plasmonic confinement. This transduction scheme enabled 60-ns switching at CMOS-compatible 1.4 V, with minimal optical loss (0.1 dB) and an ultracompact footprint of $10\ \mu m^2$. The effective nanoscale transducer mitigated inertial delays and squeeze-film damping, raising the resonance frequency to 23 MHz and establishing a new paradigm: plasmonic field enhancement serving as the intermediary in the optical–electrostatic energy conversion. Compared to earlier lateral and vertical MEMS transducers, this design effectively minimized mechanical motion, relying instead on plasmonically enhanced conversion for fast, low-power switching.

Yet, even plasmonic transducers face challenges in scalability and multiplexed control. To address this, in 2025, researchers advanced to pixelated NOEM gratings, as illustrated in Figure 7j. Here, each of the 80 pixels functioned as a nanoscale transducer, where electromechanically induced symmetry breaking toggled the grating between subwavelength and Bragg regimes. Collective nanometer-scale gap modulations achieved wavelength-selective switching in 7 ns with >100 dB contrast, while consuming only 1.1 pJ per operation and incurring negligible dynamic optical loss of 0.03 dB [207]. This distributed transducer array enabled programmable spectral shaping and massively increased integration density. The trade-off, however, lay in the complexity of independently addressing 80 coupled transducers. Compared to single-unit plasmonic devices, the pixelated NOEM architecture illustrates how nanoscale transduction can scale toward functional photonic fabrics, combining ultrafast response, CMOS-level voltages, and spectral programmability in a compact form factor.

Despite the impressive advancements in mechanical transducers, there are inherent limits to scalability when shrinking their

size for enhanced performance. As a result, researchers are increasingly investigating alternative transduction mechanisms to push the boundaries of optical switching. Building on the principles of non-Hermitian photonics, as shown in Figure 7k, Feng's team in 2025 demonstrated a hybrid III-V/Si optoelectronic transducer where vertically coupled InGaAsP and silicon waveguides form the core switching element. Optical pumping of the InGaAsP layer introduced only 100 ps carrier dynamics—an order of magnitude faster than conventional silicon photonic switches—yet achieved complete light routing between layers through precise parity-time symmetry control [208]. This transduction mechanism enabled non-blocking switching with 15 dB extinction at the through port and 37 dB at the drop port, all within an 85 × 85 μm footprint. The exceptional point physics governing this system created a new switching paradigm: gain-loss engineering serving as the mediator in the optical-electronic energy conversion, fundamentally different from traditional refractive index modulation approaches.

While the non-Hermitian approach excels in speed and scalability, power efficiency remains challenging due to the optical pumping requirements. Addressing this limitation, Zhong's team in 2024 developed a photonic crystal nanobeam cavity optical switch in Figure 7l, where a 10 μm silicon waveguide with embedded PIN junctions achieved record-low 0.10 mW static power consumption [209]. Electrically induced carrier concentration changes of merely 10^{17} cm^{-3} were sufficient to blue-shift the resonance by 0.75 nm, enabling switching through detuning rather than phase modulation. The transducer's 0.12 μm^3 mode volume enhanced the plasma dispersion effect, yielding 6.34 fJ/bit energy efficiency while maintaining 136 Gb/s PAM-4 signal integrity—a testament to how nanoscale light confinement can overcome the classical trade-offs between speed, loss, and power in photonic switching.

Table 2 also provides quantitative confirmation of the unified transduction logic illustrated in the main figure, namely that the attainable speed of the switch is fundamentally determined by the physical degrees of freedom it engages. In paradigms centered on mechanical displacement, electrostatic and thermomechanical optical switches are inevitably constrained by inertia timescales defined by mass and elasticity, with modulation frequencies limited to the kHz–MHz range. When the transduction pathway shifts to electromagnetic and carrier degrees of freedom, information can be directly encoded into the optical field or the intrinsic response of the medium, and switching speeds rise to the GHz regime. This transition is not a matter of incremental optimization but rather the inevitable outcome of migrating from mechanical to electromagnetic degrees of freedom, corresponding to a fundamental replacement of the information carrier from slow displacements to fast electronic and photonic responses.

Equally significant, this migration of degrees of freedom does not eliminate tradeoffs but instead redefines them in new dimensions. Highspeed optical switches, while overcoming inertial limitations, introduce additional constraints such as absorption loss, fabrication tolerance, and drive integrity, thereby positioning different mechanisms within distinct performance regions of the unified transduction space defined in Figure 1. Consequently, the evolution of optical switching technologies does not converge toward an optimal mechanism, but rather progresses along a trajectory from mechanical to electromagnetic and ultimately to multiphysics cooperation, selecting and integrating across performance frontiers shaped by frequency levels and degreeoffreedom combinations. Future design priorities will focus on how, within this unified framework, systemlevel transduction programming and architectural coordination can be achieved in accordance with applicationspecific priorities for speed, energy consumption, and loss.

In summary, the evolution of optical modulation and switching technologies is fundamentally driven by the parallel, yet mutually constraining demands imposed by system-level applications such as high-speed communications, quantum information processing, and intelligent optical interconnects on bandwidth, power consumption, and functional complexity. In response to this tension, the technological paradigm has undergone a sequence of well-defined transitions. Early modulation and switching approaches based on mechanical inertia established initial performance boundaries by trading speed for large angular range and stability. Subsequent solutions relying on electro-optic and carrier-based effects markedly increased modulation speed through direct access to intrinsic material responses, but remained constrained by interaction length, drive conditions, and achievable integration density. More recently, nanoscale multiphysics cooperative mechanisms have emerged, in which the joint design of optical, acoustic, electrical, and mechanical degrees of freedom enables concurrent improvements in speed, energy efficiency, and functional diversity, albeit at the cost of substantially increased design complexity and fabrication demands.

Each class of physical mechanism thus delineates a distinct and fundamentally bounded region within the overall performance space. Looking forward, system-level heterogeneous integration represents a coherent strategy for transcending these individual limits by deliberately combining complementary performance envelopes at the chip level. Through such integration, next-generation photonic processing and interconnection systems can be constructed to simultaneously satisfy multiple stringent and often competing performance requirements.

8 | Advanced Implementation of Transducers

Across the preceding chapters, systematic analyses of wearable sensing, acoustic transduction, metamaterial-enhanced spectroscopy, tunable metasurfaces, and optical modulation and beam control converge on a clear methodological principle: transducer design is fundamentally guided by application-specific prioritization of key performance metrics, strictly bounded by the intrinsic limits of the underlying physical mechanisms, and ultimately realized through precise matching among mechanism, scale, and operating frequency. This logic manifests consistently in technological evolution. As target applications progress from human and acoustic sensing in the kHz range to THz molecular fingerprinting and further toward optical communications and wavefront control near GHz, the continual upward shift in operating frequency has systematically selected and catalyzed new physical mechanisms and nanoscale structures.

However, next-generation systems such as autonomous driving, in vivo precision medicine, and integrated quantum sensing exceed the capabilities of any single function or physical domain. These systems demand deep integration of sensing, computation, communication, and actuation under stringent constraints on footprint, power consumption, and reliability. The core challenge, therefore, shifts from optimizing individual metrics to coordinating multiple physical mechanisms at the system level and simultaneously traversing several performance boundaries. Motivated by this transition, this chapter elevates the perspective from analyzing isolated transduction principles to constructing integrated systems. It focuses on implementation pathways for advanced transducers and examines how diverse mechanisms, each with distinct strengths, can be treated as composable functional primitives. Through heterogeneous integration, co-design, and intelligent control, such primitives can be assembled into reconfigurable and scalable next-generation microsystems. This shift marks a progression from understanding and optimizing individual physical bridges to engineering networked systems that strategically connect multiple physical nodes at the system level.

8.1 | Next-Generation RF–Optic Communication Modules with Transducers

8.1.1 | Transducer for Beam Steering

Beam-steering transducers underpin angular control in RF-photonic systems [241–243], yet their attainable field of view, angular resolution, modulation bandwidth, and power efficiency are highly constrained by the actuation physics of transducers. In the design of beamdeflection systems, the specific application context defines the nonnegotiable prioritization of core performance metrics. At the same time, the intrinsic laws of different physical mechanisms fundamentally delineate both the theoretical limits and the practical boundaries of these performance capabilities.

For applications such as LiDAR, three-dimensional sensing, and macroscopic imaging, the primary requirement is to obtain high-resolution spatial information over a certain distance. This translates directly into an uncompromising priority for a wide field of view and high angular resolution, while the demand for scanning speed is comparatively modest, typically satisfied by frame rates ranging from a few Hz to several kHz. To meet this performance priority, solutions within the mechanical inertia domain naturally emerge as the preferred choice. By physically rotating macroscopic masses, such as millimeter-scale mirrors, the beam direction can be directly altered, with the deflection angle determined solely by the mechanical structure, thereby enabling wide fields of view spanning tens of degrees.

As illustrated in Figure 8a, a piezoelectric ceramic-driven silicon mirror platform achieves beam modulation through the mechanical torsion of a cantilever array, with its principal advantage lying in the large stroke that provides a high dynamic range [244]. Equally noteworthy are the biaxial electrostatic micromirrors, which achieve optical deflections of ±13.08° [225], and the MEMS grating modulators, which enable beam steering up to ±30°. Through the precise engineering of microscale mechanical structures, these devices deliver large deflection angles within compact footprints, thereby offering critical solutions for beam scanning and spatial modulation. However, the intrinsic bottleneck of this physical domain lies in the constraint imposed by rotational inertia on acceleration, which restricts the response speed to the kHz–MHz range. In addition, such devices are subject to potential mechanical wear and sensitivity to vibration. These limitations represent the tradeoff that must be accepted in exchange for achieving wide fields of view and high precision.

For other applications that demand response speeds and operational flexibility beyond what macroscopic mechanical systems can offer, yet cannot tolerate the severe compromises in angular range or system complexity associated with nanoscale wavevector-based devices, such as mid-range high-resolutio radar, medical ultrasound imaging, adaptive optics correction, and high-end laser projection, the primary performance objective is to achieve an optimal balance among speed, angular coverage, precision, and system-level integrability.

This requirement has driven the core design paradigm of microscale arrays with programmable control domains. By integrating multiple micrometer-scale transducer elements, each with a limited individual stroke, into an array and endowing them with independent phase or timing control, these systems trade spatial redundancy and increased architectural complexity for enhanced overall agility, programmability, and robustness. As illustrated in Figure 8b, the stretchable piezoelectric ultrasonic array achieves beamforming at 7.3 MHz through optimized element spacing. This configuration enables remote sensing over complex surfaces, demonstrating notable advantages in spatial adaptability and detection sensitivity [245]. In the optical domain, scandium-doped aluminum nitride MEMS micromirrors achieve submicroradian angular precision through embedded sensing [200]. In parallel, MEMS grating modulators operating at a resonance frequency of 467.7 kHz enable beam steering of ±30° with a response time of 1.1 μs [225]. A 32-element PMUT phased array operating at 1.4 MHz achieves dynamic focusing and high acoustic pressure output [250]. Additional examples include resonant acoustically driven mirrors at 0.9 kHz [251] and a 2 × 2 CMUT array supporting full-space scanning at 76 kHz [252]. These devices collectively sacrifice individual element stroke for significantly enhanced agility, programmability, and integration density. These advances highlight the distinctive advantages of MEMS devices in delivering both high precision and ultrafast optical beam control. Such devices no longer aim to push a single performance metric to its theoretical limit. Instead, through array-based architectures and intelligent control algorithms, they achieve dynamically reconfigurable, well-balanced performance across moderate bandwidths in the kHz–MHz range, practical angular coverage, and high precision. This holistic capability addresses the system-level integration demands of applications that impose stringent and simultaneous requirements on multiple performance dimensions.

When application scenarios shift toward free-space optical communications, frequency-modulated continuous-wave ranging in LiDAR, or ultrafast laser manipulation, the performance priority fundamentally pivots to ultra-high speed and bandwidth. In these regimes, beam steering is required to execute switching or continuous scanning on nanosecond to microsecond timescales, while

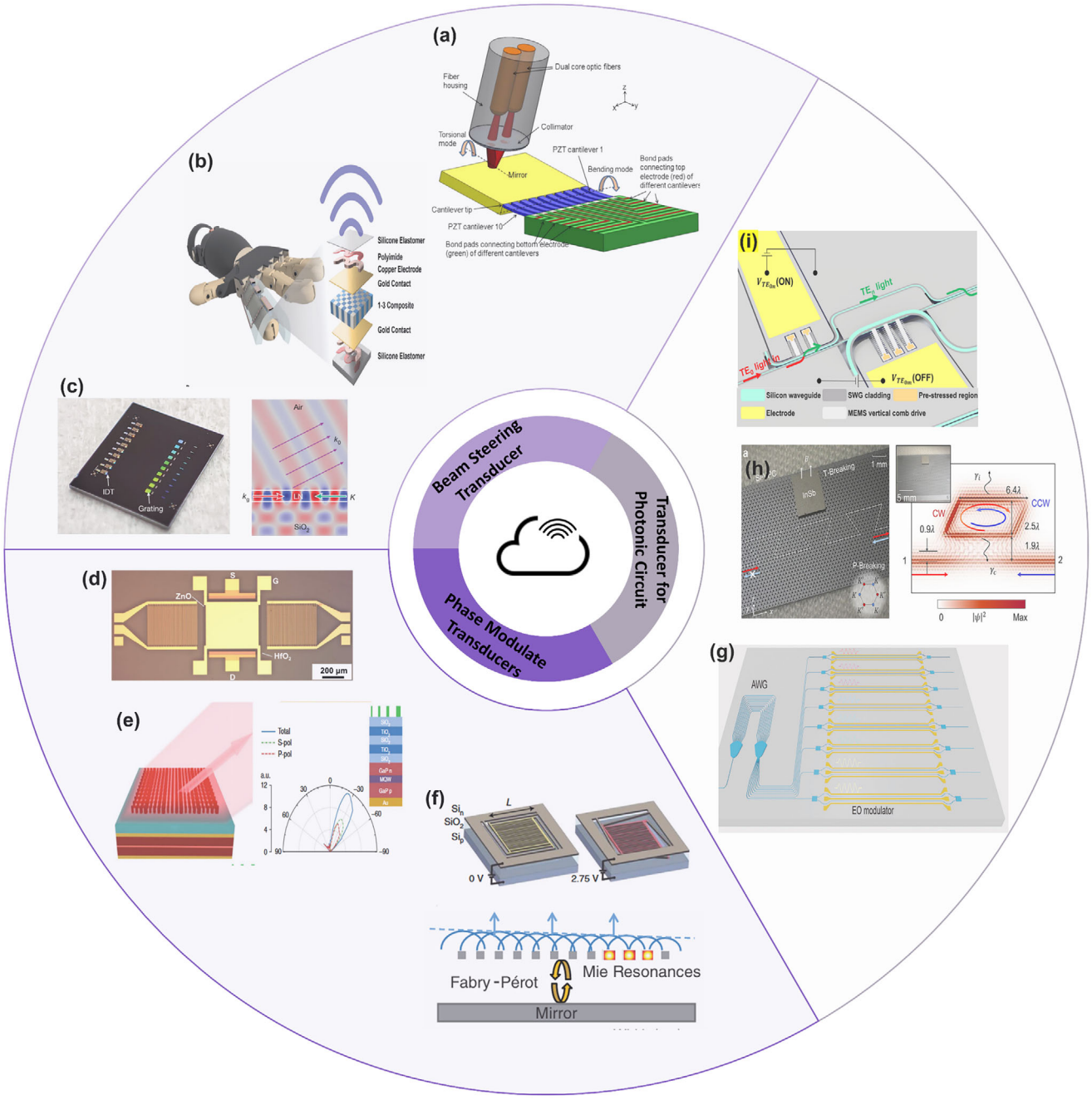

FIGURE 8 | Transducer-integrated multiscale modules for RF–optical communication functions. (a) Mesoscale piezoelectric 3D MEMS VOA with PZT cantilever arrays for translational/rotational mirror actuation, kHz operation. Reproduced with permission [244]. Copyright 2010, IEEE. (b) Microscale stretchable ultrasound array using PZT–polyimide composites for dense beamforming, MHz center frequency. Reproduced with permission [245]. Copyright 2024 The Authors. (c) Nanophotonic AO beam steering on LNOI driven by GHz SAW for frequency–angle-resolved LiDAR. Reproduced with permission [243]. Copyright 2023, The Author(s). (d) Microscale SAW phase shifter using ZnO TFT gating on $LiNbO_3$, 455 MHz operation. Reproduced with permission [246]. Copyright 2025 The Author(s). (e) Microscale dielectric metasurface and LED module using cavity enhancement and metasurface scattering at 634 nm. Reproduced with permission [247]. Copyright 2019 WILEY-VCH Verlag GmbH & Co. KGaA, Weinheim. (f) Nanoscale silicon metasurface MEMS phase modulator exploiting Mie and Fabry–Pérot resonance coupling and vertical nanowire displacement for dynamic phase control, up to 1 MHz mechanical tuning at visible wavelengths. Reproduced with permission [248]. Copyright 2019, AAAS. (g) Microscale thin-film $LiTaO_3$ Mach–Zehnder EO modulator for PICs with TE control. Reproduced with permission [59]. Copyright 2025, The Author(s). Advanced Science is published by Wiley-VCH GmbH. (h) Microscale nonreciprocal topological photonics using InSb magneto-optic elements; valley-protected edge states in the THz range. Reproduced with permission [249]. Copyright 2025 The Author(s). Advanced Materials published by Wiley-VCH GmbH. (i) Microscale MEMS programmable mode switch; electrostatic cantilevers tune sub-micron gaps for mid-IR mode routing. Reproduced with permission [197]. Copyright Wiley-VCH GmbH.

the demand for a large absolute field of view becomes secondary. Under such constraints, physical mechanisms operating in the wave-vector modulation domain exhibit decisive and essentially irreplaceable advantages.

AO deflectors achieve beam steering by exploiting refractive-index gratings induced by propagating acoustic waves, with the deflection angle exhibiting a strictly linear dependence on the acoustic frequency. As illustrated by the thin-film lithium niobate integrated acousto-optic deflector shown in Figure 8c, rapid beam scanning can be realized using a 1.8 GHz Rayleigh acoustic wave. The achievable switching speed is fundamentally limited by the acoustic transit time and can reach the microsecond or even nanosecond regime, making this approach exceptionally well-suited for high-speed frequency-to-angle mapping applications [243].

Thin-film lithium niobate AO arrays further enable microwave-driven multi-beam steering for spatial multiplexing [242]. Complementary to this approach, electro-optic beam deflection mechanisms operate by directly modulating the refractive index via an applied electric field. For example, modulators based on thin-film lithium niobate can achieve response times on the nanosecond scale [253, 254]. However, the underlying physics of wave-vector modulation intrinsically ties the achievable deflection angle to the interaction length or the acoustic wavelength. As a result, the steering range along a single axis is commonly reported within approximately 10°, representing an inherent trade-off accepted in exchange for ultra-high operational speed.

For applications such as consumer-electronics-integrated sensing that demand an ultra-wide field of view, full solid-state operation, and high reliability, like smartphone facial recognition, as well as low-power wide-area monitoring, the performance priorities clearly favor extremely extensive angular coverage, compact form factors, low power consumption, and long-term stability, while scanning speed becomes a parameter that can be substantially relaxed. Under these constraints, beam steering is most naturally implemented with chip-scale optical phased arrays, and the reduced speed requirement makes thermo-optic phase shifters an attractive choice because they offer simple, CMOS-compatible, and highly stable phase control at scale.

Optical phased arrays synthesize beams in arbitrary directions by coherently controlling the phases of an array of nanoantennas or waveguide-based emitters, without any mechanical motion. For instance, silicon nitride OPAs have demonstrated ultra-wide field-of-view scanning exceeding 160° [255]. Their fully solid-state and highly integrated nature confers exceptional reliability and strong potential for miniaturization. A Vernier-based OPA architecture enables 128-channel FMCW LiDAR control [256]. However, the underlying physical mechanisms in this domain, which typically rely on thermo-optic or carrier-induced effects for phase modulation, inherently limit the achievable response speed, with thermo-optic modulation generally confined to below the kHz regime. These approaches are also accompanied by intrinsic challenges such as thermal dissipation and sidelobe noise, representing fundamental constraints accepted in exchange for an ultra-wide field of view and extreme levels of integration.

Current breakthrough research efforts are challenging conventional physical boundaries through two complementary strategies. The first is domain-internal enhancement, in which the intrinsic strengths of a single physical mechanism are pushed toward their limits through innovations in materials and device architecture. For example, optical phased arrays employing traveling-wave electrodes based on thin-film lithium niobate have expanded the steering range to 50° × 8.6° while preserving high-bandwidth potential [257]. Similarly, MEMS technologies leverage array-based architectures to combine large angular excursions on the order of ±30° with microsecond-scale response times [227]. The second strategy is cross-domain integration, which seeks to combine the core advantages of distinct physical domains at the chip or system level to realize a performance envelope unattainable by any single mechanism alone. For instance, integrating the wide angular range of MEMS micromirrors with the high-speed electro-optic modulation units of thin-film lithium niobate offers a promising route toward achieving both large-area beam steering and nanosecond-scale wavelength switching on a single chip. Optical true time-delay networks developed for radio-frequency beamforming [258] provide another representative example, in which the high-speed processing capabilities of the photonic domain are harnessed to enable performance breakthroughs in the RF domain.

Within the unified framework of transduction and beam control illustrated in the main figure, the evolution of beam-shaping technologies can be understood as a rational selection and reconfiguration of distinct physical degrees of freedom within a performance space defined by speed, field of view, angular resolution, and system-level integrability. Macroscopic mechanical scanning, microscale optical arrays, nanoscale wave-vector engineering, and thermo-optic-based optical phased arrays respectively invoke different transduction pathways, including mechanical motion, optical interference, near-field phase reconstruction, and thermally induced refractive-index modulation, and serve as the core beam-shaping transducers across different frequency regimes and length scales.

8.1.2 | Transducer for Phase Modulation

Phase modulation is central to programmable control of optical wavefronts. Within the unified framework depicted in Figure 1, the essence of a phase-modulation transducer lies in selecting and activating the appropriate physical degrees of freedom to perform the core task of phase writing.

Acoustic, thermo-optic, electro-optic, and nanoscale multi-physics coupling mechanisms, respectively, exploit mechanical, thermal, electronic, or electromagnetic degrees of freedom, leading to well-defined differentiation in attainable operating frequency, modulation efficiency, and system-level integrability. This diversification of mechanisms does not represent a fragmentation of technological routes, but rather a natural projection of the performance space imposed by physical laws onto distinct application scenarios, and it provides the conceptual starting point for subsequent comparison and integration of phase-modulation technologies.

For phase-sensitive systems such as high-precision ultrasound imaging, biosensing, and stable spectral analysis, achieving a high signal-to-noise ratio, low drift, and repeatable phase control is essential. These requirements place a premium on modulators that offer excellent phase stability, reproducible modulation depth, and low power consumption, while the demand for modulation speed is typically confined to the MHz regime.

To meet this set of priorities, acoustic modulation mechanisms have been extensively investigated. In this approach, acoustic waves are excited via the piezoelectric effect and periodically modulate the optical phase through acousto-optic interactions. As shown in Figure 8d, an integrated device combining a zinc oxide thin-film transducer with a lithium niobate substrate enables electrically controlled phase tuning by modulating the phase velocity of a 455 MHz leaky longitudinal surface acoustic wave, delivering reliable and efficient control within a sub-millimeter footprint [246]. Similarly, capacitive ultrasound arrays operating at 5 MHz employ precise phase encoding to suppress harmonics and sharpen imaging resolution [259]. The strengths of these devices stem from the inherent periodicity and uniformity of acoustic-wave modulation. However, their modulation bandwidth, typically below 10 MHz, is ultimately constrained by the acoustic propagation velocity in solids and the inertia-related relaxation time set by the transducer dimensions. This limitation defines a fundamental speed boundary for this physical domain when prioritizing high precision and low power consumption.

When application scenarios shift toward high-speed optical fiber communications, microwave photonics, and coherent optical signal processing, the performance priorities pivot sharply to ultra-high modulation rates in the GHz-to-THz range, large bandwidth, and minimal energy consumption per bit, while the requirement for large absolute phase modulation from an individual device becomes comparatively relaxed. Under these demands, the linear electro-optic effect assumes a dominant role due to its unparalleled speed advantage.

In this mechanism, an externally applied electric field directly alters the refractive index of the material, with response times that are theoretically capable of reaching the femtosecond scale. Electro-optic modulators based on heterogeneous integration of aluminum nitride thin films on silicon platforms can operate stably under radio-frequency drives of 1–5 GHz, delivering nanosecond-scale responses and modulation efficiencies exceeding 10 dB per volt millimeter, thereby significantly outperforming thermo-optic alternatives in both speed and energy efficiency [260].

Nevertheless, the physical nature of electro-optic modulation also delineates its intrinsic boundaries. Accumulating a sufficient phase shift, such as a half-wave phase change, typically requires interaction lengths on the order of millimeters or relatively high drive voltages, which constrain the achievable phase scanning range within ultra-compact chips. Though heterogeneous material integration that combines LN piezoelectricity with silicon confinement via transfer printing has been reported [15], the heterogeneous integration of high-performance electro-optic materials, including lithium niobate and aluminum nitride, with mainstream silicon photonic platforms remains a central fabrication challenge.

For frontier applications such as quantum information processing, classical–quantum interfaces, and advanced optical computing, the requirements extend beyond phase modulation speed or precision alone, and instead emphasize complex functionalities including optical nonreciprocity, quantum-state-specific control, and orbital angular momentum multiplexing. Meeting these demands necessitates moving beyond the constraints of any single physical effect and entering a new regime of strongly coupled multiphysics mechanisms at the nanoscale.

In this regime, optical fields, acoustic waves, mechanical strain, and electric fields are co-confined within deeply subwavelength volumes, giving rise to cooperative and emergent effects. For example, on lithium niobate chips, the combination of phase-matched acoustic fields and quasi-traveling electric fields enables optical nonreciprocal isolation exceeding 40 dB at a modulation rate of 336 kHz, while maintaining an acousto-optic conversion efficiency of 92% [261]. In another approach, deformation-potential coupling between phonons and quantum dots allows precise phase locking and tuning of single-photon emission wavelengths over a range of 0.8 nm [262]. The realization of such functionalities relies critically on the ability of nanostructures to achieve extreme localization and enhancement of multiple physical field modes. The associated cost, however, lies in substantial system complexity, stringent requirements on nanofabrication precision, and intrinsic conflicts in the simultaneous optimization of disparate physical fields. These factors collectively define the fundamental boundary of this mechanism domain between functional richness and practical deployability.

Finally, for systems such as large-scale programmable photonic integrated circuits, on-chip LiDAR beamforming, and neuromorphic optical computing, the requirements emphasize low-voltage operation, high array density, independent pixel-level control, and compatibility with CMOS processes under moderate to low operating speeds at or below the MHz regime. These demands have driven the development of nanomechanical modulation and miniaturized electrical modulation mechanisms.

Direct reconstruction of optical wavefronts at the subwavelength scale represents another fundamental route toward meeting the demands of on-chip dynamic beam control. This approach requires moving beyond conventional phase-accumulation paradigms and toward the simultaneous design of local amplitude, phase, and polarization of the optical field. As shown in Figure 8e, a metal–Bragg hybrid cavity integrated on a gallium phosphide light-emitting diode, combined with a silicon-based dielectric metasurface, can directly reconstruct the phase wavefront of the emitted light at a wavelength of 620 nm, enabling beam collimation and shaping [247]. The physical essence of this metasurface–source co-integrated design lies in encoding the local optical states through arrays of subwavelength structures, thereby completing wavefront shaping directly at the emission aperture. This eliminates the need for discrete phase modulators and subsequent free-space or guided-wave optical systems. The primary advantages of this approach are its exceptional integration potential and prospects for dynamic tunability.

More than wavefront reconstruction at the subwavelength scale, achieving multifunctional integration at the unit-cell level

constitutes another viable pathway toward on-chip dynamic beam control. As illustrated in Figure 8f, suspended silicon nanowire arrays employ electrostatic actuation to induce nanometer-scale displacements, enabling continuous wavefront steering from 2° to 12° over a frequency range of 400 kHz to 1 MHz while maintaining relatively low drive voltages [248]. In another approach, a MOS-capacitor-based nano-optic modulator achieves independent phase and amplitude control within a compact 250 × 250 μm unit by using dual-gate modulation of the reflectivity, operating at 5.4 MHz [263]. The limitations of nanomechanical mechanisms arise from resonance frequencies that cap their maximum achievable speed, whereas miniaturized electrical modulation schemes typically cannot match state-of-the-art EO devices in energy efficiency, particularly in terms of energy per π phase shift. This contrast highlights the fundamental trade-offs among speed, energy efficiency, and functional completeness when prioritizing high integration density and programmability.

8.1.3 | Transducer for Photonic Integrated Circuit

The evolution of transducer technologies in photonic integrated circuits has progressively shifted from a linear trajectory focused on optimizing a single performance metric toward a paradigm of multi-mechanism co-design and integration driven by specific system-level requirements. This transition is fundamentally motivated by the fact that diverse application scenarios, including large-scale programmable computing, high-speed communication interconnects, quantum information processing, and low-power optical routing, place markedly different emphases on parameters such as speed, energy efficiency, integration density, functional complexity, and static power consumption. These metrics are often intrinsically constrained by physical laws and therefore cannot be simultaneously pushed to their respective extremes. As a result, transducer selection is no longer governed by absolute optimality in any single dimension, but by the performance boundaries that a given physical mechanism can offer along the dimensions most critical to a target application. Understanding the strengths and limitations of different transduction mechanisms is, in essence, an exercise in understanding how underlying physical processes delineate distinct performance envelopes, thereby enabling informed trade-offs and effective combinations.

For photonic neuromorphic computing, large-scale optical phased arrays, and integrated sensing systems, the central requirements lie in achieving high channel density, large-array programmability, and complex functional reconfigurability, while the speed requirement for individual transducer elements is comparatively relaxed, with response times in the microsecond-to-millisecond range being acceptable. This performance priority positions TO and multi-effect cooperative mechanisms as the dominant solutions. TO control modulates has a physical nature that ensures seamless compatibility with standard CMOS fabrication processes, enabling the integration of hundreds of independently addressable phase-control units on chips spanning only a few square millimeters. For example, thermo-optically tunable silicon-on-insulator microring resonators fabricated in a 45 nm process have been used for label-free virus particle detection [264]. In another demonstration, a 5 × 5 mm^2 tensor-core photonic processor integrating 87 thermo-optic phase units performs parallel analog matrix operations across hundreds of wavelength channels for radio-frequency signal classification [196]. The performance boundary of this mechanism is strictly set by the thermal diffusion time constant. This constraint represents a fundamental trade-off accepted in exchange for ultra-high integration density, fine-grained controllability, and near-zero static power consumption.

When application scenarios shift toward chip-to-chip or board-level high-speed optical interconnects, coherent communications, and microwave photonic processing, the core performance requirements pivot to supporting modulation bandwidths from tens to hundreds of GHz, extremely low energy consumption per bit, and high signal integrity. These demands inevitably drive system-level choices toward electro-optic and carrier-dispersion-based mechanisms.

The linear electro-optic effect enables direct and essentially instantaneous modulation of the refractive index by an applied electric field, endowing it with an unmatched advantage in modulation speed. TFLN Mach–Zehnder modulators, enabled by optimized coplanar waveguide electrode designs, have demonstrated bandwidths exceeding 100 GHz while reducing the energy per bit to below 14 fJ [32]. Nevertheless, achieving a sufficient phase shift requires a trade-off between drive voltage and interaction length, so there is an extra space cost for large-scale realization. Despite this trade-off, the speed advantage of electro-optic modulation remains irreplaceable. For example, tantalate-based platforms shown in Figure 8g can sustain bandwidths of 67 GHz while supporting dense wavelength-division multiplexed transmission at data rates up to 1.6 Tb/s [59].

In quantum information processing and other frontier applications that seek to transcend the diffraction limit or conventional symmetry constraints, the primary objective is no longer the incremental improvement of traditional performance metrics, but the realization of fundamentally new functionalities that are inaccessible to classical optical components. Representative examples include nonreciprocal transmission, topologically protected propagation, and chiral-selective responses. These demands have driven the development of mechanisms rooted in topological photonics and non-Hermitian physics. Unlike conventional approaches that rely on local refractive-index modulation, these mechanisms operate by systematically engineering the band structure and modal symmetries of photonic crystals or metamaterials, thereby reshaping the rules governing light propagation at a higher, system-wide level. This enables intrinsic control over propagation directionality and mode selectivity.

A representative example is provided by topological photonic chips based on indium antimonide material systems, where valley-polarized edge states under an applied magnetic field enable unidirectional THz-wave transmission, as shown in Figure 8h [249]. Similarly, a microwaveband paritytimesymmetric acoustic cavity attains 10.9 dB isolation at a 200 MHz center with a 28 kHz linewidth by balancing gain and loss with Bragg-defined boundaries [265]. The key advantage of such devices lies in the intrinsic robustness conferred by topological invariants or parity–time symmetry, rendering them insensitive to backscattering and structural imperfections. This functional leap,

however, comes at a substantial cost, including extremely narrow operational bandwidths, strong dependence on nanofabrication precision, and significant challenges in material and process compatibility with mainstream photonic integration platforms. Collectively, these characteristics confine such approaches to being explored in on-chip photonic systems.

Finally, for applications such as energy-efficient routing in optical switching networks, precision wavelength locking of lasers, and low-power tunable filters, the performance priorities clearly favor near-zero static power consumption, extremely high tuning accuracy, and long-term stability, while switching speeds in the MHz to GHz range are sufficient. To meet these requirements, nanomechanical and acousto-mechanical coupling mechanisms offer distinct advantages. Mechanical cantilevers or acoustic resonators consume energy only during state transitions, and their underlying physical principles enable static power dissipation to be reduced to the femtowatt level [266]. In Figure 8i, other demonstrations include a microelectromechanical mode converter that uses nanowatt-driven cantilevers to dynamically excite higher-order optical modes [197], and aluminum nitride on silicon controlling ring-to-waveguide coupling through 3.48 GHz acoustic standing waves [5]. A gallium phosphide–zinc oxide hybrid resonator highlights the potential for low-power optomechanical systems, demonstrating 2.1% Brillouin conversion efficiency at 2.56 GHz [267]. Although modulation rates are lower than electrooptic platforms, these devices excel in power-sensitive routing, mechanically stable tuning, and spatially localized reconfiguration.

Taken together, the developments reviewed above show that next-generation RF–optic communication modules are no longer defined by a single dominant device or mechanism, but by how transducers orchestrate multiple physical degrees of freedom within a unified system framework, as illustrated in Figure 1. Across beam steering, phase modulation, and photonic integrated circuits, transducers act as the decisive interface that maps RF, acoustic, thermal, mechanical, and electronic signals onto optical carriers, with their achievable speed, bandwidth, power efficiency, and functionality fundamentally bounded by the underlying physics they invoke. Mechanical and thermo-optic transducers excel where stability, extensive angular coverage, and dense programmability are paramount; electro-optic and carrier-based mechanisms dominate regimes demanding ultrahigh bandwidth and low energy per bit; while nanoscale multiphysics and topological platforms unlock qualitatively new capabilities such as nonreciprocity, quantum-state manipulation, and symmetry-protected transport. The central message emerging from the unified framework is that no single transduction pathway can satisfy all system-level requirements simultaneously. Instead, future RF–optic communication modules will be built through intentional hetero-integration of complementary transducers, combining distinct material platforms, length scales, and physical effects to navigate the multidimensional trade space of speed, field of view, precision, power, and integration density. In this sense, transducers are no longer passive enablers but active system architects, defining how information flows across frequency domains and ultimately determining the performance ceiling of scalable, intelligent RF–photonic systems.

8.2 | Intelligent Systems With Embedded Transduction

When our research perspective extends from isolated RF–optical communication modules with transducers to next-generation intelligent systems that integrate sensing, computation, and actuation, such as autonomous robots, adaptive prosthetics, and real-time diagnostic platforms, the system-level challenges undergo a fundamental increase in dimensionality. These systems must simultaneously support multimodal information acquisition, low-latency decision-making, and continuous adaptive interaction under stringent constraints on volume and power consumption, a level of complexity that far exceeds what any single functional module can accommodate.

In this context, the design paradigm inevitably shifts from optimizing an individual transduction mechanism to system-level construction based on multiphysics coordination. Mechanical, acoustic, optical, and electrical transduction are no longer treated as isolated devices, but as composable and schedulable physical primitives that jointly perform the fundamental tasks of information acquisition, conversion, and processing. Building on this perspective, this section explores how cross-domain integration and co-design can embed transduction itself as an efficient, scalable sensing and computing substrate within intelligent systems, thereby enabling complex intelligent behaviors in real-world environments.

8.2.1 | Mechanical Computing With Transducers

As the focus shifts from standalone RF–optical transducer modules to intelligent systems that tightly integrate sensing, computation, and actuation, the central challenge moves beyond signal conversion toward where and how computation is performed. For autonomous robots, adaptive prosthetics, and real-time diagnostic platforms, stringent constraints on latency, power, and form factor make it increasingly inefficient to rely solely on centralized digital processing. Within the unified framework illustrated in the main figure, this motivates a paradigm in which transducers are elevated from passive interfaces to active physical computing elements.

In this context, mechanical, acoustic, optical, and electrical transducers are no longer treated as isolated components, but as programmable physical substrates whose intrinsic dynamics can directly encode, transform, and process information. By exploiting properties such as resonance, nonlinearity, delay, and hysteresis, mechanical transducers in particular can perform computation at the point of sensing with minimal energy overhead. Building on this system-level perspective, mechanical computing transducers represent a paradigm shift by harnessing intrinsic structural dynamics to perform physical information processing through heterogeneous integration and co-design. Transduction principles that have been validated in distinct physical domains can be transformed into composable and reconfigurable system-level embedded computing capabilities, circumventing traditional von Neumann architecture limitations. Across these regimes, mechanical computing retains negligible leakage, steep effective subthreshold behavior, and

high-temperature tolerance, which justifies its role as a complement to transistor logic rather than a replacement [268].

One approach of this paradigm exploits the nonlinear resonant dynamics of micromechanical structures, directly mapping bistable or chaotic temporal responses onto logic operations and short-term memory. The computational speed of such devices is fundamentally set by their mechanical resonance frequency, typically in the kHz regime, while their near-zero static power consumption arises from the passive energy dissipation characteristics of mechanical structures. For example, a differential four-terminal comb-drive device, engineered with electrostatically induced nonlinear stiffness, has demonstrated a nonvolatile NOT logic gate at a resonance frequency of 14.5 kHz. The logic states are encoded by a displacement amplitude of 3.4 μm and are achieved under an AC drive voltage of 24 V [269]. Another study exploits the chaotic dynamics excited near the 9.74 kHz resonance of a silicon microresonator beam with dimensions of 330 × 3 μm. The vibration decay time constant of approximately 10 ms provides a form of physical short-term memory, enabling direct classification of motion patterns [270]. These examples demonstrate that, by precisely engineering mechanical nonlinearity through electrostatic or piezoelectric coupling, the intrinsic transient dynamics of the transducer itself can be harnessed directly as a computational resource. The complexity and speed of such mechanical computing tasks are fundamentally limited by the mechanical resonance frequency and material damping, while the robustness of logic operations is governed by the size of the nonlinear bistable regime and the noise floor of displacement readout.

When the primary computational task involves processing time-series signals, such as prediction or classification, exploiting the propagation delay of SAW to form physical delay lines offers a highly energy-efficient embedded computing strategy. The delay time is physically defined by the acoustic velocity and propagation path length, providing sub-microsecond precision and excellent stability. In a representative implementation, a 30 × 10 mm lithium tantalate chip excites a 150 MHz surface acoustic wave that traverses a 40 mm delay line, yielding a well-defined delay of 12 μs. By spatially encoding the input through patterned interdigital transducers, the system directly maps 16-bit temporal signals into neuron-like responses required for reservoir computing [271]. The core design logic of acoustic delay-line computing is defined by three coupled constraints. The processing bandwidth, on the order of MHz, is set by the radio-frequency excitation frequency. The computational capacity, expressed as the number of virtual nodes, is limited by the product of the delay time and the sampling rate. Its energy-efficiency advantage arises from the inherently parallel and passive nature of analog signal processing during wave propagation.

Further, by integrating multiple mechanical resonators on a single chip and introducing controllable coupling, higher-dimensional physical reservoirs can be constructed within a single physical domain to process more complex dynamical features. As shown in Figure 9a, a triple-coupled resonator array based on silicon-on-insulator technology exploits electrostatic interactions across micrometer-scale gaps to map kHz mechanical vibrations into a high-dimensional computational space [272]. In this system, doubly clamped beams are biased at 4 V to induce higher-order spring nonlinearity, and the combined effect of a ~13 ms decay time and information retention within the coupling network increases the parity-check memory capacity by 19% compared to a single-resonator implementation. The performance gains of such architectures rely on engineered nonlinear coupling rather than simple device replication. Computational capacity is governed by coupling strength and resonance uniformity, while the trade-offs arise from increased system complexity and stricter fabrication tolerances.

When confronted with nonstationary, broadband sensing signals such as speech or complex vibration spectra, and when high classification accuracy is required, purely mechanical-domain processing increasingly reveals limitations in response speed and decision flexibility. This has motivated the introduction of the electrical domain to form cross-physical hybrid computing systems. The core strategy is a clear division of labor: mechanical dynamics in the kHz to MHz range perform ultra-low-power analog feature extraction, while electrical circuits operating from MHz to GHz handle high-speed sampling, digitization, and complex decision-making. The device shown in Figure 9b, a 400 × 6 × 50 μm resonator, converts acceleration signals directly into stiffness perturbations, achieving mechanical domain feature extraction at 180.15 kHz through electrostatic actuation [273]. Critically, this system compensates for low-frequency mechanical decay using 1.25 MHz-rate electrical sampling, achieving 99.8% accuracy in speech classification tasks. This result demonstrates that cross-domain cooperative architectures can extract features at microwatt-level power and perform fast, programmable decisions at milliwatt-level power, reaching a system-level balance of energy efficiency, speed, and accuracy that is unattainable within a single physical domain.

By introducing two-dimensional materials and scaling devices to the nanoscale, embedded computing can be explored at higher operating frequencies and lower energy consumption. For example, a molybdenum disulfide nanodrum with a diameter of approximately 4 μm and a thickness of 5–13 nm achieves a fundamental resonance near 3 MHz due to its extremely low effective mass of about 10^{-15} kg. Frequency hysteresis in this structure enables nonvolatile mechanical memory, with optical interferometric readout demonstrating an ultra-low write energy on the order of 10^{-12} J [278]. This example highlights key traits of nanoscale embedded computing: dimensional scaling elevates attainable operating frequency, while ultrathin structures reduce switching energy through enhanced stress sensitivity. At the same time, functionality remains limited and highly sensitive to fabrication variability and environmental fluctuations, positioning such devices as specialized functional units rather than general-purpose computing cores.

8.2.2 | AI-enhanced Computing With Transducers

The central challenge of next-generation intelligent systems lies not only in high-precision sensing of individual physical quantities but in transforming multimodal information from diverse transduction pathways into structured, decision-ready representations under strict power and latency constraints. Within the unified transduction framework illustrated in Figure 1, signals

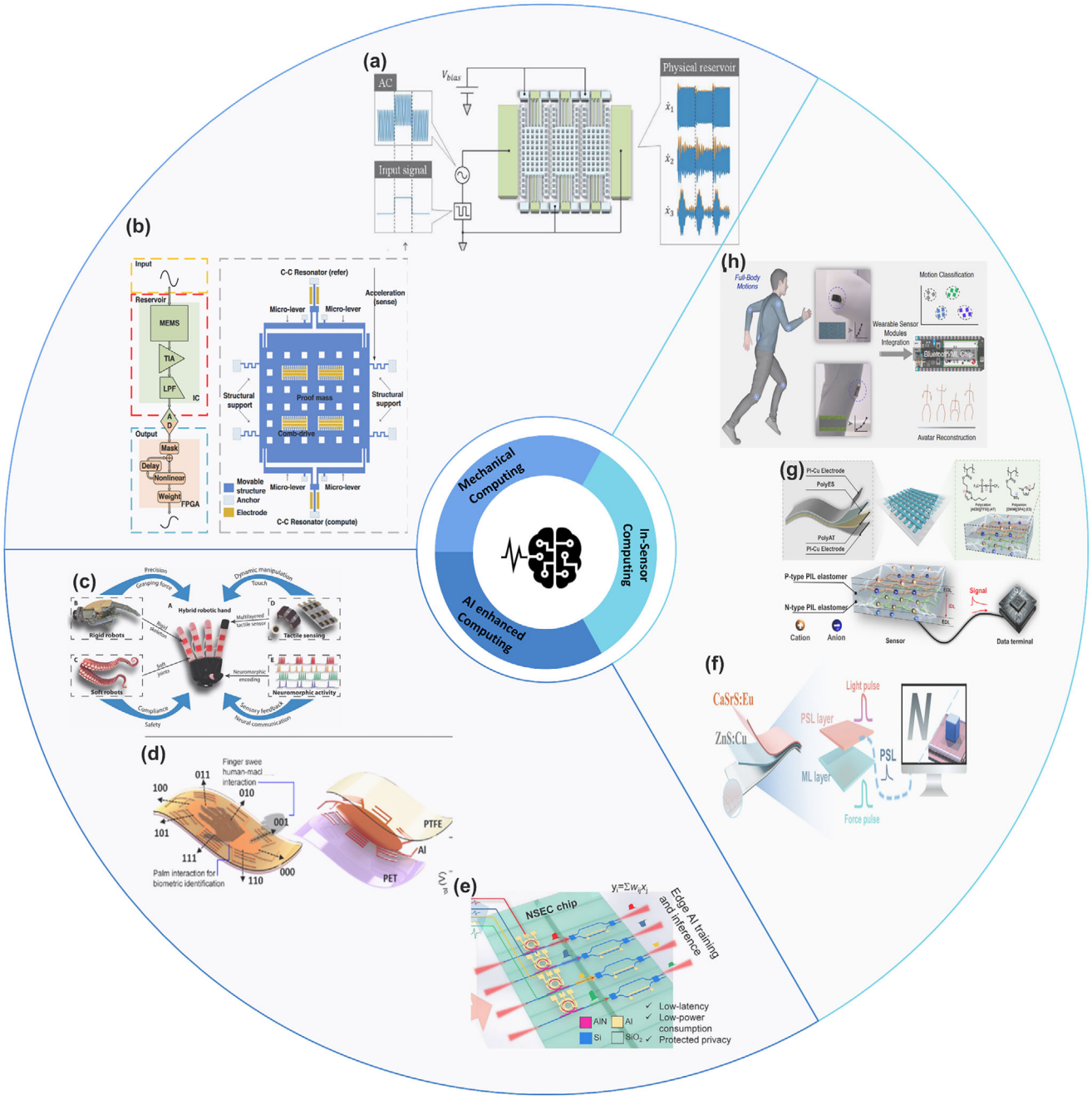

FIGURE 9 | Transducer-integrated multiscale platforms integrating sensing and in-sensor computing functionalities. (a) kHz-range Microscale coupled triple MEMS nonlinear resonator array using electrostatic coupling for mechanical edge computing. Reproduced with permission [272]. Copyright 2025, IEEE. (b) Microscale MEMS reservoir computing element with stiffness modulation for 180 kHz operation. Reproduced with permission [273]. Copyright 2024, The Author(s). (c) Hand-scale biomimetic prosthetic hand integrating layered tactile transducers, combining deformation sensing at Hz timescales and vibration sensing at kHz timescales. Reproduced with permission [274]. Copyright 2025, AAAS. (d) Wearable triboelectric photonic interface combining centimeter-scale flexible electrodes with microring for bio-signal to optical-carrier conversion spanning Hz to MHz frequencies. Reproduced with permission [275]. Copyright 2022, AAAS. (e) Microscale CMOS-compatible bilayer AlN/Si photonic platform enabling EO transduction with 10 GHz bandwidth for integrated optical feature extraction and on-chip matrix–vector multiplication. Reproduced with permission [33]. Copyright 2025, The Author(s). (f) Mesoscale mechano-optical artificial synapse based on mechano-luminescent and persistent-luminescent layers with millimeter microdome units in diameter operating on sub-Hz to Hz timescales. Reproduced with permission [276]. Copyright 2025 Wiley-VCH GmbH. (g) Mesoscale iontronic artificial skin built from polyelectrolyte elastomer arrays that enable multimodal pressure, temperature, and ionic current transduction with response in the Hz to kHz band. Reproduced with permission [277]. Copyright 2025 Wiley-VCH GmbH. (h) Wearable MXene strain sensor system using tunable wrinkle topology for full-body motion capture operating at Hz-level dynamics. Reproduced with permission [71]. Copyright 2022, The Author(s).

such as pressure, texture, temperature, and light are first mapped through their respective optimal physical mechanisms into the electrical or optical domain, forming parallel, heterogeneous feature streams with clear physical semantics. The AI–transducer co-design paradigm builds on this division of labor: rather than processing raw physical signals directly, embedded AI operates after high-fidelity physical-to-information conversion, performing feature alignment, fusion, and semantic inference, hence fuses neural algorithms with multi-physics signals to elevate systems from raw sensing to semantic inference [21, 57, 279].

Shifting information processing away from centralized digital computation and embedding it in a distributed manner at the site of physical sensing and interaction is a critical step toward intelligent systems. The AI–physics co-design paradigm offers a clear system architecture for this transition. Its essence is not a simple serial connection of sensing and computing modules, but the organization of mature multiphysics transduction mechanisms into composable, reconfigurable, and evolvable system-level capability units through heterogeneous integration and co-design. Within this framework, transducers are no longer passive data sources. Instead, their physical specificity enables front-end filtering and structuring of information across frequency, sensitivity, and power dimensions. Embedded AI extends beyond high-level inference to act as a system-level scheduler and coordinator, dynamically configuring transducer operating states and selecting processing pathways according to task objectives. In this way, sensing, computation, and actuation are jointly optimized within a unified transduction framework.

At the biomechanical sensing level, coordination is first realized by exploiting complementary physical transduction mechanisms to jointly construct a comprehensive feature representation of complex stimuli. In Figure 9c, the role of the physical front end is to convert low-frequency, unstructured biomechanical motions below 50 Hz, such as gait or gestures, into electrical signals with informative temporal features. For example, a biomimetic prosthetic hand integrating piezoresistive and piezoelectric units employs a piezoresistive layer with a bandwidth of about 40 Hz to encode macroscopic contact force and shape, while a piezoelectric layer with kHz bandwidth simultaneously captures fine texture-induced vibrations. After hardware-level preprocessing, the combined outputs are fused by a support vector machine classifier, achieving a material recognition accuracy of 98.38% [274]. A more advanced level of system integration is demonstrated in identity authentication. Figure 9d shows kHz triboelectric signals generated by macroscopic palm contact and skin bioelectric signals are jointly coupled into an aluminum nitride microring resonator operating at a 1550 nm optical carrier [275]. In this architecture, the physical domain acts as a primary coordinator, merging multimodal electrical signals into a unified optical feature stream. A backend convolutional neural network then serves as a higher-level coordinator, disentangling and identifying specific biometric features to achieve a 90% user authentication accuracy. This illustrates a hierarchical progression from physical hardware coordination to algorithmic model coordination.

To enable fine-grained environmental interaction, flexible large-area distributed sensor arrays must adapt their multimodal sensing outputs for AI processing. The core requirement is to encode heterogeneous signals arising from different physical mechanisms into spatiotemporally aligned and feature-decoupled data streams. A representative example is a millimeter-scale multilayer flexible sensor that uses a single contact–separation mechanism to simultaneously generate differentiated electrical signals sensitive to pressure, material properties, and curvature under 15.9 Hz excitation [67]. Through co-design of the physical structure and readout circuitry, partial feature decoupling is achieved at the signal generation stage. As a result, multichannel time-series data can be directly processed by a lightweight long short-term memory network, achieving 99.2% recognition accuracy. This illustrates that AI-oriented sensor design benefits from embedding modality-specific physical responses to shift low-level feature separation into the physical domain, allowing algorithms to focus on higher-level correlation learning. A similar principle is demonstrated in flexible electronic skin based on electrical impedance tomography. Using 1 kHz excitation and a 10 frames-per-second imaging rate, the system reconstructs low-resolution three-dimensional pressure distributions directly at the physical layer [280]. This point-to-area information transformation effectively compresses high-dimensional contact data into image-like representations compatible with AI vision models, enabling over 80% accuracy in character recognition. Collectively, these studies highlight an effective pathway for integrating flexible sensing with AI by reducing information redundancy through physical encoding and replacing post hoc computation with structured signals.

The highest level of coordination emerges in a complete sensing–decision–actuation loop, where AI functions as a real-time hub that dynamically coordinates sensory inputs and physical actuation outputs to enable adaptive interaction. Such systems typically require end-to-end latencies below 300 ms, with decision accuracy and timeliness being equally critical. Representative examples include a digital embroidery smart glove that integrates piezoresistive sensors sampled at 50 Hz with electromagnetic actuators operating at 100 Hz. An AI model manages the full sensing-to-haptic-feedback loop, achieving 94% skill transfer accuracy after only 15 s of training [281]. In more advanced systems, multimodal five-degree-of-freedom stretchable electromagnetic actuators generate normal and rotational shear stimuli, and, when combined with AI-based user feedback fusion, reach near-100% recognition accuracy [282]. This transition marks AI's transfer from a passive interpreter to an active coordinator of physical interaction.

To meet extreme requirements for privacy, latency, and energy efficiency, coordination shifts to the network edge, where specialized AI models are co-designed with the specific output characteristics of transducers under stringent resource constraints, including milliwatt-level power and kilobyte-to-megabyte memory budgets. For example, a spiking neural network edge chip classifies electromyography signals with a latency of 5.7 ms at 41 mW, sacrificing accuracy to 74% but meeting the extreme real-time and power requirements of implantable devices [283]. Similarly, a paper-based PEDOT:PSS electrochemical sensor achieves 100% detection accuracy by co-designing its AI algorithm with the sensor's characteristic low-frequency impedance response to fungal metabolites [284]. At the edge, this coordination centers on tight matching and joint optimization between the physical output characteristics of transducers and the computational structure of machine learning models.

Ultimately, to enable high-speed unified processing of cross-domain and cross-scale signals, photonic computing chips are introduced into the system architecture as high-performance coprocessors, providing a reconfigurable analog computing plane that coordinates with diverse front-end transducers. As illustrated in Figure 9e, a thin-film aluminum nitride microring resonator modulates kHz sensor signals into the optical domain via the electro-optic effect, while a silicon Mach–Zehnder interferometer array implements an optical neural network with weight tuning at a 5.6 V half-wave voltage. This system achieves optical-domain feature extraction and inference on microsecond to nanosecond timescales, delivering 96.77% gesture recognition accuracy with an end-to-end latency of 10 ns [33]. This example points to a clear frontier: on-chip photonic processors are not intended to replace transducers, but to function as AI coprocessors that provide an ultra-low-latency, highly parallel computing platform for information originating from mechanical, acoustic, electrochemical, and other physical front ends, once mapped into the electrical or optical domain. The key system-level challenge lies in developing efficient and compact electro-optic and optoelectronic interfaces to minimize signal conversion overhead.

8.2.3 | In-Sensor Computing With Transducers

In-sensor computing represents an emerging paradigm in intelligent perception, in which sensing and computation are co-located in the same spatiotemporal domain through heterogeneous integration and co-design, enabling signal extraction and transformation at the point of generation. In this framework, computation does not rely on a single general-purpose processing unit. Instead, it is realized through multiphysics transduction mechanisms, such as electromagnetic confinement in waveguides, mechanical vibrations of resonant membranes, or carrier dynamics in ionic gels, which collectively form composable, reconfigurable, and evolvable embedded computational capabilities at the system level [28].

The central design principle is to select and combine physical effects that best match the intrinsic characteristics of the target information, including spatiotemporal vibration patterns, chemical spectra, or tactile textures, thereby allowing system architecture, power consumption, and latency to be determined by the physical properties of the signals themselves. This AI–transducer co-design paradigm provides a rigorous foundation for next-generation intelligent sensing systems, enabling deep integration of perception, computation, and actuation.

At the materials and device level, in-sensor computing exploits intrinsic physical responses of functional materials, such as ion migration, mechano-optical transduction, and piezoresistive effects, to directly map environmental stimuli into analog states with computational meaning, thereby physically merging sensing with early-stage computation. This fusion offers pronounced energy-efficiency advantages and admits diverse implementations. For instance, Figure 9g shows an 8×8 iontronic electronic skin based on a polyionic liquid elastomer that leverages ion migration and recombination dynamics within a p–n-junction-like architecture to simultaneously respond to pressure, temperature, and electric fields in a single physical process [277]. By unifying multimodal sensing within a single ionic mechanism and patterning the electrode array, the spatiotemporal response becomes reconfigurable as a physical reservoir, enabling on-sensor handwritten digit recognition. Similarly, for wearable visuo-tactile fusion, Figure 9f shows a 0.5 mm microcapsule integrating a ZnS:Cu luminescent layer converts mechanical pressure into optical signals and exploits a 0.34 s luminescence decay constant together with a ~180% paired-pulse facilitation effect to realize synapse-like short-term memory and plasticity [276]. A stretchable OECT array leverages ion-gel neuromorphic modulation in the 10^2–10^3 Hz window under sub-1 V bias to achieve 90% EMG classification accuracy, demonstrating soft, conformable in-sensor intelligence [285]. These examples illustrate how opto-mechanical coupling at the material level can be composed into sensing units with inherent temporal filtering and learning capability.

To enable real-time processing of dynamic signals such as vibration, posture, and waveforms, in-sensor computing further exploits physical phenomena, including resonance, nonlinear dynamics, and charge accumulation in micro- and nanostructures, to construct analog computational front ends close to the sensing site. The processing speed is fundamentally set by the intrinsic physical time constants of the devices. For example, a sealed aluminum nitride circular membrane with a diameter of 1900 μm employs its 52.7 kHz mechanical resonance as a short-term memory carrier, forming a physical reservoir with 128 virtual nodes for posture recognition [286]. Here, the decay time of mechanical resonance, determined by the quality factor, together with thermal stability achieved through vacuum encapsulation and anchor-loss engineering, defines the operational window and robustness of this computational primitive. Complementarily, a stacked-capacitor architecture exploits charge accumulation and redistribution to perform analog multiply–accumulate operations directly within a predefined 110 ms time window, with an energy consumption of only 493 μW [287]. In this design, temporal integration is physically implemented via RC time constants, while programmable windows and interleaved sampling enable temporal reconfigurability of the analog computation.

An even more extreme example is a fully mechanical neural network that uses electrostatic pull-in and release hysteresis of MEMS actuators as memory elements and mechanically coupled cantilever arrays for signal propagation. This system achieves continuous-time waveform classification at approximately 195 Hz without relying on semiconductor materials [288], demonstrating how electrostatic–mechanical coupling and structural dynamics can be composed into a self-contained physical computing network suitable for operation in extreme environments.

For applications requiring high bandwidth and ultra-low latency, such as rapid event detection and broadband signal analysis, in-sensor computing naturally shifts toward photonic carriers. By exploiting optical propagation, interference, and wavelength multiplexing, linear and nonlinear transformations can be performed concurrently with signal generation. A representative example is a spatiotemporal reservoir computing system built from a 1.12 km single-mode fiber and nonlinear feedback from a semiconductor laser [289]. Vibration signals are mapped onto an optical delay of approximately 11.2 μs and expanded through about 250 virtual nodes, achieving 100% event recognition accuracy. Here, fiber

propagation delay, traditionally a limitation, is repurposed as a temporal memory resource, with periodic wavelength locking ensuring long-term stability.

At the chip scale, this concept is realized through highly compact photonic co-design. In a silicon-based integrated platform operating in the 3.65–3.8 μm mid-infrared range, molecular fingerprint spectra are acquired directly on chip and processed in real time by a programmable Mach–Zehnder interferometer network performing optical convolution [290]. Spectral absorption provides sensing, while the interferometric network executes computation, seamlessly coupled within the optical domain. With only kHz-rate electronic tuning, the system achieves feature extraction across THz optical bandwidths. Together, these examples highlight the unique advantages of photonic in-sensor computing in bandwidth, latency, and composability, and underscore the value of treating optical physical processes themselves as computational resources.

Pushing computation to the nanophotonic scale enables strong light–matter interactions enhanced by microcavities, achieving THz optical processing bandwidths together with extremely high computational density exceeding 1 TOPS mm^{-2}. A representative example is an optical multiply–accumulate system based on a 4×4 microring resonator crossbar array. Although its reconfigurability is limited by kHz-scale electronic tuning, the core computations proceed in parallel at optical frequencies, enabling 45-class protein classification with an accuracy of 97.58% [291]. This result highlights a defining characteristic of nanophotonic in-sensor computing: system throughput and energy efficiency are dominated by ultrafast photonic parallelism, while functional reconfigurability is provided by slower yet flexible electronic control, exemplifying a multiphysics co-design paradigm.

Extending computation and sensing toward the quantum-limited optoelectronic interface further pushes sensitivity to fundamental bounds, allowing signal-to-noise optimization at the point of information generation. Superconducting nanowire single-photon imaging systems demonstrate this capability, achieving 92.22% image classification accuracy under extremely low-light conditions with an average of only 0.12 photons per pixel [292]. This example unifies quantum noise limits in sensing with computational decision-making at a single physical interface, underscoring the unique potential of in-sensor computing for quantum information processing.

Ultimately, building powerful intelligent sensing systems requires hierarchical coordination of embedded computing units across different physical domains, forming an energy-optimal heterogeneous processing pipeline that spans from raw sensing to abstract decision-making. Within this architecture, each layer is assigned tasks best matched to its physical nature. For example, the front-end layer can be implemented using MXene-based strain topological sensors. Through localized thermal shrinkage, these sensors form tailored topological structures of Figure 9h that directly encode low-frequency strains around 10 Hz into high signal-to-noise resistance variations. This physical encoding enables precise human posture tracking with an error of 3.5 cm while reducing total system power consumption by 71%, illustrating how front-end physical computation can substantially improve both accuracy and energy efficiency [71]. The intermediate processing layer can be implemented using optical convolution processors or analog reservoir computing units, which perform high-throughput, low-latency transformations on feature-encoded data from the front end. The decision layer may then be assigned to a superconducting nanowire single-photon imager, operating near the quantum limit for image sensing and pulse encoding, or to a compact digital coprocessor that executes the final classification.

Building on these advances, the in-sensor computing paradigm is evolving from fixed, preconfigured computation toward adaptive learning, in which weight updates and algorithmic optimization are executed directly within sensing nodes, enabling dynamic adaptation to environmental changes. For example, a ferroelectric photosensor neural network (FE-PS-NET) uses the nonvolatile polarization states of ferroelectric materials as tunable weights. With a write speed of 100 ns and an optical response time of 30 μs, the system performs in-pixel training and inference, achieving recognition speeds 50 times faster than conventional architectures while maintaining near-zero static power consumption [293]. Device nonuniformity and imprint effects are mitigated through in-array calibration and adaptive refresh strategies, ensuring robust learning at the material-physics level. This capability marks a transition from merely reconfigurable to truly evolvable in-sensor computing. Computational functionality is no longer fixed by fabrication-defined structures but can be continuously optimized in response to incoming data streams, establishing a physical foundation for autonomous, self-adapting intelligent sensing systems.

The three pathways discussed in this chapter form a coherent technological progression that elevates multiphysics transduction mechanisms into higher-level system capabilities. Mechanical computing with transducers establishes the foundation by exploiting intrinsic nonlinearity and temporal dynamics in mechanical, acoustic, and charge-based processes to realize logic, memory, and feature extraction at the physical layer. Building on this, AI-enhanced computing with transducers introduces algorithms as system-level coordinators, enabling multimodal fusion and real-time reconfiguration of sensing, computation, and actuation within closed perception–decision–action loops. In-sensor computing with transducers further deepens this integration by merging sensing and computation at the physical interface, extending functionality from fixed reconfigurability toward adaptive and evolvable learning across photonic, electronic, and ionic domains.

Together, these pathways reveal a unifying design principle: the performance of next-generation intelligent microsystems is determined not by the limits of any single mechanism, but by the ability to orchestrate heterogeneous physical primitives at the system level. System functionality emerges from the types, scales, and interconnections of available primitives, ranging from kHz mechanical resonators and microsecond acoustic delays to THz photonic processors and plastic ionic devices. Through cross-domain co-design, these elements can be assembled into task-specific computational graphs, dynamically reconfigured by embedded intelligence, and progressively optimized through in situ learning. Consequently, the design focus shifts from optimizing isolated transducers to constructing open system

architectures capable of flexibly integrating, scheduling, and evolving multiphysics resources.

8.3 | Sustainable Applications via Transducers

The realization of sustainable intelligent systems does not rely on any single highly efficient energy conversion mechanism. Instead, it depends on the system's ability to organize multiple physical transduction mechanisms in accordance with the spectral distribution and temporal uncertainty of environmental excitations, thereby establishing a stable and scalable foundation for both energy and information. In real-world environments, available energy is typically distributed across disparate frequency bands, ranging from sub-hertz to tens of hertz, with amplitudes, intermittency, and statistical properties that are strongly scenario dependent. This fundamental constraint dictates that sustainable nodes must first exhibit composability, namely the capacity to broaden the effective energy harvesting bandwidth and improve output stability through the parallel integration and cooperative operation of heterogeneous transducers.

At this stage, system optimization moves beyond maximizing energy harvesting efficiency and toward the functional reuse and reconfiguration of energy transduction mechanisms [294]. When the outputs of transducers are reinterpreted as representations of environmental state variables, energy harvesting and sensing can be co-realized within the same physical processes, leading to substantial reductions in system volume and power consumption. Ultimately, only when energy management, sensing, and communication are jointly orchestrated at the system level, and co-designed with ultra-low-power circuits and algorithms, can sustainable nodes evolve into intelligent microsystems with long-term autonomous operation [65, 295].

When addressing low-frequency (<10 Hz), large-displacement environmental excitations such as human motion, ocean waves, and wind, electromagnetic and triboelectric mechanisms tend to dominate due to their high adaptability to slow, large-strain motions. In this frequency regime, piezoelectric materials are often disadvantaged as a result of impedance mismatch and limited strain tolerance [296]. Therefore, the key to system design lies in leveraging hybrid mechanisms together with macroscopic structures to maximize energy extraction. For example, a hybrid reciprocating energy harvester that integrates piezoelectric, electromagnetic, and triboelectric units is specifically designed to capture human motion energy at approximately 4 Hz, with the parallel operation of multiple mechanisms supplying power to wearable nodes [297]. An electromagnetic harvester with a non-resonant rotor of 65 mm diameter delivering 10.4 mW at 8 Hz during human motion [298]. For ocean wave energy in the 0.25–2 Hz range, a pendulum-based hybrid triboelectric–electromagnetic device converts the slow oscillatory motion of waves into contact–separation and magnetic flux cutting, enabling broadband response and directly powering a Bluetooth sensor module [299]. Wind-driven systems have been realized with rotational tapered rollers that couple triboelectrification and electromagnetic induction [300]. These examples collectively reveal a central design paradigm for low-frequency energy harvesting: system performance is jointly governed by the displacement amplification enabled by mechanical structures and the parallel output characteristics of multiple physical transduction mechanisms. Beyond this, structural engineering approaches such as metamaterials enable spatial reconfiguration of energy fields, leading to order-of-magnitude efficiency gains. For instance, an ocean-scale metamaterial plate can concentrate wave-induced elastic strain energy, achieving an energy density of 81 W m^{-3} in the 0.9–2 Hz frequency range [301]. In fluidic environments, an electromagnetic turbine of only 28 mm diameter generates nearly 0.9 mW under irrigation flows of 10–50 L min^{-1}, serving simultaneously as a self-powered flow sensor [302]. Collectively, these examples illustrate how low-frequency harvesters employ large displacements, rolling magnets, and hybrid coupling to transform low-frequency excitations into multi-mechanism activation.

When the excitation frequency shifts into the acoustic and ultrasonic regimes (kHz–MHz) and device dimensions are reduced to the micrometer scale, piezoelectric MEMS mechanisms become a dominant solution owing to their high intrinsic resonance frequencies and strong electromechanical coupling. In this frequency range, system composability is primarily realized through mechanical frequency upconversion: low-frequency environmental energy is efficiently mapped onto high-frequency piezoelectric resonant modes via impact, inertial, or contact-driven processes, enabling efficient and stable energy and signal transduction. For example, rectangular diaphragm arrays with an active area of only 2–5 mm^2 can operate within the 170–930 kHz range, delivering nanowatt-level power output suitable for implantable biomedical devices [303]. A more representative example is a composite iCUPE that integrates a low-frequency flexible nanofiber piezoelectric generator (LF-PEG) with a high-frequency thick-film PZT cantilever (HF-PEG), shown in Figure 10a [304]. Through the frequency up-conversion (FUC) mechanism, LF-PEG and HF-PEG work together, outperforming conventional single-mode PEGs. This design employs mechanical impact to effectively map low-frequency vibrations in the 10–46 Hz range onto the high-frequency resonant modes of the HF-PEG. These results demonstrate that, through coordinated design of heterogeneous mechanical structures, physical mechanisms operating in different frequency regimes can be efficiently coupled in a relay-like manner, thereby fundamentally overcoming the limitations imposed by the narrow bandwidth of individual transducers.

As research progresses, reliance on periodic mechanical vibrations moves to the frontier of sustainable transduction, which is increasingly defined by the introduction of new physical effects that extend energy harvesting from dynamic mechanical excitations to static or quasi-static environmental gradient fields, including temperature, humidity, and illumination. The core principle of such harvesters lies in exploiting intrinsic material properties to generate sustained responses to specific gradients. For example, a compact thermoelectric device based on phase-change materials, with a characteristic size of approximately 3.6 cm, induces a pseudo-Seebeck effect by engineering differences in phase-transition temperatures among composite materials. This design enables stable voltage output under thermal cycling between 25 and 80°C, making it well suited for structural monitoring in building and aerospace applications [310]. In another approach, an ion-diode thin film with a thickness of only

FIGURE 10 | Sustainable Applications via Transducers. (a) A iCUPE for energy harvesting and intelligent sensing. Reproduced with permission [304]. Copyright 2023, American Chemical Society. (b) Multifunctional hydrogel-based self-powered outdoor plant monitoring system. Reproduced with permission [66]. Copyright 2024, The Author(s). (c) Self-powered gyroscope ball using a triboelectric mechanism. Reproduced with permission [305]. Copyright 2017 WILEY-VCH Verlag GmbH & Co. KGaA, Weinheim. (d) Self-powered smart insole for gait monitoring and recognition. Reproduced with permission [306]. Copyright 2025, The American Association for the Advancement of Science. (e) Fabric-reinforced functional insole with superior durability and antifracture properties for biomechanical energy harvesting and AI-powered motion monitoring. Reproduced with permission [307]. Copyright 2024 Wiley-VCH GmbH. (f) Breathable Nanogenerators conformally attached to plant leaves for sustainable energy harvesting and intelligent agricultural monitoring. Reproduced with permission [308]. Copyright 2021, American Chemical Society. (g) Ultrathin and highly conductive electronic tattoo (e-tattoo) for real-time and non-invasive measurement of plant immune responses. Reproduced with permission [309]. Copyright 2025, The Author(s).

6–15 μm simultaneously couples ambient humidity diffusion and electromagnetic radiation. Through the synergistic action of ionic transport and interfacial polarization, the device generates output voltages of up to 0.59 V, achieving integrated energy harvesting, storage, and transmission within a single structure [311].

Furthermore, ionic-carrier dynamics mechanisms demonstrate strong potential for deep integration of energy harvesting and information sensing. As shown in Figure 10b, an ionic hydrogel harvester with a thickness of approximately 300 μm employs a PVA/PAAm/LiCl/Gly hydrogel sandwiched between Cu–Al

electrodes. Its stable direct-current output originates from a sustained oxygen reduction reaction at the copper cathode, yielding an average power density of 1.9 W m^{-3} [66]. More importantly, the output voltage exhibits a linear dependence on the relative water content of plant leaves, enabling the device to perform noninvasive plant hydration monitoring while simultaneously harvesting energy. This functionality can be further extended to self-powered wind and light-sensing units. Collectively, these studies demonstrate that, by leveraging nontraditional physical processes such as phase-change enthalpy, ionic diffusion, interfacial polarization, and electrochemical reactions, transducers can continuously extract energy from more ubiquitous environmental potential fields while concurrently decoding environmental information. This capability reflects the evolvability of sustainable systems at the mechanism level and substantially broadens their application scope and long-term deployment potential.

The evolution of sustainable transducers is fundamentally driven by revealing and exploiting the intrinsic physical unity between energy harvesting and information sensing, and by extending this unity into autonomously operating intelligent microsystems through system-level co-design. This progression follows a clear hierarchical pathway. First, the inherent dual role of energy transduction mechanisms as both power generators and signal carriers is leveraged to achieve basic functional reuse within a single physical process. Next, stable and reliable self-powered sensing nodes are constructed through the combination of heterogeneous energy harvesting and sensing units together with coordinated power management. Ultimately, the integration of embedded communication and algorithmic intelligence enables environmental interaction, decision-making, and long-term autonomous operation. This stepwise transition from physical mechanisms to system intelligence systematically illustrates how multiphysics transduction mechanisms can be transformed, through coordinated design, into composable, reconfigurable, and evolvable system-level capabilities.

In electromagnetic and triboelectric energy harvesters, this mapping between electrical output and environmental excitation is particularly explicit, allowing the output signals to be directly exploited for quantitative environmental sensing. For example, in a micro-scale irrigation turbine system, the induced current exhibits a linear dependence on water flow velocity, enabling the device to function simultaneously as a power generator and a self-powered flow meter [302]. In wind-driven hybrid harvesters, the rotational speed corresponds uniquely to the output voltage, thereby realizing self-powered wind-speed monitoring [300]. In ocean wave energy harvesting scenarios, the output amplitude and frequency of triboelectric nanogenerators directly encode wave intensity and periodicity, providing access to key ocean dynamic parameters [299, 301]. These results demonstrate that the readout circuitry of energy harvesters can be directly repurposed as sensing interfaces without the need for additional sensor elements. This dual use substantially reduces system complexity while enhancing integration density.

The first level of functional integration is rooted directly in physical laws: the physical coupling mechanisms that govern energy transduction produce electrical outputs, including voltage, current, and frequency, that deterministically encode the corresponding environmental inputs. This intrinsic dual functionality allows transducers to operate naturally as self-powered sensors, eliminating the need for additional, standalone sensing elements. In electromagnetic harvesters, induced current is proportional to flow velocity or rotational speed, thereby turning irrigation turbines into autonomous flow meters and wind-driven hybrids into self-powered anemometers. Transducers like TENG naturally couple output amplitude with contact frequency, making them suitable for motion recognition in wearable systems [297]. A T-ball device with a diameter of approximately 65 mm (Figure 10b) integrates Al/PTFE and Al/PDMS electrodes with 6.3 mm steel beads to realize contact–separation and sliding coupling [305]. Its open-circuit voltage increases from 8 V to 32 V as the rotation diameter expands from 1 cm to 5 cm, while the current rises from 0.15 μA to 0.35 μA, with stable performance maintained in water at 30–90°C. Beyond energy harvesting, it also provides tri-axial acceleration and angular velocity sensing, enabling gesture and activity recognition and demonstrating the integration of low- to mid-frequency motion energy harvesting with multimodal sensing. Ocean-wave TENG harvesters provide direct indicators of wave strength and periodicity. The dual role of powering and sensing exemplifies the principle that energy harvesting transducers are not mere battery substitutes but self-sustained transducers forming the foundation of distributed IoT.

To achieve system-level energy autonomy, functional integration advances to a second level: a heterogeneous combination of dedicated sensing front ends with efficient energy harvesting modules, coordinated through power management circuits that regulate energy acquisition, storage, and distribution to form a complete sensing–power hardware loop. At this level, composability is manifested through a modular system architecture. A representative example is a wireless self-powered intelligent insole system in Figure 10d [306]. This system integrates two key modules: a photovoltaic energy harvesting unit based on flexible perovskite solar cells, and a distributed pressure-sensing array composed of 22 porous carbon nanotube composite piezoresistive sensors. Electrical energy generated by the photovoltaic module is regulated and stored in a lithium-ion battery through power management circuitry, establishing a unified energy bus that supplies the sensing, processing, and Bluetooth communication chain. In this architecture, energy flow and information flow are deliberately decoupled. The harvesting module, with a conversion efficiency of approximately 15–20%, is optimized for maximal energy capture, while the sensing module, operating over a linear pressure range of 0–225 kPa, is optimized for high-precision mechanical measurement. The two are combined through standardized power and signal interfaces. The advantage of this approach lies in its clear functional partitioning and independent optimizability, which provide a robust foundation for complex system functionality.

Another representative example is a textile-enhanced functional insole system in Figure 10e that harvests biomechanical energy through a reinforced dual L-shaped structure coupled with a triboelectric mechanism, achieving a peak power output of 8214 μW and maintaining stable performance over 60 000 cycles [307]. Beyond powering external devices, the harvested energy is directly reused to support the system's own sensing and processing operations, exemplifying a locally sourced, locally consumed autonomy paradigm.

The highest level of functional integration is realized through cross-domain co-design of materials, devices, and algorithms, enabling the simultaneous execution of energy harvesting, information sensing, and in situ intelligent processing within a single system, thereby forming fully autonomous, full-stack microsystems. At this level, system reconfigurability and evolvability are unified. A representative example is a plant health monitoring system based on a waterproof and breathable triboelectric nanogenerator (WB-TENG). In Figure 10f, the plant monitoring system provides a representative example of sustainable sensing [308]. Its core component is a functionalized PVDF-HFP nanofiber membrane with a thickness of approximately 35 μm. A hierarchical micro–nanoporous structure endows the membrane with high hydrophobicity, maintaining high water vapor permeability. This combination allows long-term attachment to plant leaves without disrupting physiological activity. At the system level, the device simultaneously performs broadband energy harvesting, spanning from several hertz to several hundred hertz, and sensing of environmental stimuli such as wind and rain. The harvested energy directly powers integrated microenvironment sensing nodes and supports closed-loop operation through Bluetooth communication, achieving deep integration in which sensing and power generation share a common physical origin.

In Figure 10g, an ultrathin, biocompatible, substrate-free silver-nanowire (AgNW) network-based e-tattoo for monitoring plant immunity can respond via electrochemical impedance spectroscopy (EIS) [309]. The e-tattoo is transferred onto leaf surfaces via in-water transfer printing, a gentle and non-invasive process. With low resistance ($<5\ \Omega\ sq^{-1}$) and good stability, the e-tattoo conforms to trichome-rich leaves and outperforms metal and liquid-metal electrodes in EIS. Using the transgenic A. thaliana, the system realizes the long-term (>24 h) and continuous monitoring and detects the onset of NLR-mediated hypersensitive responses before visible symptoms(~3 h). This method provides a unique platform for monitoring the immune dynamics of plants, establishing a foundation for broader investigations across diverse immune pathways and environmental stresses.

In summary, the evolution of the functional integration paradigm can be understood as a progressive construction of viable technological pathways for sustainable applications. This evolution follows the logic of heterogeneous integration and co-design illustrated in the main figure. Systems advance along increasing dimensions of environmental information frequency and functional complexity, starting from low-power, conformal flexible sensing front ends, and gradually incorporating heterogeneous combinations of multi-source environmental energy harvesting mechanisms. Through this process, sensing, power supply, communication, and decision-making units are integrated to operate cooperatively within a unified physical framework, ultimately forming highly autonomous microsystems.

The direct outcome is the emergence of a new class of sustainable intelligent nodes that fundamentally differ from conventional monitoring devices. Rather than relying on continuous external power sources, these systems acquire energy and decode environmental information simultaneously through ongoing interaction with their surroundings. As a result, energy harvesting and environmental sensing become physically unified, elevating sustainability from a problem of energy substitution to a system-level capability for long-term autonomous operation. As emphasized in the main figure, by coordinating multiple physical degrees of freedom and achieving system-level integration, transducers evolve from isolated functional components into foundational building blocks that support complex system behaviors. This transformation enables intelligent systems to be deployed over long durations in the absence of fixed infrastructure and frequent human intervention, providing a clear and practical engineering foundation for large-scale, low-maintenance environmental monitoring networks, as well as for applications such as personalized health management and precision agriculture that critically depend on sustained operation.

9 | Conclusion and Outlook

This review has outlined how physical transduction mechanisms evolve across scales and frequency domains, but more importantly, it has shown that this evolution no longer follows a unidirectional path from demand to mechanism to implementation. Instead, we are witnessing a structural transition: from selecting optimal mechanisms under physical constraints to orchestrating heterogeneous mechanisms as composable system primitives.

Across mechanical, electrical, acoustic, and optical domains, a consistent pattern emerges: each verified mechanism operates within a bounded performance envelope defined by fundamental trade-offs between sensitivity, bandwidth, latency, energy, and integration complexity. These envelopes are not flaws to be eliminated but complementary capabilities to be coordinated [12, 312, 313]. These envelopes should not be viewed as deficiencies to be overcome, but as complementary and interoperable capabilities that can be strategically coordinated. As application requirements increasingly demand the simultaneous achievement of precision, reconfigurability, speed, and scalability beyond the reach of any single mechanism, the role of the transducer necessarily evolves. It ceases to function as an isolated interface and instead becomes an active node within a programmable, collaborative, and continuously evolving physical system.

In this context, heterogeneous integration should not be interpreted merely as a packaging strategy. Rather, it functions as an architectural language that enables distinct transduction mechanisms to interact coherently across disparate frequency bands, characteristic wavelengths, and device dimensions. At a fundamental level, heterogeneous integration can be understood along three complementary layers. At the materials layer, it involves the co-integration of dissimilar material systems and the deliberate engineering of their interfaces to access complementary coupling strengths, loss channels, and reliability constraints. At the device layer, it refers to the co-design and interconnection of heterogeneous transducer elements—electrical, mechanical, acoustic, and photonic—such that energy and information can be transferred across physical domains with controlled parasitics and impedance matching. At the functional layer, heterogeneous integration enables the intentional partitioning of sensing, modulation, sampling, and partial pre-processing between the transducer front-end and the electronic or photonic back-end,

forming a co-optimized system pipeline rather than a collection of isolated components.

Across frequency regimes, this architectural role becomes explicit. At low frequencies in the Hertz to kHz range, transducer interfaces with centimeter-to-millimeter CD support large deformations and high signal robustness, enabling energy-autonomous and multimodal sensing under intrinsic constraints on bandwidth and response speed [66, 277, 314–318]. As operating frequencies extend into the kHz to MHz regime, electromechanical systems with feature sizes from tens to hundreds of micrometers offer improved linearity, tunable bandwidth, and compatibility with on-chip signal conditioning and inference. When transduction shifts further toward GHz and THz carriers, subwavelength photonic and plasmonic structures with nanoscale confinement enable ultrafast response, high bandwidth density, and field-mediated information encoding, while introducing new constraints associated with optical loss, uniformity, and fabrication tolerance. Viewed collectively, these regimes highlight that the objective of high-performance transduction is no longer defined by a single metric, but by the coordinated optimization of size, bandwidth, dynamic response, noise characteristics, uniformity, and integrability, each rooted in specific coupling mechanisms and architectural choices [319, 320].

As the implementation of information processing moves closer to the physical front-end in the scenario of in-sensor computing and physics-assisted feature extraction, gains in system-level latency and energy efficiency are often accompanied by a reduction in interpretability and cross-platform reusability [37, 43, 287]. These trade-offs stem from the intrinsic nonlinearity, process variability, and environmental sensitivity of physical transduction mechanisms. Such constraints do not invalidate the architectural promise; rather, they refocus the design imperative toward creating observable, calibratable, and modular physical operators. In practice, this means transducer designs must expose accessible internal states [321], enable systematic calibration [158] and drift compensation [322, 323], and be characterized by well-defined performance—all while maintaining acceptable fallback modes. Consequently, the overarching design logic shifts: from optimizing performance within a single physical domain to the deliberate coordination of complementary mechanisms that collectively navigate multiple physical and system-level constraints.

Crucially, this transition reframes the role of the transducer from a domain-bridging element to an integrative platform through which functional capacity is constructed. Rather than being chosen solely to satisfy application-specific requirements and physical feasibility, transduction mechanisms are increasingly assembled, reconfigured, and redeployed to support new modes of interaction. Systems that jointly exploit piezoelectric and optoelectronic pathways, or that couple photothermal and electrostatic processes, illustrate that progress in transduction is driven not by the replacement of one mechanism with another, but by the coordinated organization of multiple mechanisms within a unified system [49, 324–331].

The chapters surveyed in this review, spanning flexible biointerfaces through THz optical modulators, collectively indicate that progress in transduction no longer hinges on the discovery of a singularly superior mechanism [332]. Instead, advancement increasingly depends on the ability to program physical systems in which sensing, actuation, and modulation are intrinsically coupled, jointly optimized, and dynamically reconfigurable. In this context, innovation is no longer defined by materials or individual mechanisms in isolation, but by the deliberate design of interactions among verified and interoperable physical processes.

From this perspective, system-level integration provides a generative framework for constructing transduction architectures that are reconfigurable, scalable, and tailored to specific application requirements. Such architectures enable unified platforms capable of adaptive bandwidth control, multimodal information extraction, energy-aware operation, and frequency-domain intelligence. Through this shift, transducers are repositioned from passive endpoints of energy conversion to active system elements that coordinate and govern the flow of physical information across domains.

Author Contributions

Aolei Xu: conceptualization, investigation, writing – original draft, and visualization. **Mengyao Xiao:** methodology, writing – review and editing. **Zhouli Sui:** methodology, writing – review and editing. **Daoye Zheng:** methodology, writing – review and editing. **Yinpeng Wang:** methodology, writing – review and editing. **Yuxin Liu:** data curation, writing – review and editing. **Luwei Wang:** supervision and project administration. **Huajun Liu:** supervision and editing. **Chengkuo Lee:** conceptualization, supervision, funding acquisition, and writing – review and editing.

Acknowledgements

The authors acknowledge the funding support from the National Research Foundation Competitive Research Program (NRF-CRP28-2022-0002), National Centre for Advanced Integrated Photonics (NCAIP) (NRF-MSG-2023-0002), RIE2025 MTC Individual Research Grant (M22K2c0084), National Semiconductor Translation and Innovation Centre (NSTIC) (M24W1NS005), RIE2025 Industry Alignment Fund – Industry Collaboration Projects (IAF-ICP I2301E0027), NUS Robotics Seed Grant Programme projects (A-8003283-00-00), NUS Robotics Seed Grant Programme projects (A-8003281-00-00), and Electro-Optic (EO)-Enhanced Memory on Lithium Niobate Integrated Platforms (A-8003551-00-00). The authors acknowledge the project support from Research Platform for Biomedical and Health Technology (RP-BHT, NUSRI).

Funding

National Research Foundation Competitive Research Program (NRF-CRP28-2022-0002), National Centre for Advanced Integrated Photonics (NCAIP) (NRF-MSG-2023-0002), RIE2025 MTC Individual Research Grant (M22K2c0084), RIE2025 Industry Alignment Fund – Industry Collaboration Projects (IAF-ICP I2301E0027), NUS Robotics Seed Grant Programme projects (A-8003283-00-00), NUS Robotics Seed Grant Programme projects (A-8003281-00-00), and Electro-Optic (EO)-Enhanced Memory on Lithium Niobate Integrated Platforms (A-8003551-00-00).

Conflicts of Interest

The authors declare no conflicts of interest.

Data Availability Statement

This article is a review, and the data are sourced from the references cited within the text. Data availability is not applicable to this article as no new data were created or analysed in this study.

References

1. A. S. Algamili, M. H. M. Khir, J. O. Dennis, et al., "A Review of Actuation and Sensing Mechanisms in MEMS-Based Sensor Devices," *Nanoscale Research Letters* 16, no. 1 (2021): 16, https://doi.org/10.1186/s11671-021-03481-7.

2. J. Christenson, "Sensors and Transducers," in *Handbook of Biomechatronics* (Elsevier, 2018), 61–93, https://doi.org/10.1016/B978-0-12-812539-7.00003-9.

3. C. Qiu, Z. Zhang, and Z. Xu, "Transparent Ultrasonic Transducers Based on Relaxor Ferroelectric Crystals for Advanced Photoacoustic Imaging," *Nature Communications* 15, no. 1 (Dec. 2024): 10580, https://doi.org/10.1038/s41467-024-55032-0.

4. G. Wissmeyer, M. A. Pleitez, A. Rosenthal, and V. Ntziachristos, "Looking at Sound: Optoacoustics with All-optical Ultrasound Detection," *Light: Science & Applications* 7, no. 1 (Aug. 2018): 53, https://doi.org/10.1038/s41377-018-0036-7.

5. T. Blésin, W. Kao, A. Siddharth, et al., "Bidirectional Microwave-optical Transduction Based on Integration of High-overtone Bulk Acoustic Resonators and Photonic Circuits," *Nature Communications* 15, no. 1 (2024): 6096, https://doi.org/10.1038/s41467-024-49467-8.

6. L. Yang, Y. Zhang, and W. Cai, "Electrochemically-driven Actuators: From Materials to Mechanisms and from Performance to Applications," *Chemical Society Reviews* 53, no. 11 (2024): 5956–6010, https://doi.org/10.1039/d3cs00906h.

7. W. J. Westerveld, M. Mahmud-Ul-Hasan, R. Shnaiderman, et al., "Sensitive, Small, Broadband and Scalable Optomechanical Ultrasound Sensor in Silicon Photonics," *Nature Photonics* 15, no. 5 (2021): 341–345, https://doi.org/10.1038/s41566-021-00776-0.

8. L. Midolo, A. Schliesser, and A. Fiore, "Nano-opto-electro-mechanical Systems," *Nature Nanotechnology* 13, no. 1 (2018): 11–18, https://doi.org/10.1038/s41565-017-0039-1.

9. N. Quack, A. Y. Takabayashi, H. Sattari, et al., "Integrated Silicon Photonic MEMS," *Microsystems & Nanoengineering* 9, no. 1 (2023): 27, https://doi.org/10.1038/s41378-023-00498-z.

10. Y. Koo, T. Moon, M. Kang, et al., "Dynamical Control of Nanoscale Light–Matter Interactions in Low-Dimensional Quantum Materials," *Light: Science & Applications* 13, no. 1 (2024): 30, https://doi.org/10.1038/s41377-024-01380-x.

11. J. R. Stone, X. Lu, G. Moille, D. Westly, T. Rahman, and K. Srinivasan, "Wavelength-accurate Nonlinear Conversion through Wavenumber Selectivity in Photonic Crystal Resonators," *Nature Photonics* 18, no. 2 (2024): 192–199, https://doi.org/10.1038/s41566-023-01326-6.

12. H. Zhou, D. Li, Q. Lv, and C. Lee, "Integrative Plasmonics: Optical Multi-effects and Acousto-electric-thermal Fusion for Biosensing, Energy Conversion, and Photonic Circuits," *Chemical Society Reviews* 54, no. 11 (2025): 5342–5432, https://doi.org/10.1039/d4cs00427b.

13. J. Yu, W. Yao, M. Qiu, and Q. Li, "Free-space High-Q Nanophotonics," *Light: Science & Applications* 14, no. 1 (2025): 174, https://doi.org/10.1038/s41377-025-01825-x.

14. D. Li, X. Wu, Z. Chen, T. Liu, and X. Mu, "Surface-enhanced Spectroscopy Technology Based on Metamaterials," *Microsystems & Nanoengineering* 11, no. 1 (2025): 60, https://doi.org/10.1038/s41378-025-00905-7.

15. S. Xu, W. Liu, X. Le, and C. Lee, "Unveiling Efficient Acousto-Optic Modulation in Silicon Photonic Devices via Lithium Niobate Using Transfer Printing," *Nano Letters* 41 (2024): 12964–12972, https://doi.org/10.1021/acs.nanolett.4c03622.

16. J. Su, W. Gao, Z. Cui, et al., "Large-Area Microtransfer-Printed Thin-Film Lithium Niobate-Silicon Nitride Microring Optical Filter with Nanosecond Tuning Speed," *ACS Photonics* 12, no. 4 (2025): 2062–2069, https://doi.org/10.1021/acsphotonics.4c02508.

17. Z. Li, N. Sharma, B. Lopez-Rodriguez, et al., "Heterogeneous Integration of Amorphous Silicon Carbide on Thin Film Lithium Niobate," *APL Photonics* 10, no. 1 (2025), https://doi.org/10.1063/5.0228408.

18. D. Liang and J. E. Bowers, "Recent Progress in Heterogeneous III-V-on-Silicon Photonic Integration," *Light Advanced Manufacturing* 2, no. 1 (2021): 59, 10.37188/lam.2021.005.

19. C. Xiang, W. Jin, D. Huang, et al., "High-Performance Silicon Photonics Using Heterogeneous Integration," *IEEE Journal of Selected Topics in Quantum Electronics* 28, no. 3 (2022): 1–15, https://doi.org/10.1109/JSTQE.2021.3126124.

20. X. Zhao, A. Li, G. Duan, C. Chen, and X. Zhang, "Integrating Microsystems with Metamaterials towards Metadevices," in *2019 20th Int. Conf. Solid-State Sensors, Actuators Microsystems Eurosensors XXXIII, TRANSDUCERS 2019 EUROSENSORS XXXIII* (Jan. 2019), 574–577, https://doi.org/10.1038/s41378-018-0042-1.

21. T. Leng, L. Li, and C. Lee, "Journal Editorial: Welcome to the New Era of AI-Enabled Sensing," *AI Sensors* 1, no. 1 (2025): 1, https://doi.org/10.3390/aisens1010001.

22. X. Liu, W. Liu, Z. Ren, et al., "Progress of Optomechanical Micro/Nano Sensors: A Review," *International Journal of Optomechatronics* 15, no. 1 (2021): 120–159, https://doi.org/10.1080/15599612.2021.1986612.

23. A. Kumar, A. Varghese, D. Kalra, et al., "MEMS-based Piezoresistive and Capacitive Microphones: A Review on Materials and Methods," *Materials Science in Semiconductor Processing* 169 (2024): 107879, https://doi.org/10.1016/j.mssp.2023.107879.

24. Z. Xue, Y. S. Gai, Y. Wu, Z. liu, and Z. Li, "Wearable Mechanical and Electrochemical Sensors for Real-time Health Monitoring," *Communications Materials* 5, no. 1 (2024): 211, https://doi.org/10.1038/s43246-024-00658-2.

25. C. Huang, S. Fujisawa, T. F. de Lima, et al., "A Silicon Photonic–electronic Neural Network for Fibre Nonlinearity Compensation," *Nature Electronics* 4, no. 11 (2021): 837–844, https://doi.org/10.1038/s41928-021-00661-2.

26. Y. Ma, W. Liu, X. Liu, N. Wang, and H. Zhang, "Review of Sensing and Actuation Technologies – from Optical MEMS and Nanophotonics to Photonic Nanosystems," *International Journal of Optomechatronics* 18, no. 1 (2024): 2342279, https://doi.org/10.1080/15599612.2024.2342279.

27. H. Wu, G. Yang, K. Zhu, et al., "Materials, Devices, and Systems of on-Skin Electrodes for Electrophysiological Monitoring and Human–Machine Interfaces," *Advancement of Science* 8, no. 2 (2021), https://doi.org/10.1002/advs.202001938.

28. H. Zhou, D. Li, and C. Lee, "Technology Landscape Review of in-Sensor Photonic Intelligence: From Optical Sensors to Smart Devices," *AI Sensors* 1, no. 1 (2025): 5, https://doi.org/10.3390/aisens1010005.

29. D.-H. Kim, N. Lu, R. Ma, et al., "Epidermal Electronics," *Science (80-)* 333, no. 6044 (2011): 838–843, https://doi.org/10.1126/science.1206157.

30. S. L. Ullo and G. R. Sinha, "Advances in Smart Environment Monitoring Systems Using Iot and Sensors," *Sensors* 20, no. 11 (2020): 3113, https://doi.org/10.3390/s20113113.

31. S. Zhou, G. Park, M. Lin, X. Yang, and S. Xu, "Wearable Ultrasound Technology," *Nature Reviews Bioengineering* 3 (2025): 835–854, https://doi.org/10.1038/s44222-025-00329-y.

32. C. Wang, M. Zhang, X. Chen, et al., "Integrated Lithium Niobate Electro-optic Modulators Operating at CMOS-compatible Voltages," *Nature* 562, no. 7725 (2018): 101–104, https://doi.org/10.1038/s41586-018-0551-y.

33. Z. Ren, Z. Zhang, Y. Zhuge, et al., "Near-Sensor Edge Computing System Enabled by a CMOS Compatible Photonic Integrated Circuit Platform Using Bilayer AlN/Si Waveguides," *Nano-Micro Letters* 17, no. 1 (2025): 261, https://doi.org/10.1007/s40820-025-01743-y.

34. S. Duan, H. Zhang, L. Liu, et al., "A Comprehensive Review on Triboelectric Sensors and AI-integrated Systems," *Materials Today* 80 (2024): 450–480, https://doi.org/10.1016/j.mattod.2024.08.013.

35. Y. Yang, X. Guo, M. Zhu, et al., "Triboelectric Nanogenerator Enabled Wearable Sensors and Electronics for Sustainable Internet of Things Integrated Green Earth," *Advanced Energy Materials* 13, no. 1 (2023): 2203040, https://doi.org/10.1002/aenm.202203040.

36. C. Xu, Y. Song, M. Han, and H. Zhang, "Portable and Wearable Self-powered Systems Based on Emerging Energy Harvesting Technology," *Microsystems & Nanoengineering* 7, no. 1 (2021): 25, https://doi.org/10.1038/s41378-021-00248-z.

37. X. Guo, Z. Zhang, Z. Ren, et al., "Advances in Intelligent Nano-Micro-Scale Sensors and Actuators: Moving toward Self-Sustained Edge AI Microsystems," *Advanced Materials* (2025): 10417, https://doi.org/10.1002/adma.202510417.

38. J. Wang, B. Wang, X. Yin, et al., "HgTe Nanocrystal-Gated Infrared Phototransistors with High Sensitivity, Extended Dynamic Range, and in-Sensor Image Processing Capability," *Small* 21, no. 34 (2025): 2505195, https://doi.org/10.1002/smll.202505195.

39. M. S. Haghighi, P. Firoozy, M. Kanygin, G. Williams-Jones, and B. Bahreyni, "Tunable Negative-Stiffness Nonlinear Microspring Design for High Performance MEMS Inertial Sensors," *IEEE Sensors Journal* (2025): 1–1, https://doi.org/10.1109/JSEN.2025.3606804.

40. Y. Song, Y. Hu, X. Zhu, K. Yang, and M. Lončar, "Octave-spanning Kerr Soliton Frequency Combs in Dispersion- and Dissipation-engineered Lithium Niobate Microresonators," *Light: Science & Applications* 13, no. 1 (2024): 225, https://doi.org/10.1038/s41377-024-01546-7.

41. Y. Huang, J. G. Flor Flores, Y. Li, et al., "A Chip-Scale Oscillation-Mode Optomechanical Inertial Sensor near the Thermodynamical Limits," *Laser & Photonics Reviews* 14, no. 5 (2020): 1800329, https://doi.org/10.1002/lpor.201800329.

42. K. Roy, D. Sim, L. Wang, et al., "A Generative AI-Assisted Piezo-MEMS Ultrasound Device for Plant Dehydration Monitoring," *Advanced Science* 12, no. 32 (2025): 04954, https://doi.org/10.1002/advs.202504954.

43. L. Abou-Hamdan, E. Marinov, P. Wiecha, P. del Hougne, T. Wang, and P. Genevet, "Programmable Metasurfaces for Future Photonic Artificial Intelligence," *Nature Reviews Physics* 7, no. 6 (2025): 331–347, https://doi.org/10.1038/s42254-025-00831-7.

44. Y. Hu, D. Zhu, S. Lu, et al., "Integrated Electro-optics on Thin-film Lithium Niobate," *Nature Reviews Physics* 7, no. 5 (2025): 237–254, https://doi.org/10.1038/s42254-025-00825-5.

45. S. Shekhar, W. Bogaerts, L. Chrostowski, et al., "Roadmapping the next Generation of Silicon Photonics," *Nature Communications* 15, no. 1 (2024): 751, https://doi.org/10.1038/s41467-024-44750-0.

46. D. Zhu, L. Shao, M. Yu, et al., "Integrated Photonics on Thin-film Lithium Niobate," *Advances in Optics and Photonics* 13, no. 2 (2021): 242, https://doi.org/10.1364/aop.411024.

47. D. Sun, Y. Zhang, D. Wang, et al., "Microstructure and Domain Engineering of Lithium Niobate Crystal Films for Integrated Photonic Applications," *Light: Science & Applications* 9, no. 1 (2020): 197, https://doi.org/10.1038/s41377-020-00434-0.

48. O. A. M. Abdelraouf, Z. Wang, H. Liu, et al., "Recent Advances in Tunable Metasurfaces: Materials, Design, and Applications," *ACS Nano* 16, no. 9 (2022): 13339–13369, https://doi.org/10.1021/acsnano.2c04628.

49. B. Lin, K. P. Ong, T. Yang, et al., "Ultrahigh Electromechanical Response from Competing Ferroic Orders," *Nature* 633, no. 8031 (2024): 798–803, https://doi.org/10.1038/s41586-024-07917-9.

50. M. Xiao, A. Xu, Z. Sui, W. Zhang, H. Liu, and C. Lee, "Multifunctional MEMS, NEMS, Micro/Nano-structures Enabled by Piezoelectric and Ferroelectric Effects," *Nanoscale Horizons* 10 (2025): 2744–2771, https://doi.org/10.1039/D5NH00386E.

51. Y. To, J. Du, C. Decroze, L. Huitema, A. Crunteanu, and H. Wong, "Phase Change Material-Driven Tunable Metasurface for Adaptive Terahertz Sensing and Communication in 6G Perceptive Networks," *Advanced Functional Materials* (2025): 15085, https://doi.org/10.1002/adfm.202515085.

52. J. Jung, W. Lee, W. Kang, E. Shin, J. Ryu, and H. Choi, "Review of Piezoelectric Micromachined Ultrasonic Transducers and Their Applications," *Journal of Micromechanics and Microengineering* 27, no. 11 (2017): 113001, https://doi.org/10.1088/1361-6439/aa851b.

53. Y. Birjis, S. Swaminathan, H. Nazemi, et al., "Piezoelectric Micromachined Ultrasonic Transducers (PMUTs): Performance Metrics, Advancements, and Applications," *Sensors* 22, no. 23 (2022): 9151, https://doi.org/10.3390/s22239151.

54. A. Valipour, M. H. Kargozarfard, M. Rakhshi, A. Yaghootian, and H. M. Sedighi, "Metamaterials and Their Applications: An Overview," *Proceedings of the Institution of Mechanical Engineers, Part L: Journal of Materials: Design and Applications* 236, no. 11 (2022): 2171–2210, https://doi.org/10.1177/1464420721995858.

55. S. Ghosh, J. O'Callaghan, O. Moynihan, et al., "Scalable Transfer Printing Approach to Heterogeneous Integration of InP Lasers on Silicon-on-insulator Waveguide Platform," *Applied Physics Letters* 125, no. 8 (2024): 81104, https://doi.org/10.1063/5.0223167.

56. E. Jung, H. Gehring, F. Brückerhoff-Plückelmann, et al., "Ultra-Broadband Plug-and-play Photonic Circuit Packaging with Sub-dB Loss," *arXiv* 41 (2025), https://arxiv.org/pdf/2505.21168.

57. J. Zhu, X. Liu, Q. Shi, et al., "Development Trends and Perspectives of Future Sensors and MEMS/NEMS," *Micromachines* 11, no. 1 (2020): 7, https://doi.org/10.3390/mi11010007.

58. P. Pitchappa, A. Kumar, H. Liang, et al., "Frequency-Agile Temporal Terahertz Metamaterials," *Advanced Optical Materials* 8, no. 12 (2020): 2000101, https://doi.org/10.1002/adom.202000101.

59. F. Huang, X. Shen, S. Wang, et al., "Toward Large-Scale Photonic Chips Using Low-Anisotropy Thin-Film Lithium-Tantalate," *Advanced Science* 12, no. 9 (2025): 2410345, https://doi.org/10.1002/advs.202410345.

60. M. Thomaschewski, V. A. Zenin, C. Wolff, and S. I. Bozhevolnyi, "Plasmonic Monolithic Lithium Niobate Directional Coupler Switches," *Nature Communications* 11, no. 1 (Feb. 2020): 748, https://doi.org/10.1038/s41467-020-14539-y.

61. J. Zhou, H. Zhang, Q. Qiao, et al., "Denoising-autoencoder-facilitated MEMS Computational Spectrometer with Enhanced Resolution on a Silicon Photonic Chip," *Nature Communications* 15, no. 1 (Nov. 2024): 10260, https://doi.org/10.1038/s41467-024-54704-1.

62. X. Wang, Z. Ruan, G. Chen, et al., "Ultrahigh Resolution Reconstructive Spectrometer Using a Disordered Cavity on Thin-Film Lithium Niobate," *ACS Photonics* 12 (2025): 3698–3705, https://doi.org/10.1021/acsphotonics.5c00663.

63. X. Zhou, R. Uppu, Z. Liu, et al., "On-Chip Nanomechanical Filtering of Quantum-Dot Single-Photon Sources," *Laser & Photonics Reviews* 14, no. 7 (2020): 1900404, https://doi.org/10.1002/lpor.201900404.

64. J. Liu, Y. Wang, Y. Liu, et al., "Recent Progress in Wearable near-Sensor and in-Sensor Intelligent Perception Systems," *Sensors* 24, no. 7 (2024): 2180, https://doi.org/10.3390/s24072180.

65. L. Liu, T. Hu, X. Zhao, and C. Lee, "Recent Progress in Blue Energy Harvesting Based on Triboelectric Nanogenerators," *Nanoenergy Advances* 4, no. 2 (2024): 156–173, https://doi.org/10.3390/nanoenergyadv4020010.

66. X. Guo, L. Wang, Z. Jin, and C. Lee, "A Multifunctional Hydrogel with Multimodal Self-Powered Sensing Capability and Stable Direct Current Output for Outdoor Plant Monitoring Systems," *Nano-Micro Letters* 17, no. 1 (2025): 76, https://doi.org/10.1007/s40820-024-01587-y.

67. X. Zhao, Z. Sun, and C. Lee, "Augmented Tactile Perception of Robotic Fingers Enabled by AI-Enhanced Triboelectric Multimodal Sensors," *Advanced Functional Materials* 34, no. 49 (2024): 2409558, https://doi.org/10.1002/adfm.202409558.

68. T. Chen, Z. Dai, M. Liu, et al., "3D Multimodal Sensing and Feedback Finger Case for Immersive Dual-Way Interaction," *Advanced Materials Technologies* 9, no. 5 (2024), https://doi.org/10.1002/admt.202301681.

69. M. Liu, Z. Dai, Y. Zhao, et al., "Tactile Sensing and Rendering Patch with Dynamic and Static Sensing and Haptic Feedback for Immersive Communication," *ACS Applied Materials & Interfaces* 16, no. 39 (2024): 53207–53219, https://doi.org/10.1021/acsami.4c11050.

70. B. Dong, Y. Yang, Q. Shi, et al., "Wearable Triboelectric–Human–Machine Interface (THMI) Using Robust Nanophotonic Readout," *ACS Nano* 14, no. 7 (2020): 8915–8930, https://doi.org/10.1021/acsnano.0c03728.

71. H. Yang, J. Li, X. Xiao, et al., "Topographic Design in Wearable MXene Sensors with in-sensor Machine Learning for Full-body Avatar Reconstruction," *Nature Communications* 13, no. 1 (2022), https://doi.org/10.1038/s41467-022-33021-5.

72. J. Xu, X. Guo, Z. Zhang, H. Liu, and C. Lee, "Triboelectric Mat Multimodal Sensing System (TMMSS) Enhanced by Infrared Image Perception for Sleep and Emotion-Relevant Activity Monitoring," *Advanced Science* 12, no. 6 (2025), https://doi.org/10.1002/advs.202407888.

73. Z. Shen, J. Li, H. Hu, et al., "A Review of Non-Invasive Continuous Blood Pressure Measurement: From Flexible Sensing to Intelligent Modeling," *AI Sensors* 1, no. 2 (2025): 8, https://doi.org/10.3390/aisens1020008.

74. M. Zhu, Z. Sun, Z. Zhang, et al., "Haptic-feedback Smart Glove as a Creative human-machine Interface (HMI) for Virtual/Augmented Reality Applications," *Science Advances* 6, no. 19 (2020): 1–15, https://doi.org/10.1126/sciadv.aaz8693.

75. Z. Zhang, T. He, M. Zhu, et al., "Deep Learning-enabled Triboelectric Smart Socks for IoT-based Gait Analysis and VR Applications," *npj Flexible Electronics* 4, no. 1 (2020): 1–12, https://doi.org/10.1038/s41528-020-00092-7.

76. M. Zhu, Z. Sun, and C. Lee, "Soft Modular Glove with Multimodal Sensing and Augmented Haptic Feedback Enabled by Materials' Multifunctionalities," *ACS Nano* 16, no. 9 (2022): 14097–14110, https://doi.org/10.1021/acsnano.2c04043.

77. X. Yu, Z. Xie, Y. Yu, et al., "Skin-integrated Wireless Haptic Interfaces for Virtual and Augmented Reality," *Nature* 575, no. 7783 (2019): 473–479, https://doi.org/10.1038/s41586-019-1687-0.

78. Z. Sun, M. Zhu, X. Shan, and C. Lee, "Augmented Tactile-perception and Haptic-feedback Rings as human-machine Interfaces Aiming for Immersive Interactions," *Nature Communications* 13, no. 1 (2022), https://doi.org/10.1038/s41467-022-32745-8.

79. Q. Shi, Z. Zhang, T. Chen, and C. Lee, "Minimalist and Multifunctional human Machine Interface (HMI) Using a Flexible Wearable Triboelectric Patch," *Nano Energy* 62 (2019): 355–366, https://doi.org/10.1016/j.nanoen.2019.05.033.

80. X. Guo, Z. Sun, Y. Zhu, and C. Lee, "Zero-Biased Bionic Fingertip E-Skin with Multimodal Tactile Perception and Artificial Intelligence for Augmented Touch Awareness," *Advanced Materials* 36 (2024), https://doi.org/10.1002/adma.202406778.

81. Y. Xu, Z. Sun, Z. Bai, et al., "Bionic E-skin with Precise Multidirectional Droplet Sliding Sensing for Enhanced Robotic Perception," *Nature Communications* 15, no. 1 (2024): 6022, https://doi.org/10.1038/s41467-024-50270-8.

82. X. Gao, X. Chen, M. Lin, et al., "A Wearable Echomyography System Based on a Single Transducer," *Nature Electronics* 7, no. 11 (2024): 1035–1046, https://doi.org/10.1038/s41928-024-01271-4.

83. M. Zhu, Q. Shi, T. He, et al., "Self-Powered and Self-Functional Cotton Sock Using Piezoelectric and Triboelectric Hybrid Mechanism for Healthcare and Sports Monitoring," *ACS Nano* 13, no. 2 (2019): 1940–1952, https://doi.org/10.1021/acsnano.8b08329.

84. D. Hohm and R. Gerhard-Multhaupt, "Silicon-dioxide Electret Transducer," *The Journal of the Acoustical Society of America* 75, no. 4 (1984): 1297–1298, https://doi.org/10.1121/1.390738.

85. C.-K. Lim, "Enhancing Sensing Performance of Capacitive Sensors Using Kirigami Structures," *Sensors* 24, no. 21 (2024): 6930, https://doi.org/10.3390/s24216930.

86. Z. Li, L. Dong, H. Li, J. Zhang, X. Wang, and H. Zhang, "An Analog Readout Circuit with a Noise-Reduction Input Buffer for MEMS Microphone," *IEEE Transactions on Circuits and Systems II Express Briefs* 69, no. 10 (2022): 3983–3987, https://doi.org/10.1109/TCSII.2022.3186205.

87. S. Qiao, Y. He, H. Sun, et al., "Ultra-highly Sensitive Dual Gases Detection Based on Photoacoustic Spectroscopy by Exploiting a Long-wave, High-power, Wide-tunable, Single-longitudinal-mode Solid-state Laser," *Light: Science & Applications* 13, no. 1 (2024): 100, https://doi.org/10.1038/s41377-024-01459-5.

88. H. C. Her, T. L. Wu, and J. H. Huang, "Acoustic Analysis and Fabrication of Microelectromechanical System Capacitive Microphones," *Journal of Applied Physics* 104, no. 8 (2008): 084509, https://doi.org/10.1063/1.3000038.

89. Z. You, J. Gan, C. Yang, R. Tuerhong, L. Zhao, and Y. Lu, "Piezoelectric MEMS Microphones Based on Rib Structures and Single Crystal PZT Thin Film," *Microsystems & Nanoengineering* 10, no. 1 (2024): 167, https://doi.org/10.1038/s41378-024-00767-5.

90. Y. Guan, S. Sadeghpour, C. Wang, et al., "A Hybrid MEMS Microphone Combining Piezoelectric and Capacitive Transduction Mechanisms," *Journal of Microelectromechanical Systems* 34, no. 3 (2025): 306–315, https://doi.org/10.1109/JMEMS.2025.3548927.

91. A. Rahaman and B. Kim, "Sound Source Localization by Ormia ochracea Inspired Low–noise Piezoelectric MEMS Directional Microphone," *Scientific Reports* 10, no. 1 (2020): 1–10, https://doi.org/10.1038/s41598-020-66489-6.

92. K. Chen, B. Zhang, M. Guo, et al., "Photoacoustic Trace Gas Detection of Ethylene in High-concentration Methane Background Based on Dual Light Sources and fiber-optic Microphone," *Sensors and Actuators B: Chemical* 310 (2020): 127825, https://doi.org/10.1016/j.snb.2020.127825.

93. Z. Wang, Y. Zhang, X. Huang, et al., "Miniature Mid-infrared Photoacoustic Gas Sensor for Detecting Dissolved Carbon Dioxide in Seawater," *Sensors and Actuators B: Chemical* 405 (2024): 135370, https://doi.org/10.1016/j.snb.2024.135370.

94. C. Li, F. Ma, C. Sun, et al., "In-situ Detection of Dissolved C_2H_2/CH_4 with Frequency-division-multiplexed fiber-optic Photoacoustic Sensor," *Sensors Actuators B Chem* 435 (2025): 137651, https://doi.org/10.1016/j.snb.2025.137651.

95. R. Lu and S. Gong, "RF Acoustic Microsystems Based on Suspended Lithium Niobate Thin Films: Advances and Outlook," *Journal of Micromechanics and Microengineering* 31, no. 11 (2021): 114001, https://doi.org/10.1088/1361-6439/ac288f.

96. X. Niu, V. Chulukhadze, Z. Liu, et al., "Lithium Niobate Microphone with High SNR Potential," *IEEE Sensors Journal* 25, no. 10 (2025): 18115–18122, https://doi.org/10.1109/JSEN.2025.3555885.

97. G. Piazza, V. Felmetsger, P. Muralt, R. H. Olsson, and R. Ruby, "Piezoelectric Aluminum Nitride Thin Fi Lms for Microelectromechanical Systems," *MRS Bulletin* 37, no. 11 (2012): 1051–1061, https://doi.org/10.1557/mrs.2012.268.

98. R. Weigel, D. P. Morgan, J. M. Owens, et al., "Microwave Acoustic Materials, Devices, and Applications," *IEEE Transactions on Microwave Theory and Techniques* 50, no. 3 (2002): 738–749, https://doi.org/10.1109/22.989958.

99. R. C. Turner, P. A. Fuierer, R. E. Newnham, and T. R. Shrout, "Materials for High Temperature Acoustic and Vibration Sensors: A

Review," *Applied Acoustics* 41, no. 4 (1994): 299–324, https://doi.org/10.1016/0003-682X(94)90091-4.

100. H. L. Wang, E. M. You, R. Panneerselvam, S. Y. Ding, and Z. Q. Tian, "Advances of Surface-enhanced Raman and IR Spectroscopies: From Nano/Microstructures to Macro-optical Design," *Light: Science & Applications* 10, no. 1 (2021): 161, https://doi.org/10.1038/s41377-021-00599-2.

101. A. Toma, S. Tuccio, M. Prato, et al., "Squeezing Terahertz Light into Nanovolumes: Nanoantenna Enhanced Terahertz Spectroscopy (NETS) of Semiconductor Quantum Dots," *Nano Letters* 15, no. 1 (2015): 386–391, https://doi.org/10.1021/nl503705w.

102. C. D'Andrea, J. Bochterle, A. Toma, et al., "Optical Nanoantennas for Multiband Surface-enhanced Infrared and Raman Spectroscopy," *ACS Nano* 7, no. 4 (2013): 3522–3531, https://doi.org/10.1021/nn4004764.

103. D. Rodrigo, A. Tittl, N. Ait-Bouziad, et al., "Resolving Molecule-specific Information in Dynamic Lipid Membrane Processes with Multi-resonant Infrared Metasurfaces," *Nature Communications* 9, no. 1 (2018): 2160, https://doi.org/10.1038/s41467-018-04594-x.

104. H. Zhou, D. Li, Z. Ren, X. Mu, and C. Lee, "Loss-Induced Phase Transition in Mid-Infrared Plasmonic Metamaterials for Ultrasensitive Vibrational Spectroscopy," *InfoMat* 4, no. 12 (2022): 12349, https://doi.org/10.1002/inf2.12349.

105. C. Xu, Z. Ren, H. Zhou, et al., "Expanding Chiral Metamaterials for Retrieving Fingerprints via Vibrational Circular Dichroism," *Light: Science & Applications* 12, no. 1 (2023): 154, https://doi.org/10.1038/s41377-023-01186-3.

106. H. Zhou, D. Li, Z. Ren, C. Xu, L. F. Wang, and C. Lee, "Surface Plasmons-phonons for Mid-infrared Hyperspectral Imaging," *Science Advances* 10, no. 22 (2024): ado3179, https://doi.org/10.1126/sciadv.ado3179.

107. F. U. Richter, I. Sinev, S. Zhou, et al., "Gradient High- Q Dielectric Metasurfaces for Broadband Sensing and Control of Vibrational Light-Matter Coupling," *Advanced Materials* 36, no. 25 (2024): 2314279, https://doi.org/10.1002/adma.202314279.

108. K. Yang, J. Wang, X. Yao, et al., "Large-Area Plasmonic Metamaterial with Thickness-Dependent Absorption," *Advanced Optical Materials* 9, no. 1 (2021): 2001375, https://doi.org/10.1002/adom.202001375.

109. C. F. Shi, Z. Q. Li, C. Wang, J. Li, and X. H. Xia, "Ultrasensitive Plasmon Enhanced Raman Scattering Detection of Nucleolin Using Nanochannels of 3D Hybrid Plasmonic Metamaterial," *Biosensors and Bioelectronics* 178, no. 2020 (2021): 113040, https://doi.org/10.1016/j.bios.2021.113040.

110. H. Hu, A. K. Pal, A. Berestennikov, et al., "Surface-Enhanced Raman Scattering in BIC-Driven Semiconductor Metasurfaces," *Advanced Optical Materials* 12, no. 14 (2024): 2302812, https://doi.org/10.1002/adom.202302812.

111. A. Tittl, A. Leitis, M. Liu, et al., "Imaging-based Molecular Barcoding with Pixelated Dielectric Metasurfaces," *Science (80-)* 360, no. 6393 (2018): 1105–1109, https://doi.org/10.1126/science.aas9768.

112. A. Leitis, A. Tittl, M. Liu, et al., "Angle-multiplexed All-dielectric Metasurfaces for Broadband Molecular Fingerprint Retrieval," *Science Advances* 5, no. 5 (2019): aaw2871, https://doi.org/10.1126/sciadv.aaw2871.

113. M. L. Tseng, Y. Jahani, A. Leitis, and H. Altug, "Dielectric Metasurfaces Enabling Advanced Optical Biosensors," *ACS Photonics* 8, no. 1 (2021): 47–60, https://doi.org/10.1021/acsphotonics.0c01030.

114. J. Langer, D. Jimenez de Aberasturi, J. Aizpurua, et al., "Present and Future of Surface-enhanced Raman Scattering," *ACS Nano* 14, no. 1 (2020): 28–117, https://doi.org/10.1021/acsnano.9b04224.

115. H. T. Lee, J. Kim, J. S. Lee, M. Yoon, and H. R. Park, "More than 30000-fold Field Enhancement of Terahertz Nanoresonators Enabled by Rapid Inverse Design," *Nano Letters* 23, no. 24 (2023): 11685–11692, https://doi.org/10.1021/acs.nanolett.3c03572.

116. D. Li, H. Zhou, Z. Ren, and C. Lee, "Advances in MEMS, Optical MEMS, and Nanophotonics Technologies for Volatile Organic Compound Detection and Applications," *Small Science* 5, no. 4 (2025): 2400250, https://doi.org/10.1002/smsc.202400250.

117. Y. Chang, J. Wei, and C. Lee, "Metamaterials – From Fundamentals and MEMS Tuning Mechanisms to Applications," *Nanophotonics* 9, no. 10 (2020): 3049–3070, https://doi.org/10.1515/nanoph-2020-0045.

118. P. Pitchappa, A. Kumar, R. Singh, and N. Wang, "Electromechanically Tunable Frequency-Agile Metamaterial Bandpass Filters for Terahertz Waves," *Advanced Optical Materials* 10, no. 2 (2022), https://doi.org/10.1002/adom.202101544.

119. G. Jiang, Y. Wang, Z. Zhang, et al., "Abnormal Beam Steering with Kirigami Reconfigurable Metasurfaces," *Nature Communications* 16, no. 1 (2025): 1660, https://doi.org/10.1038/s41467-025-56211-3.

120. O. Niksan, L. Bi, Y. Gogotsi, and M. H. Zarifi, "MXene-based Kirigami Designs: Showcasing Reconfigurable Frequency Selectivity in Microwave Regime," *Nature Communications* 15, no. 1 (2024): 7793, https://doi.org/10.1038/s41467-024-51853-1.

121. H. Wang, Z. Wang, C. Gong, et al., "Using Light to Image Millimeter Wave Based on Stacked Meta-MEMS Chip," *Light: Science & Applications* 14, no. 1 (2025): 59, https://doi.org/10.1038/s41377-024-01733-6.

122. M. Manjappa, P. Pitchappa, N. Singh, et al., "Reconfigurable MEMS Fano Metasurfaces with Multiple-input–output States for Logic Operations at Terahertz Frequencies," *Nature Communications* 9, no. 1 (2018): 4056, https://doi.org/10.1038/s41467-018-06360-5.

123. H. Zhou, T.-Y. Chen, and Z. Ren, "Mems-Driven Electrically Reconfigurable Platform for Photonic Quasi-Bound States in the Continuum," in International Conference on Solid State Sensors and Actuators (Transducers) (2025), 108–111.

124. C. Meng, P. C. V. Thrane, F. Ding, et al., "Dynamic Piezoelectric MEMS-based Optical Metasurfaces," *Science Advances* 7, no. 26 (Jun. 2021): abg5639, https://doi.org/10.1126/sciadv.abg5639.

125. S. Doshi, A. Ji, A. I. Mahdi, et al., "Electrochemically Mutable Soft Metasurfaces," *Nature Materials* 24, no. 2 (2025): 205–211, https://doi.org/10.1038/s41563-024-02042-4.

126. M. Manjappa, P. Pitchappa, N. Wang, C. Lee, and R. Singh, "Active Control of Resonant Cloaking in a Terahertz MEMS Metamaterial," *Advanced Optical Materials* 6, no. 16 (2018): 1800141, https://doi.org/10.1002/adom.201800141.

127. L. Cong, P. Pitchappa, C. Lee, and R. Singh, "Active Phase Transition via Loss Engineering in a Terahertz MEMS Metamaterial," *Advanced Materials* 29, no. 26 (2017): 1700733, https://doi.org/10.1002/adma.201700733.

128. C. P. Ho, P. Pitchappa, and C. Lee, "Digitally Reconfigurable Binary Coded Terahertz Metamaterial with Output Analogous to NOR and and," *Journal of Applied Physics* 119, no. 15 (2016): 153104, https://doi.org/10.1063/1.4946891.

129. P. Pitchappa, M. Manjappa, C. P. Ho, R. Singh, N. Singh, and C. Lee, "Active Control of Electromagnetically Induced Transparency Analog in Terahertz MEMS Metamaterial," *Advanced Optical Materials* 4, no. 4 (2016): 541–547, https://doi.org/10.1002/adom.201500676.

130. P. Pitchappa, C. P. Ho, L. Cong, R. Singh, N. Singh, and C. Lee, "Reconfigurable Digital Metamaterial for Dynamic Switching of Terahertz Anisotropy," *Advanced Optical Materials* 4, no. 3 (2016): 391–398, https://doi.org/10.1002/adom.201500588.

131. P. Pitchappa, C. P. Ho, L. Dhakar, and C. Lee, "Microelectromechanically Reconfigurable Interpixelated Metamaterial for Independent Tuning of Multiple Resonances at Terahertz Spectral Region," *Optica* 2, no. 6 (2015): 571, https://doi.org/10.1364/optica.2.000571.

132. P. Pitchappa, C. P. Ho, L. Dhakar, Y. Qian, N. Singh, and C. Lee, "Periodic Array of Subwavelength MEMS Cantilevers for Dynamic Manipulation of Terahertz Waves," *Journal of Microelectromechanical*

Systems 24, no. 3 (2015): 525–527, https://doi.org/10.1109/JMEMS.2015.2421307.

133. Y. S. Lin, C. Y. Huang, and C. Lee, "Reconfiguration of Resonance Characteristics for Terahertz U-Shape Metamaterial Using MEMS Mechanism," *Ieee Journal of Selected Topics in Quantum Electronics* 21, no. 4 (2015): 93–99, https://doi.org/10.1109/JSTQE.2014.2361840.

134. P. Pitchappa, C. P. Ho, P. Kropelnicki, N. Singh, D. L. Kwong, and C. Lee, "Micro-electro-mechanically Switchable near Infrared Complementary Metamaterial Absorber," *Applied Physics Letters* 104, no. 20 (2014): 201114, https://doi.org/10.1063/1.4879284.

135. P. Pitchappa, C. Pei Ho, Y.-S. Lin, et al., "Micro-electro-mechanically Tunable Metamaterial with Enhanced Electro-optic Performance," *Applied Physics Letters* 104, no. 15 (2014): 151104, https://doi.org/10.1063/1.4871517.

136. V. S. Lin and C. Lee, "Tuning Characteristics of Mirrorlike T-shape Terahertz Metamaterial Using out-of-plane Actuated Cantilevers," *Applied Physics Letters* 104, no. 25 (2014): 251914, https://doi.org/10.1063/1.4885839.

137. F. Ma, Y. S. Lin, X. Zhang, and C. Lee, "Tunable Multiband Terahertz Metamaterials Using a Reconfigurable Electric Split-ring Resonator Array," *Light: Science & Applications* 3 (2014): e171–e171, https://doi.org/10.1038/lsa.2014.52.

138. Y. S. Lin, Y. Qian, F. Ma, Z. Liu, P. Kropelnicki, and C. Lee, "Development of Stress-induced Curved Actuators for a Tunable THz Filter Based on Double Split-ring Resonators," *Applied Physics Letters* 102, no. 11 (2013): 111908, https://doi.org/10.1063/1.4798244.

139. F. Ma, Y. Qian, Y.-S. Lin, et al., "Polarization-sensitive Microelectromechanical Systems Based Tunable Terahertz Metamaterials Using Three Dimensional Electric Split-ring Resonator Arrays," *Applied Physics Letters* 102, no. 16 (2013): 161912, https://doi.org/10.1063/1.4803048.

140. P. Pitchappa, M. Manjappa, H. N. S. Krishnamoorthy, Y. Chang, C. Lee, and R. Singh, "Bidirectional Reconfiguration and Thermal Tuning of Microcantilever Metamaterial Device Operating from 77 K to 400 K," *Applied Physics Letters* 111, no. 26 (2017): 261101, https://doi.org/10.1063/1.5006836.

141. K. Shih, P. Pitchappa, M. Manjappa, et al., "Active MEMS Metamaterials for THz Bandwidth Control," *Applied Physics Letters* 110, no. 16 (2017): 161108, https://doi.org/10.1063/1.4980115.

142. C. P. Ho, P. Pitchappa, Y. S. Lin, C. Y. Huang, P. Kropelnicki, and C. Lee, "Electrothermally Actuated Microelectromechanical Systems Based Omega-ring Terahertz Metamaterial with Polarization Dependent Characteristics," *Applied Physics Letters* 104, no. 16 (Apr. 2014): 161104, https://doi.org/10.1063/1.4871999.

143. X. Liu and W. J. Padilla, "Reconfigurable Room Temperature Metamaterial Infrared Emitter," *Optica* 4, no. 4 (Apr. 2017): 430, https://doi.org/10.1364/optica.4.000430.

144. E. Arbabi, A. Arbabi, S. M. Kamali, Y. Horie, M. S. Faraji-Dana, and A. Faraon, "MEMS-tunable Dielectric Metasurface Lens," *Nature Communications* 9, no. 1 (Feb. 2018): 812, https://doi.org/10.1038/s41467-018-03155-6.

145. J. Zhou, X. Liu, H. Zhou, et al., "Artificial-Intelligence-Enhanced Mid-Infrared Lab-on-a-Chip for Mixture Spectroscopy Analysis," *Laser & Photonics Reviews* 19, no. 1 (Aug. 2025): 2400754, https://doi.org/10.1002/lpor.202400754.

146. N. Qi, Q. Ma, A. Li, et al., "A Monolithically Integrated DWDM Si-Photonics Transceiver for Chiplet Optical I/O," *Ieee Journal of Solid-State Circuits* 60 (2025): 3613–3625, https://doi.org/10.1109/JSSC.2025.3585584.

147. M. Dong, G. Clark, A. J. Leenheer, et al., "High-speed Programmable Photonic Circuits in a Cryogenically Compatible, Visible–near-infrared 200 Mm CMOS Architecture," *Nature Photonics* 16, no. 1 (2022): 59–65, https://doi.org/10.1038/s41566-021-00903-x.

148. B. Malayappan, U. P. Lakshmi, B. V. V. S. N. P. Rao, K. Ramaswamy, and P. K. Pattnaik, "Sensing Techniques and Interrogation Methods in Optical MEMS Accelerometers: A Review," *IEEE Sensors Journal* 22, no. 7 (2022): 6232–6246, https://doi.org/10.1109/JSEN.2022.3149662.

149. Y. Wu, X. Zeng, Y. J. Rao, Y. Gong, C. L. Hou, and G. G. Yang, "MOEMS Accelerometer Based on Microfiber Knot Resonator," *IEEE Photonics Technology Letters* 21, no. 20 (2009): 1547–1549, https://doi.org/10.1109/LPT.2009.2029556.

150. J. Hu, H. Xu, N. Hu, and H. Hu, "Optical Mems Accelerometer Based on Photonic Crystal with Air Defect Layer," in Proceedings of the 2024 Symposium on Piezoelectricity, Acoustic Waves, and Device Applications, SPAWDA (2024), 553–557, https://doi.org/10.1109/SPAWDA63926.2024.10878862.

151. A. K. N. Shotorban, K. Jafari, and K. Abedi, "Optical MEMS Accelerometer Sensor Relying on a Micro-Ring Resonator and an Elliptical Disk," *IET Circuits, Devices & Systems* 13, no. 7 (2019): 1102–1106, https://doi.org/10.1049/iet-cds.2019.0029.

152. N. De Milleri, G. A. Onaran, A. Wiesbauer, and A. Baschirotto, "Design of a MEMS Optical Microphone Transducer Based on Light Phase Modulation," *IEEE Sensors Journal* 24, no. 3 (2024): 3628–3636, https://doi.org/10.1109/JSEN.2023.3339546.

153. P. H. Kim, B. D. Hauer, T. J. Clark, F. Fani Sani, M. R. Freeman, and J. P. Davis, "Magnetic Actuation and Feedback Cooling of a Cavity Optomechanical Torque Sensor," *Nature Communications* 8, no. 1 (2017): 1355, https://doi.org/10.1038/s41467-017-01380-z.

154. B. S. Tina, S. Rohith, and V. Seena, "Fabrication and Electromechanical Characterization of Silicon Nanomechanical Membrane Flexure MEMS Sensor for Gas Sensing Applications," *IEEE Sensors Journal* 24, no. 5 (2024): 5440–5447, https://doi.org/10.1109/JSEN.2024.3351198.

155. Q. Qiao, X. Liu, Z. Ren, et al., "MEMS-Enabled on-Chip Computational Mid-Infrared Spectrometer Using Silicon Photonics," *ACS Photonics* 9, no. 7 (2022): 2367–2377, https://doi.org/10.1021/acsphotonics.2c00381.

156. Y. Chang, S. Xu, B. Dong, et al., "Development of Triboelectric-enabled Tunable Fabry-Pérot Photonic-crystal-slab Filter towards Wearable Mid-infrared Computational Spectrometer," *Nano Energy* 89 (2021): 106446, https://doi.org/10.1016/j.nanoen.2021.106446.

157. X. Zhao, J. M. Tsai, H. Cai, et al., "A Nano-opto-mechanical Pressure Sensor via Ring Resonator," *Optics Express* 20, no. 8 (2012): 8535, https://doi.org/10.1364/oe.20.008535.

158. E. Sentre-Arribas, A. Aparicio-Millán, A. Lemaître, et al., "Simultaneous Optical and Mechanical Sensing Based on Optomechanical Resonators," *ACS Sensors* 9, no. 1 (2024): 371–378, https://doi.org/10.1021/acssensors.3c02103.

159. T. W. Lu, Z. Y. Wang, K. M. Lin, and P. T. Lee, "Lasing Emission from Soft Photonic Crystals for Pressure and Position Sensing," *Nanomaterials* 13, no. 22 (2023): 2956, https://doi.org/10.3390/nano13222956.

160. D. Y. Fedyanin and Y. V. Stebunov, "All-nanophotonic NEMS Biosensor on a Chip," *Scientific Reports* 5 (2015), https://doi.org/10.1038/srep10968.

161. Y. Yan, H. Feng, C. Wang, and W. Ren, "On-chip Photothermal Gas Sensor Based on a Lithium Niobate Rib Waveguide," *Sensors and Actuators B: Chemical* 405 (2024): 135392, https://doi.org/10.1016/j.snb.2024.135392.

162. H. Chen, H. Zhang, J. Zhou, et al., "High-performance and Wavelength-transplantable on-chip Fourier Transform Spectrometer Using MEMS in-plane Reconfiguration," *Photonics Research* 12, no. 8 (2024): 1730, https://doi.org/10.1364/prj.521439.

163. P. Saha and M. Sen, "NOEMS Based Slotted Photonic Crystal Cavity for the Sensing of Force," *IEEE Transactions on Nanotechnology* 20 (2021): 20–27, https://doi.org/10.1109/TNANO.2020.3042923.

164. T. W. Lu, C. C. Wu, and P. T. Lee, "1D photonic Crystal Strain Sensors," *ACS Photonics* 5, no. 7 (2018): 2767–2772, https://doi.org/10.1021/acsphotonics.8b00560.

165. Z. Brodzeli, L. Silvestri, A. Michie, et al., "Sensors at Your Fibre Tips: A Novel Liquid Crystal-based Photonic Transducer for Sensing Systems," *Journal of Lightwave Technology* 31, no. 17 (2013): 2940–2946, https://doi.org/10.1109/JLT.2013.2274455.

166. S. Liu, P. Chen, J. Luo, et al., "Nano-Optomechanical Resonators Based Graphene/Au Membrane for Current Sensing," *Journal of Lightwave Technology* 40, no. 21 (2022): 7200–7207, https://doi.org/10.1109/JLT.2022.3198116.

167. Q. Qiao, J. Xia, C. Lee, and G. Zhou, "Applications of Photonic Crystal Nanobeam Cavities for Sensing," *Micromachines* 9, no. 11 (2018): 541, https://doi.org/10.3390/mi9110541.

168. A. Buzzin, R. Asquini, D. Caputo, and G. de Cesare, "Sensitive and Compact Evanescent-Waveguide Optical Detector for Sugar Sensing in Commercial Beverages," *Sensors* 23, no. 19 (2023): 8184, https://doi.org/10.3390/s23198184.

169. I. Zeimpekis, I. Sari, and M. Kraft, "Characterization of a Mechanical Motion Amplifier Applied to a MEMS Accelerometer," *Journal of Microelectromechanical Systems* 21, no. 5 (2012): 1032–1042, https://doi.org/10.1109/JMEMS.2012.2196491.

170. D. Li, H. Zhou, Z. Ren, C. Xu, and C. Lee, "Tailoring Light–Matter Interactions in Overcoupled Resonator for Biomolecule Recognition and Detection," *Nano-Micro Letters* 17, no. 1 (2025): 10, https://doi.org/10.1007/s40820-024-01520-3.

171. X. Liu, Z. Zhang, J. Zhou, W. Liu, G. Zhou, and C. Lee, "Artificial Intelligence-Enhanced Waveguide "Photonic Nose"- Augmented Sensing Platform for VOC Gases in Mid-Infrared," *Small* 20, no. 34 (2024): 2400035, https://doi.org/10.1002/smll.202400035.

172. H. Zhou, Z. Ren, C. Xu, L. Xu, and C. Lee, "MOF/Polymer-Integrated Multi-Hotspot Mid-Infrared Nanoantennas for Sensitive Detection of CO2 Gas," *Nano-Micro Letters* 14, no. 1 (2022): 207, https://doi.org/10.1007/s40820-022-00950-1.

173. Z. Ren, Z. Zhang, J. Wei, B. Dong, and C. Lee, "Wavelength-multiplexed Hook Nanoantennas for Machine Learning Enabled Mid-infrared Spectroscopy," *Nature Communications* 13, no. 1 (2022): 3859, https://doi.org/10.1038/s41467-022-31520-z.

174. C. Xu, Z. Ren, H. Zhou, J. Zhou, D. Li, and C. Lee, "Near-Field Coupling Induced Less Chiral Responses in Chiral Metamaterials for Surface-Enhanced Vibrational Circular Dichroism," *Advanced Functional Materials* 34, no. 13 (2024), https://doi.org/10.1002/adfm.202314482.

175. H. Liu, X. She, H. Shen, et al., "Monolithic Integrated Cavity Optomechanical Accelerometer Based on Push-pull Photonic Crystal Zipper Cavity," *Optical Engineering* 62, no. 03 (2023), https://doi.org/10.1117/1.oe.62.3.037107.

176. J. Kappa, D. Sokoluk, S. Klingel, C. Shemelya, E. Oesterschulze, and M. Rahm, "Electrically Reconfigurable Micromirror Array for Direct Spatial Light Modulation of Terahertz Waves over a Bandwidth Wider than 1 THz," *Scientific Reports* 9, no. 1 (2019): 2597, https://doi.org/10.1038/s41598-019-39152-y.

177. J. Suh, K. Han, C. W. Peterson, and G. Bahl, "Invited Article: Real-time Sensing of Flowing Nanoparticles with Electro-opto-mechanics," *APL Photonics* 2, no. 1 (2017): 010801, https://doi.org/10.1063/1.4972299.

178. H. Kaviani, R. Ghobadi, B. Behera, et al., "Optomechanical Detection of Light with Orbital Angular Momentum," *Optics Express* 28, no. 10 (2020): 15482, https://doi.org/10.1364/oe.389170.

179. R. Wang, R. Hao, D. Li, et al., "Multifunctional Terahertz Biodetection Enabled by Resonant Metasurfaces," *Advanced Materials* 37, no. 16 (2025): 2418147, https://doi.org/10.1002/adma.202418147.

180. C. Zhang, L. Xu, X. Miao, et al., "Machine Learning Assisted Dual-modal SERS Detection for Circulating Tumor Cells," *Biosensors and Bioelectronics* 268 (2025): 116897, https://doi.org/10.1016/j.bios.2024.116897.

181. Y. Wan, Q. Wei, H. Sun, et al., "Machine Learning Assisted Biomimetic Flexible SERS Sensor from Seashells for Pesticide Classification and Concentration Prediction," *Chemical Engineering Journal* 507 (2025): 160813, https://doi.org/10.1016/j.cej.2025.160813.

182. S. Basiri-Esfahani, A. Armin, S. Forstner, and W. P. Bowen, "Precision Ultrasound Sensing on a Chip," *Nature Communications* 10, no. 1 (2019): 132, https://doi.org/10.1038/s41467-018-08038-4.

183. P. Zhang, H. Deng, X. Jiang, Y. Tang, L. Yuan, and C. Wang, "A Vector Accelerometer Based on Optical Fiber Cantilever with Hybrid Gratings," *Journal of Lightwave Technology* 42, no. 19 (2024): 7021–7027, https://doi.org/10.1109/JLT.2024.3415153.

184. M. Sansa, M. Defoort, A. Brenac, et al., "Optomechanical Mass Spectrometry," *Nature Communications* 11, no. 1 (2020): 3781, https://doi.org/10.1038/s41467-020-17592-9.

185. B. Li, F. L. Hsiao, and C. Lee, "Configuration Analysis of Sensing Element for Photonic Crystal Based NEMS Cantilever Using Dual Nano-ring Resonator," *Sensors and Actuators A: Physical* 169, no. 2 (2011): 352–361, https://doi.org/10.1016/j.sna.2011.03.020.

186. A. G. Krause, M. Winger, T. D. Blasius, Q. Lin, and O. Painter, "A High-resolution Microchip Optomechanical Accelerometer," *Nature Photonics* 6, no. 11 (2012): 768–772, https://doi.org/10.1038/nphoton.2012.245.

187. F. Galeotti, I. Sersic Vollenbroek, M. Petruzzella, et al., "On-chip Waveguide-coupled Opto-electro-mechanical System for Nanoscale Displacement Sensing," *APL Photonics* 5, no. 2 (2020): 026103, https://doi.org/10.1063/1.5131576.

188. Y. Tao, W. Liu, C. Nan, et al., "Resonant fiber Optic Gyroscope Based on Sideband Locking of Dual-light Sources," *Optical Engineering* 63, no. 04 (2024), https://doi.org/10.1117/1.oe.63.4.044104.

189. Y. S. Yaras, D. K. Yildirim, O. Kocaturk, and F. L. Degertekin, "Sensitivity and Phase Response of FBG Based Acousto-optic Sensors for Real-time MRI Applications," *OSA Continuum* 3, no. 3 (2020): 447, https://doi.org/10.1364/osac.385969.

190. Y. Wu, T. Sun, M. Shao, et al., "Pyroelectrically Driven Charge Transfer and Its Advantages on SERS and Self-Cleaning Property," *Laser & Photonics Reviews* 19, no. 4 (2025): 2401152, https://doi.org/10.1002/lpor.202401152.

191. M. R. Watts, M. J. Shaw, and G. N. Nielson, "Microphotonic Thermal Imaging," *Nature Photonics* 1, no. 11 (2007): 632–634, https://doi.org/10.1038/nphoton.2007.219.

192. M. W. Pruessner, D. Park, T. H. Stievater, D. A. Kozak, and W. S. Rabinovich, "Optomechanical Cavities for All-Optical Photothermal Sensing," *ACS Photonics* 5, no. 8 (2018): 3214–3221, https://doi.org/10.1021/acsphotonics.8b00452.

193. T. J. Seok, K. Kwon, J. Henriksson, J. Luo, and M. C. Wu, "Wafer-scale Silicon Photonic Switches beyond Die Size Limit," *Optica* 6, no. 4 (2019): 490, https://doi.org/10.1364/optica.6.000490.

194. J. Roels, I. De Vlaminck, L. Lagae, B. Maes, D. Van Thourhout, and R. Baets, "Tunable Optical Forces between Nanophotonic Waveguides," *Nature Nanotechnology* 4, no. 8 (2009): 510–513, https://doi.org/10.1038/nnano.2009.186.

195. R. T. Paschoalin, N. O. Gomes, G. F. Almeida, et al., "Wearable Sensors Made with Solution-blow Spinning Poly(lactic acid) for Non-enzymatic Pesticide Detection in Agriculture and Food Safety," *Biosensors & Bioelectronics* 199, no. 2021 (2022): 113875, https://doi.org/10.1016/j.bios.2021.113875.

196. S. Xu, Z. Ren, B. Dong, J. Zhou, W. Liu, and C. Lee, "Mid-Infrared Silicon-on-Lithium-Niobate Electro-Optic Modulators toward Integrated Spectroscopic Sensing Systems," *Advanced Optical Materials* 11, no. 4 (2023): 2202228, https://doi.org/10.1002/adom.202202228.

197. H. Sun, Q. Qiao, C. Lee, and G. Zhou, "MEMS-Enabled Ultralow Power Consumption Programmable Arbitrary Order Mode Switch," *Laser & Photonics Reviews* 19, no. 1 (2025): 2400641, https://doi.org/10.1002/lpor.202400641.

198. H. Sun, Q. Qiao, J. Xia, C. Lee, and G. Zhou, "Mid-infrared Silicon Photonic Phase Shifter Based on Microelectromechanical System," *Optics Letters* 47, no. 22 (2022): 5801, https://doi.org/10.1364/ol.474597.

199. Y. Cui, V. A. Tamma, J. B. Lee, and W. Park, "Mechanically Tunable Negative-index Photonic Crystal Lens," *IEEE Photonics Journal* 2, no. 6 (2010): 1003–1012, https://doi.org/10.1109/JPHOT.2010.2091116.

200. W. Xue, Y. Liu, X. Zhu, et al., "A High-performance 10 Mm Diameter MEMS Fast Steering Mirror with Integrated Piezoresistive Angle Sensors for Laser Inter-satellite Links," *Microsystems & Nanoengineering* 11, no. 1 (2025): 75, https://doi.org/10.1038/s41378-025-00935-1.

201. L. Wu and Y. S. Lin, "Design and Investigation of Dual-axis Electrostatic Driving MEMS Scanning Micromirror," *International Journal of Optomechatronics* 18, no. 1 (2024): 2350749, https://doi.org/10.1080/15599612.2024.2350749.

202. K. E. Grutter, M. I. Davanço, K. C. Balram, and K. Srinivasan, "Invited Article: Tuning and Stabilization of Optomechanical Crystal Cavities through NEMS Integration," *APL Photonics* 3, no. 10 (2018), https://doi.org/10.1063/1.5042225.

203. M. J. Weaver, P. Duivestein, A. C. Bernasconi, et al., "An Integrated Microwave-to-optics Interface for Scalable Quantum Computing," *Nature Nanotechnology* 19, no. 2 (2024): 166–172, https://doi.org/10.1038/s41565-023-01515-y.

204. T. C. van Thiel, M. J. Weaver, F. Berto, et al., "Optical Readout of a Superconducting Qubit Using a Piezo-optomechanical Transducer," *Nature Physics* 21, no. 3 (2025): 401–405, https://doi.org/10.1038/s41567-024-02742-3.

205. T. J. Seok, N. Quack, S. Han, R. S. Muller, and M. C. Wu, "Large-scale Broadband Digital Silicon Photonic Switches with Vertical Adiabatic Couplers," *Optica* 3, no. 1 (2016): 64, https://doi.org/10.1364/optica.3.000064.

206. C. Haffner, A. Joerg, M. Doderer, et al., "Nano–opto-electro-mechanical Switches Operated at CMOS-level Voltages," *Science (80-)* 366, no. 6467 (2019): 860–864, https://doi.org/10.1126/science.aay8645.

207. W. Liu, S. Xu, and C. Lee, "Ultracompact on-chip Spectral Shaping Using Pixelated Nano-opto-electro-mechanical Gratings," *Science (80-)* 389, no. 6762 (2025): 806–810, https://doi.org/10.1126/science.adu8492.

208. X. Feng, T. Wu, Z. Gao, et al., "Non-Hermitian Hybrid Silicon Photonic Switching," *Nature Photonics* 19, no. 3 (2025): 264–270, https://doi.org/10.1038/s41566-024-01579-9.

209. H. Zhong, J. Li, Y. He, et al., "Ultra-low-power Consumption Silicon Electro-optic Switch Based on Photonic Crystal Nanobeam Cavity," *NPJ Nanophotonics* 1, no. 1 (2024): 33, https://doi.org/10.1038/s44310-024-00032-7.

210. G. Yang, H. Wang, S. Mu, et al., "Unveiling the Pockels Coefficient of Ferroelectric Nitride ScAlN," *Nature Communications* 15, no. 1 (2024): 9538, https://doi.org/10.1038/s41467-024-53895-x.

211. B.-C. Pan, H.-X. Liu, and H.-C. Xu, "Ultra-compact Lithium Niobate Microcavity Electro-optic Modulator beyond 110 GHz," *Chip* 1, no. 4 (2022): 100029, https://doi.org/10.1016/j.chip.2022.100029.

212. X. Meng, C. Yuan, X. Cheng, et al., "Thin-Film Lithium Niobate Modulators with Ultra-High Modulation Efficiency," *Laser & Photonics Reviews* 19, no. 1 (2025): 2400809, https://doi.org/10.1002/lpor.202400809.

213. S. A. Tadesse, H. Li, Q. Liu, and M. Li, "Acousto-optic Modulation of a Photonic Crystal Nanocavity with Lamb Waves in Microwave K Band," *Applied Physics Letters* 107, no. 20 (2015): 201113, https://doi.org/10.1063/1.4935981.

214. H. Li, S. A. Tadesse, Q. Liu, and M. Li, "Nanophotonic Cavity Optomechanics with Propagating Acoustic Waves at Frequencies up to 12 GHz," *Optica* 2, no. 9 (2015): 826, https://doi.org/10.1364/optica.2.000826.

215. R. Nehra, R. Sekine, L. Ledezma, et al., "Few-cycle Vacuum Squeezing in Nanophotonics," *Science* 377, no. 6612 (2022): 1333–1337, https://doi.org/10.1126/science.abo6213.

216. Y. Lee, J. Karst, M. Ubl, M. Hentschel, and H. Giessen, "Dynamic Beam Control Based on Electrically Switchable Nanogratings from Conducting Polymers," *Nanophotonics* 12, no. 14 (2023): 2865–2871, https://doi.org/10.1515/nanoph-2022-0801.

217. C. L. Panuski, I. Christen, M. Minkov, et al., "A Full Degree-of-freedom Spatiotemporal Light Modulator," *Nature Photonics* 16, no. 12 (2022): 834–842, https://doi.org/10.1038/s41566-022-01086-9.

218. M. Mirhosseini, A. Sipahigil, M. Kalaee, and O. Painter, "Superconducting Qubit to Optical Photon Transduction," *Nature* 588, no. 7839 (2020): 599–603, https://doi.org/10.1038/s41586-020-3038-6.

219. S. Meesala, S. Wood, D. Lake, et al., "Non-classical Microwave–optical Photon Pair Generation with a Chip-scale Transducer," *Nature Physics* 20, no. 5 (2024): 871–877, https://doi.org/10.1038/s41567-024-02409-z.

220. S. A. Tadesse and M. Li, "Sub-optical Wavelength Acoustic Wave Modulation of Integrated Photonic Resonators at Microwave Frequencies," *Nature Communications* 5 (2014): 5402, https://doi.org/10.1038/ncomms6402.

221. W. Huang, L. Xia, J. Li, et al., "Acousto-Optic Modulation on Silicon-Aluminum Nitride Hybrid-Integrated Platform for Cryogenic Applications," *Nano Letters* 25, no. 13 (2025): 5117–5123, https://doi.org/10.1021/acs.nanolett.4c05680.

222. K. Ye, H. Feng, R. te Morsche, et al., "Integrated Brillouin Photonics in Thin-film Lithium Niobate," *Science Advances* 11, no. 18 (2025), https://doi.org/10.1126/sciadv.adv4022.

223. M. Eichenfield, J. Chan, R. M. Camacho, K. J. Vahala, and O. Painter, "Optomechanical Crystals," *Nature* 462, no. 7269 (2009): 78–82, https://doi.org/10.1038/nature08524.

224. R. Van Laer, B. Kuyken, D. Van Thourhout, and R. Baets, "Interaction between Light and Highly Confined Hypersound in a Silicon Photonic Nanowire," *Nature Photonics* 9, no. 3 (2015): 199–203, https://doi.org/10.1038/nphoton.2015.11.

225. D. Hui, D. Li, B. Wang, et al., "A MEMS Grating Modulator with a Tunable Sinusoidal Grating for Large-scale Extendable Apertures," *Microsystems & Nanoengineering* 11, no. 1 (2025): 39, https://doi.org/10.1038/s41378-025-00894-7.

226. H. Lee, S. Kim, S. Eom, et al., "Quantum Tunneling High-speed Nano-excitonic Modulator," *Nature Communications* 15, no. 1 (2024): 8725, https://doi.org/10.1038/s41467-024-52813-5.

227. Y. Wang, G. Zhou, X. Zhang, et al., "2D broadband Beamsteering with Large-scale MEMS Optical Phased Array," *Optica* 6, no. 5 (2019): 557, https://doi.org/10.1364/optica.6.000557.

228. R. Ma, Z. Huang, S. Gao, et al., "Ka-band Thin Film Lithium Niobate Photonic Integrated Optoelectronic Oscillator," *Photonics Research* 12, no. 6 (2024): 1283, https://doi.org/10.1364/prj.521301.

229. H. Lee, L. Chang, A. Kecebas, et al., "Chiral Exceptional Point Enhanced Active Tuning and Nonreciprocity in Micro-resonators," *Light: Science & Applications* 14, no. 1 (2025): 45, https://doi.org/10.1038/s41377-024-01686-w.

230. Y. Zhang, W. Zhu, P. Fan, et al., "A Broadband and Low-power Light-control-light Effect in a fiber-optic Nano-optomechanical System," *Nanoscale* 12, no. 17 (2020): 9800–9809, https://doi.org/10.1039/c9nr10953f.

231. M. Dong, D. Heim, A. Witte, et al., "Piezo-optomechanical Cantilever Modulators for VLSI Visible Photonics," *APL Photonics* 7, no. 5 (2022): 51304, https://doi.org/10.1063/5.0088424.

232. A. Ren, Y. Ding, H. Yang, et al., "A Tip-tilt-piston Electrothermal Micromirror Array with Integrated Position Sensors," *Microsystems &*

Nanoengineering 11, no. 1 (2025): 45, https://doi.org/10.1038/s41378-024-00835-w.

233. T. Liu, T. Pan, P. Wang, S. Qin, and H. Xie, "Scanning Optimization of an Electrothermally-actuated MEMS Mirror for Applications in Optical Coherence Tomography Endoscopy," *Sensors and Actuators A: Physical* 335 (2022): 113377, https://doi.org/10.1016/j.sna.2022.113377.

234. A. Yaacobi, J. Sun, M. Moresco, G. Leake, D. Coolbaugh, and M. R. Watts, "Integrated Phased Array for Wide-angle Beam Steering," *Optics Letters* 39, no. 15 (2014): 4575, https://doi.org/10.1364/ol.39.004575.

235. Y. Horie, A. Arbabi, E. Arbabi, S. M. Kamali, and A. Faraon, "High-Speed, Phase-Dominant Spatial Light Modulation with Silicon-Based Active Resonant Antennas," *ACS Photonics* 5, no. 5 (2018): 1711–1717, https://doi.org/10.1021/acsphotonics.7b01073.

236. M. Chalupnik, A. Singh, J. Leatham, M. Lončar, and M. Soltani, "Scalable and Ultralow Power Silicon Photonic Two-dimensional Phased Array," *APL Photonics* 8, no. 5 (May 2023): 051305, https://doi.org/10.1063/5.0139538.

237. H. Cao, P. Dong, Y. Hu, et al., "Ultrahigh-Efficiency All-Optically Tunable Silicon Photonic Filter with an Ultrawide Tuning Range," *ACS Photonics* 12 (2025): 5490–5500, https://doi.org/10.1021/acsphotonics.5c01160.

238. Y. Hu, Y. Sun, Y. Lu, et al., "Silicon Photonic MEMS Switches Based on Split Waveguide Crossings," *Nature Communications* 16, no. 1 (2025): 331, https://doi.org/10.1038/s41467-024-55528-9.

239. X. Liu, Q. Qiao, B. Dong, et al., "MEMS Enabled Suspended Silicon Waveguide Platform for Long-wave Infrared Modulation Applications," *International Journal of Optomechatronics* 16, no. 1 (2022): 42–57, https://doi.org/10.1080/15599612.2022.2137608.

240. S. Han, T. J. Seok, N. Quack, B.-W. Yoo, and M. C. Wu, "Large-scale Silicon Photonic Switches with Movable Directional Couplers," *Optica* 2, no. 4 (2015): 370, https://doi.org/10.1364/optica.2.000370.

241. Z. Li, Y. Han, L. Wu, et al., "Towards an Ultrafast 3D Imaging Scanning LiDAR System: A Review," *Photonics Research* 12, no. 8 (2024): 1709, https://doi.org/10.1364/prj.509710.

242. Q. Lin, S. Fang, Y. Yu, et al., "Optical Multi-beam Steering and Communication Using Integrated Acousto-optics Arrays," *Nature Communications* 16 (2025): 4501, https://doi.org/10.1038/s41467-025-59831-x.

243. B. Li, Q. Lin, and M. Li, "Frequency–angular Resolving LiDAR Using Chip-scale Acousto-optic Beam Steering," *Nature* 620, no. 7973 (2023): 316–322, https://doi.org/10.1038/s41586-023-06201-6.

244. K. H. Koh, C. Lee, and T. Kobayashi, "A Piezoelectric-driven Three-dimensional MEMS VOA Using Attenuation Mechanism with Combination of Rotational and Translational Effects," *Journal of Microelectromechanical Systems* 19, no. 6 (2010): 1370–1379, https://doi.org/10.1109/JMEMS.2010.2076785.

245. A. Dutta, Z. Niu, A. M. Abdullah, et al., "Closely Packed Stretchable Ultrasound Array Fabricated with Surface Charge Engineering for Contactless Gesture and Materials Detection," *Advanced Science* 11, no. 15 (2024): 2303403, https://doi.org/10.1002/advs.202303403.

246. Y. Zhang, Z. Xiong, L. He, et al., "Electrically Reconfigurable Surface Acoustic Wave Phase Shifters Based on ZnO TFTs on LiNbO3 Substrate," *International Journal of Extreme Manufacturing* 7, no. 3 (2025): 035504, https://doi.org/10.1088/2631-7990/ada7a9.

247. E. Khaidarov, Z. Liu, R. Paniagua-Domínguez, et al., "Control of LED Emission with Functional Dielectric Metasurfaces," *Laser & Photonics Reviews* 14, no. 1 (2020): 1900235, https://doi.org/10.1002/lpor.201900235.

248. A. L. Holsteen, A. F. Cihan, and M. L. Brongersma, "Temporal Color Mixing and Dynamic Beam Shaping with Silicon Metasurfaces," *Science (80-)* 365, no. 6450 (2019): 257–260, https://doi.org/10.1126/science.aax5961.

249. R. Jia, T. C. Tan, S. S. Mishra, W. Wang, Y. J. Tan, and R. Singh, "On-Chip Active Non-Reciprocal Topological Photonics," *Advanced Materials* 37, no. 26 (2025): 2501711, https://doi.org/10.1002/adma.202501711.

250. P. Tipsawat, S. J. Ilham, J. I. Yang, Z. Kashani, M. Kiani, and S. Trolier-Mckinstry, "32 Element Piezoelectric Micromachined Ultrasound Transducer (PMUT) Phased Array for Neuromodulation," *IEEE Open Journal of Ultrasonics, Ferroelectrics, and Frequency Control* 2 (2022): 184–193, https://doi.org/10.1109/OJUFFC.2022.3196823.

251. M. Fukuta, R. Nakashima, T. Kan, and H. Takahashi, "Acoustically Driven Scanning Mirror Enhanced by Helmholtz Resonator Unit," in *Proceedings of the IEEE International Conference on Micro Electro Mechanical Systems (MEMS)* (IEEE, 2025), 995–998, https://doi.org/10.1109/MEMS61431.2025.10917420.

252. T. M. Khan, A. S. Tasdelen, M. Yilmaz, A. Atalar, and H. Köymen, "High-Intensity Airborne CMUT Transmitter Array with Beam Steering," *Journal of Microelectromechanical Systems* 29, no. 6 (2020): 1537–1546, https://doi.org/10.1109/JMEMS.2020.3026094.

253. Z. Wang, X. Li, J. Ji, et al., "Fast-speed and Low-power-consumption Optical Phased Array Based on Lithium Niobate Waveguides," *Nanophotonics* 13, no. 13 (2024): 2429–2436, https://doi.org/10.1515/nanoph-2024-0066.

254. J. Liu, B. Wang, Y. Gong, et al., "Focal Plane Array Based on Thin-Film Lithium Niobate for Fast-Speed and Low-Power-Consumption Beam Steering," *ACS Photonics* 12 (2025): 4171–4181, https://doi.org/10.1021/acsphotonics.5c00188.

255. B. Chen, Y. Li, Q. Xie, et al., "SiN-on-SOI Optical Phased Array LiDAR for Ultra-Wide Field of View and 4D Sensing," *Laser & Photonics Reviews* 18, no. 10 (2024): 2301360, https://doi.org/10.1002/lpor.202301360.

256. J. Chen, W. Li, Z. Kang, et al., "Single Soliton Microcomb Combined with Optical Phased Array for Parallel FMCW LiDAR," *Nature Communications* 16, no. 1 (2025): 1056, https://doi.org/10.1038/s41467-025-56483-9.

257. W. Li, X. Zhao, J. He, et al., "High-speed 2D Beam Steering Based on a Thin-film Lithium Niobate Optical Phased Array with a Large Field of View," *Photonics Research* 11, no. 11 (2023): 1912, https://doi.org/10.1364/prj.502439.

258. P. Martinez-Carrasco, T. H. Ho, D. Wessel, and J. Capmany, "Ultra-broadband High-resolution Silicon RF-photonic Beamformer," *Nature Communications* 15, no. 1 (2024): 1433, https://doi.org/10.1038/s41467-024-45743-9.

259. S. Satir and F. L. Degertekin, "Phase and Amplitude Modulation Methods for Nonlinear Ultrasound Imaging with CMUTs," *IEEE Transactions on Ultrasonics, Ferroelectrics, and Frequency Control* 63, no. 8 (2016): 1086–1092, https://doi.org/10.1109/TUFFC.2016.2557621.

260. E. A. Kittlaus, W. M. Jones, P. T. Rakich, N. T. Otterstrom, R. E. Muller, and M. Rais-Zadeh, "Electrically Driven Acousto-optics and Broadband Non-reciprocity in Silicon Photonics," *Nature Photonics* 15, no. 1 (2021): 43–52, https://doi.org/10.1038/s41566-020-00711-9.

261. L. Shao, D. Zhu, M. Colangelo, et al., "Electrical Control of Surface Acoustic Waves," *Nature Electronics* 5, no. 6 (2022): 348–355, https://doi.org/10.1038/s41928-022-00773-3.

262. D. D. Bühler, M. Weiß, A. Crespo-Poveda, et al., "On-chip Generation and Dynamic Piezo-optomechanical Rotation of Single Photons," *Nature Communications* 13, no. 1 (2022): 6998, https://doi.org/10.1038/s41467-022-34372-9.

263. J. Park, B. G. Jeong, S. I. Kim, et al., "All-solid-state Spatial Light Modulator with Independent Phase and Amplitude Control for Three-dimensional LiDAR Applications," *Nature Nanotechnology* 16, no. 1 (2021): 69–76, https://doi.org/10.1038/s41565-020-00787-y.

264. B. Dong, S. Aggarwal, W. Zhou, et al., "Higher-dimensional Processing Using a Photonic Tensor Core with Continuous-time Data," *Nature Photonics* 17, no. 12 (2023): 1080–1088, https://doi.org/10.1038/s41566-023-01313-x.

265. L. Shao, W. Mao, S. Maity, et al., "Non-reciprocal Transmission of Microwave Acoustic Waves in Nonlinear Parity–time Symmetric Resonators," *Nature Electronics* 3, no. 5 (2020): 267–272, https://doi.org/10.1038/s41928-020-0414-z.

266. D. U. Kim, Y. J. Park, D. Y. Kim, et al., "Programmable Photonic Arrays Based on Microelectromechanical Elements with Femtowatt-level Standby Power Consumption," *Nature Photonics* 17, no. 12 (2023): 1089–1096, https://doi.org/10.1038/s41566-023-01327-5.

267. I. T. Chen, B. Li, S. Lee, S. Chakravarthi, K. M. Fu, and M. Li, "Optomechanical Ring Resonator for Efficient Microwave-optical Frequency Conversion," *Nature Communications* 14, no. 1 (2023): 7594, https://doi.org/10.1038/s41467-023-43393-x.

268. L. Wang, P. Zhang, Z. Liu, Z. Wang, and R. Yang, "On-chip Mechanical Computing: Status, Challenges, and Opportunities," *Chip* 2, no. 1 (2023): 100038, https://doi.org/10.1016/j.chip.2023.100038.

269. A. Marković, A. Laborde, N. Mauran, H. Fanet, G. Pillonnet, and B. Legrand, "High-Temperature Dual-Rail Contactless MEMS Logic for Industrial Edge Computing," in *Proc. IEEE Int. Conf. Micro Electro Mech. Syst* (2025), 542–545, https://doi.org/10.1109/MEMS61431.2025.10917966.

270. H. Takemura, T. Mizumoto, A. Banerjee, J. Hirotani, and T. Tsuchiya, "Physical Reservoir Computing Using Nonlinear MEMS Resonator Having High Memory Capacity at 'Edge of Chaos," in *Proceedings of the IEEE International Conference on Micro Electro Mechanical Systems (MEMS)* (IEEE, 2023), 515–518, https://doi.org/10.1109/MEMS49605.2023.10052286.

271. C. Meffan, T. Ijima, A. Banerjee, J. Hirotani, and T. Tsuchiya, "Exploring Surface Acoustic Wave Devices for Sound-Based Reservoir Computing," in *Proceedings of the IEEE International Conference on Micro Electro Mechanical Systems (MEMS)* (IEEE, 2024), 529–532, https://doi.org/10.1109/MEMS58180.2024.10439559.

272. K. Shima, H. Takemura, M. Shimofuri, A. Banerjee, J. Hirotani, and T. Tsuchiya, "Improved Learning Performance in Physical Reservoir Computing Using Coupled Triple MEMS Nonlinear Resonators," in *Proceedings of the IEEE International Conference on Micro Electro Mechanical Systems (MEMS)* (2025), 546–549, https://doi.org/10.1109/MEMS61431.2025.10918117.

273. X. Guo, W. Yang, X. Xiong, Z. Wang, and X. Zou, "MEMS Reservoir Computing System with Stiffness Modulation for Multi-scene Data Processing at the Edge," *Microsystems & Nanoengineering* 10, no. 1 (2024): 84, https://doi.org/10.1038/s41378-024-00701-9.

274. S. Sankar, W.-Y. Cheng, J. Zhang, et al., "A Natural Biomimetic Prosthetic Hand with Neuromorphic Tactile Sensing for Precise and Compliant Grasping," *Science Advances* 11 (2025), https://doi.org/10.1126/sciadv.adr9300.

275. B. Dong, Z. Zhang, Q. Shi, et al., "Biometrics-protected Optical Communication Enabled by Deep Learning–enhanced Triboelectric/Photonic Synergistic Interface," *Science Advances* 8, no. 3 (2022), https://doi.org/10.1126/sciadv.abl9874.

276. J. Guo, F. Guo, H. Zhao, et al., "In-Sensor Computing with Visual-Tactile Perception Enabled by Mechano-Optical Artificial Synapse," *Advanced Materials* 37, no. 14 (2025): 2419405, https://doi.org/10.1002/adma.202419405.

277. H. Pei, H. Hu, Y. Dong, et al., "Electric Eels Inspired Iontronic Artificial Skin with Multimodal Perception and in-Sensor Reservoir Computing," *Advanced Functional Materials* 35 (2025), https://doi.org/10.1002/adfm.202506431.

278. P. Zhang, Y. Jia, and Z. Liu, "Nanoelectromechanical Memories Based on Nonlinear 2D MoS2Resonators," in *Proceedings of the IEEE International Conference on Micro Electro Mechanical Systems (MEMS)* (2022), 208–211, https://doi.org/10.1109/MEMS51670.2022.9699463.

279. Q. Shi, Z. Sun, X. Le, J. Xie, and C. Lee, "Soft Robotic Perception System with Ultrasonic Auto-Positioning and Multimodal Sensory Intelligence," *ACS Nano* 17, no. 5 (2023): 4985–4998, https://doi.org/10.1021/acsnano.2c12592.

280. K. Kim, J.-H. Hong, K. Bae, et al., "Extremely Durable Electrical Impedance Tomography–based Soft and Ultrathin Wearable E-skin for Three-dimensional Tactile Interfaces," *Science Advances* 10, no. 38 (2024): adr1099, https://doi.org/10.1126/sciadv.adr1099.

281. Y. Luo, C. Liu, Y. J. Lee, et al., "Adaptive Tactile Interaction Transfer via Digitally Embroidered Smart Gloves," *Nature Communications* 15, no. 1 (2024): 868, https://doi.org/10.1038/s41467-024-45059-8.

282. S. Chen, C. Liu, Y. J. Lee, et al., "Multimodal 5-DOF Stretchable Electromagnetic Actuators toward Haptic Information Delivery," *Advanced Functional Materials* 34, no. 17 (2024), https://doi.org/10.1002/adfm.202314515.

283. A. Vitale, E. Donati, R. Germann, and M. Magno, "Neuromorphic Edge Computing for Biomedical Applications: Gesture Classification Using EMG Signals," *IEEE Sensors Journal* 22, no. 20 (2022): 19490–19499, https://doi.org/10.1109/JSEN.2022.3194678.

284. A. Elhadad, N. Cascioli, Y. Gao, and S. Choi, 2025 23rd International Conference on Solid-State Sensors, Actuators and Microsystems (Transducers), Orlando, FL, USA, 2025, pp. 1037–1040, https://ieeexplore.ieee.org/abstract/document/11109917.

285. D. Liu, X. Tian, J. Bai, et al., "A Wearable in-sensor Computing Platform Based on Stretchable Organic Electrochemical Transistors," *Nature Electronics* 7, no. 12 (2024): 1176–1185, https://doi.org/10.1038/s41928-024-01250-9.

286. H.-C. Hsiao, Z.-X. Guan, and Y. Chiu, "AlN Thin-Film Piezoelectric-on-Silicon Transducers for in-Sensor Computing," in *2025 23rd International Conference on Solid-State Sensors, Actuators and Microsystems (Transducers)* (IEEE, 2025), 2110–2113, https://doi.org/10.1109/Transducers61432.2025.11109622.

287. Y. Chen, J. Cao, J. Qiu, et al., "Capacitive in-sensor Tactile Computing," *Nature Communications* 16, no. 1 (2025): 5691, https://doi.org/10.1038/s41467-025-60703-7.

288. M. H Hasan, A. Abbasalipour, H. Nikfarjam, et al., "Exploiting Pull-in/Pull-out Hysteresis in Electrostatic Mems Sensor Networks to Realize a Novel Sensing Continuous-time Recurrent Neural Network," *Micromachines* 12, no. 3 (2021): 1–17, https://doi.org/10.3390/mi12030268.

289. N. Fang, S. Wang, and C. Wang, "Distributed Optical fiber Vibration Sensing Implemented with Delayed Feedback Reservoir Computing," *Optics & Laser Technology* 162 (2023): 109244, https://doi.org/10.1016/j.optlastec.2023.109244.

290. X. Liu, Z. Zhang, J. Zhou, W. Liu, G. Zhou, and C. Lee, "Development of Photonic in-Sensor Computing Based on a Mid-Infrared Silicon Waveguide Platform," *ACS Nano* 18, no. 34 (2024): 22938–22948, https://doi.org/10.1021/acsnano.4c04052.

291. Z. Xiao, Z. Ren, Y. Zhuge, et al., "Multimodal in-Sensor Computing System Using Integrated Silicon Photonic Convolutional Processor," *Advanced Science* 11, no. 47 (2024): 2408597, https://doi.org/10.1002/advs.202408597.

292. Y. Guan, H. Li, Y. Zhang, et al., "Photon-efficient Camera with in-sensor Computing," *Nature Communications* 16, no. 1 (2025): 3201, https://doi.org/10.1038/s41467-025-58501-2.

293. H. Lin, J. Ou, Z. Fan, et al., "In Situ Training of an in-sensor Artificial Neural Network Based on Ferroelectric Photosensors," *Nature Communications* 16, no. 1 (2025): 421, https://doi.org/10.1038/s41467-024-55508-z.

294. Q. Shi, T. He, and C. Lee, "More than Energy Harvesting – Combining Triboelectric Nanogenerator and Flexible Electronics Technology for Enabling Novel Micro-/Nano-systems," *Nano Energy* 57 (2019): 851–871, https://doi.org/10.1016/j.nanoen.2019.01.002.

295. A. Luo, S. Gu, X. Guo, et al., "AI-enhanced Backpack with Double Frequency-up Conversion Vibration Energy Converter for Motion Recognition and Extended Battery Life," *Nano Energy* 131 (2024): 110302, https://doi.org/10.1016/j.nanoen.2024.110302.

296. H. Liu, S. Zhang, R. Kathiresan, T. Kobayashi, and C. Lee, "Development of Piezoelectric Microcantilever Flow Sensor with Wind-driven Energy Harvesting Capability," *Applied Physics Letters* 100, no. 22 (2012), https://doi.org/10.1063/1.4723846.

297. G. Tang, Z. Wang, X. Hu, et al., "A Non-Resonant Piezoelectric–Electromagnetic–Triboelectric Hybrid Energy Harvester for Low-Frequency Human Motions," *Nanomaterials* 12, no. 7 (2022): 1168, https://doi.org/10.3390/nano12071168.

298. H. Liu, C. Hou, J. Lin, et al., "A Non-resonant Rotational Electromagnetic Energy Harvester for Low-frequency and Irregular human Motion," *Applied Physics Letters* 113, no. 20 (2018), https://doi.org/10.1063/1.5053945.

299. L. Liu, Q. Shi, and C. Lee, "A Novel Hybridized Blue Energy Harvester Aiming at all-weather IoT Applications," *Nano Energy* 76 (2020): 105052, https://doi.org/10.1016/j.nanoen.2020.105052.

300. Y. Fang, T. Tang, Y. Li, et al., "A High-performance Triboelectric-electromagnetic Hybrid Wind Energy Harvester Based on Rotational Tapered Rollers Aiming at Outdoor IoT Applications," *iScience* 24, no. 4 (2021): 102300, https://doi.org/10.1016/j.isci.2021.102300.

301. Z. Q. Lu, L. Zhao, H. L. Fu, E. Yeatman, H. Ding, and L. Q. Chen, "Ocean Wave Energy Harvesting with High Energy Density and Self-powered Monitoring System," *Nature Communications* 15, no. 1 (2024): 6513, https://doi.org/10.1038/s41467-024-50926-5.

302. H. Liu, J. Zhang, Q. Shi, et al., "Development of a Thermoelectric and Electromagnetic Hybrid Energy Harvester from Water Flow in an Irrigation System," *Micromachines* 9, no. 8 (2018): 395, https://doi.org/10.3390/mi9080395.

303. Q. Shi, T. Wang, T. Kobayashi, and C. Lee, "Investigation of Geometric Design in Piezoelectric Microelectromechanical Systems Diaphragms for Ultrasonic Energy Harvesting," *Applied Physics Letters* 108, no. 19 (2016), https://doi.org/10.1063/1.4948973.

304. M. Huang, M. Zhu, X. Feng, et al., "Intelligent Cubic-Designed Piezoelectric Node (iCUPE) with Simultaneous Sensing and Energy Harvesting Ability toward Self-Sustained Artificial Intelligence of Things (AIoT)," *ACS Nano* 17, no. 7 (2023): 6435–6451, https://doi.org/10.1021/acsnano.2c11366.

305. Q. Shi, H. Wu, H. Wang, H. Wu, and C. Lee, "Self-Powered Gyroscope Ball Using a Triboelectric Mechanism," *Advanced Energy Materials* 7, no. 22 (2017), https://doi.org/10.1002/aenm.201701300.

306. Q. Wang, H. Guan, C. Wang, et al., "A Wireless, Self-powered Smart Insole for Gait Monitoring and Recognition via Nonlinear Synergistic Pressure Sensing," *Science Advances* 11, no. 16 (2025), https://doi.org/10.1126/sciadv.adu1598.

307. Y. Gao, B. Xu, M. Qiu, et al., "Fabric-Reinforced Functional Insoles with Superior Durability and Antifracture Properties for Energy Harvesting and AI-Empowered Motion Monitoring," *Advanced Functional Materials* 35, no. 10 (2025), https://doi.org/10.1002/adfm.202416577.

308. L. Lan, J. Xiong, D. Gao, et al., "Breathable Nanogenerators for an on-Plant Self-Powered Sustainable Agriculture System," *ACS Nano* 15, no. 3 (2021): 5307–5315, https://doi.org/10.1021/acsnano.0c10817.

309. T. He, J. Wang, D. Hu, Y. Yang, E. Chae, and C. Lee, "Epidermal Electronic-tattoo for Plant Immune Response Monitoring," *Nature Communications* 16, no. 1 (2025): 3244, https://doi.org/10.1038/s41467-025-58584-x.

310. C. Yu and G. Li, "Electrical Energy Harvesting by Connected Form Stable Phase Change Material Composites," *Energy Conversion and Management* 299 (2024): 117851, https://doi.org/10.1016/j.enconman.2023.117851.

311. Z. Gao, C. Fang, Y. Gao, et al., "Hybrid Electromagnetic and Moisture Energy Harvesting Enabled by Ionic Diode Films," *Nature Communications* 16, no. 1 (2025): 312, https://doi.org/10.1038/s41467-024-55030-2.

312. X. Lu, Y. Yuan, F. Chen, et al., "Harnessing Exceptional Points for Ultrahigh Sensitive Acoustic Wave Sensing," *Microsystems & Nanoengineering* 11, no. 1 (2025): 44, https://doi.org/10.1038/s41378-024-00864-5.

313. T. Dutta, A. Safinezhad, M. Zhuldybina, et al., "Advances in Integrated Quantum Photonics for Quantum Sensing and Communication," *Journal of Materials Chemistry C* 13, no. 23 (2025): 11521–11561, https://doi.org/10.1039/d4tc05290k.

314. J. Xu, X. Guo, and C. Lee, "Triboelectric Mat Multimodal System for Sleep Pose Estimation," *Proceedings IEEE International Conference on Micro Electro Mechanical Systems* (2025): 8–11, https://doi.org/10.1109/MEMS61431.2025.10917976.

315. T. Wang, T. Jin, W. Lin, et al., "Multimodal Sensors Enabled Autonomous Soft Robotic System with Self-Adaptive Manipulation," *ACS Nano* 18, no. 14 (2024): 9980–9996, https://doi.org/10.1021/acsnano.3c11281.

316. S. Choi, K. Yoon, S. Lee, et al., "Conductive Hierarchical Hairy Fibers for Highly Sensitive, Stretchable, and Water-Resistant Multimodal Gesture-Distinguishable Sensor, VR Applications," *Advanced Functional Materials* 29, no. 50 (2019): 1905808, https://doi.org/10.1002/adfm.201905808.

317. Z. Sun, Z. Zhang, and C. Lee, "A Skin-like Multimodal Haptic Interface," *Nature Electronics* 6, no. 12 (2023): 941–942, https://doi.org/10.1038/s41928-023-01093-w.

318. S. Zheng, A. Liu, J. Liu, et al., "A Diode-like Integrated Hydrogel for Piezoionic Generators and Sensors," *Nano Energy* 133 (2025): 110467, https://doi.org/10.1016/j.nanoen.2024.110467.

319. M. Zhu, S. He, T. Chen, and C. Lee, "Wearable Intelligent Human–Machine Interfaces Ready for Sustainable Edge Computing Systems," *AI Sensors* 1, no. 9 (2025), https://doi.org/10.3390/aisens1020009.

320. J. Chen, M. Xia, P. Chen, et al., "Innovations in Multidimensional Force Sensors for Accurate Tactile Perception and Embodied Intelligence," *AI Sensors* 1, no. 7 (2025), https://doi.org/10.3390/aisens1020007.

321. H. Wang, J. Hu, Y. Baek, et al., "Optical next Generation Reservoir Computing," *Light: Science & Applications* (2025): 245, http://arxiv.org/abs/2404.07857.

322. F. Hossein-Babaei and V. Ghafarinia, "Compensation for the Drift-like Terms Caused by Environmental Fluctuations in the Responses of Chemoresistive Gas Sensors," *Sensors and Actuators B: Chemical* 143, no. 2 (2010): 641–648, https://doi.org/10.1016/j.snb.2009.10.006.

323. M. Z. Abidin, A. Asmat, and M. N. Hamidon, "Comparative Study of Drift Compensation Methods for Environmental Gas Sensors," *IOP Conference Series: Earth and Environmental Science* 117, no. 1 (2018): 012031, https://doi.org/10.1088/1755-1315/117/1/012031.

324. D.-P. Yang, X.-G. Tang, and Q.-J. Sun, "Emerging Ferroelectric Materials ScAlN: Applications and Prospects in Memristors," *Materials Horizons* 11, no. 12 (2024): 2802–2819, https://doi.org/10.1039/D3MH01942J.

325. H. Liu, H. Wu, and K. P. Ong, "Giant Piezoelectricity in Oxide Thin Films with Nanopillar Structure," *Science* 369, no. 6501 (2020): 292–297, https://doi.org/10.1126/science.abb3209.

326. H. Zhu, Y. Wang, and J. Xiao, "Observation of Piezoelectricity in Free-standing Monolayer MoS2," *Nature Nanotechnology* 10, no. 2 (2015): 151–155, https://doi.org/10.1038/nnano.2014.309.

327. L. Persano, A. Camposeo, and F. Matino, "Advanced Materials for Energy Harvesting and Soft Robotics: Emerging Frontiers to Enhance Piezoelectric Performance and Functionality," *Advanced Materials* 36, no. 45 (2024), https://doi.org/10.1002/adma.202405363.

328. S. Raoux, "Phase Change Materials," *Annual Review of Materials Research* 39, no. 1 (2009): 25–48, https://doi.org/10.1146/annurev-matsci-082908-145405.

329. M. Wuttig and N. Yamada, "Phase-change Materials for Rewriteable Data Storage," *Nature Materials* 6, no. 11 (2007): 824–832, https://doi.org/10.1038/nmat2009.

330. B. Yang, X. Zhang, J. Ji, M. Jiang, and Y. Zhao, "A Comprehensive Review of Phase Change Material-based Wearable Devices for Personal Thermal Management: Mechanism, Location and Application Functionality," *Applied Thermal Engineering* 257 (2024): 124416, https://doi.org/10.1016/j.applthermaleng.2024.124416.

331. P. Liu, X. Chen, and Y. Li, "Aerogels Meet Phase Change Materials: Fundamentals, Advances, and beyond," *ACS Nano* 16, no. 10 (2022): 15586–15626, https://doi.org/10.1021/acsnano.2c05067.

332. H. Zhou, D. Li, and C. Lee, "Technology Landscape Review of In-Sensor Photonic Intelligence: From Optical Sensors to Smart Devices," *AI Sensors* 1, no. 5 (2025), https://doi.org/10.3390/aisens1010005.